



University of Bergen

**Master Degree Thesis**

IN MEDICAL PHYSICS AND TECHNOLOGY

---

**Noise and Cluster Size Studies of ALPIDE-CMOS  
Pixel Sensor for pCT**

---

**Susmita Afroz**

Supervisor

**Professor Dieter Rohrich**

Co-supervisor

**Ganesh Jagannath Tambave, PhD**

**Department of Physics and Technology**

University of Bergen

Bergen, Norway

**June 2018**

---

**Dedication**

*To my beloved husband and our dearly loved son, Prappo.*

<b>Contents</b>	
<b>Acknowledgements</b>	<b>i</b>
<b>List of Abbreviations</b>	<b>ii</b>
<b>List of Figures</b>	<b>iv</b>
<b>List of Tables</b>	<b>ix</b>
<b>Abstract</b>	<b>x</b>
<b>Chapter-1 Introduction</b>	<b>1</b>
<b>Chapter-2 Proton CT (pCT)</b>	<b>3</b>
2.1 Medical Imaging	3
2.1.1 Advances in Medical Imaging	3
2.1.2 Introduction to Computed Tomography (CT)	4
2.1.3 X-ray Depth Dose Distribution	5
2.2 Heavy Charged Particle	6
2.2.1 Proton Interaction with Matter	6
2.2.2 Proton Stopping Power and Linear Energy Transfer (LET)	7
2.2.3 Multiple Coulomb Scattering (MCS)	8
2.2.4 Nuclear Interaction	8
2.2.5 Proton and its Depth Dose Distribution	8
2.2.6 Potential Advantage of Proton in Radiation Therapy	9
2.3 Brief History towards Proton Computed Tomography (Using Energy Loss)	10
2.4 Imaging Using Different Properties of the Proton	11
2.4.1 Marginal Range Radiography	11
2.4.2 Nuclear Scattering Radiography	12
2.4.3 Proton Scattering Radiography	12
2.5 pCT for Imaging the Relative Stopping Power (RSP)	14
2.5.1 Phase-1 pCT Scanner (Conceptual pCT Detector Approach)	14
2.5.2 Design Specification	15
2.5.3 Proton Tracking System and Energy/Range Measurement	16
2.6 Expected Performance of PCT	18
2.6.1 Path Estimation and Spatial Resolution	18
2.6.2 Dose and Density Resolution	19
2.7 Next-Generation pCT	20
2.7.1 Digital Tracking Calorimeter (DTC)	20
<b>Chapter-3 Monolithic Active Pixel Sensor (MAPS)</b>	<b>21</b>
3.1 Interaction of Particles with Silicon Sensor	22
3.1.1 Energy Loss of Charged Particle	22
3.1.2 Energy Loss of Electromagnetic Radiation	23
3.1.3 Detection Principle of MAPS	24
3.2 ALPIDE	25
3.2.1 ALPIDE in Pixel Architecture	25
3.2.2 ALPIDE Pixel Matrix Architecture	26
3.2.3 ALPIDE Readout Architecture	27

3.3 The ALPIDE Family	28
3.3.1 ALPIDE Prototypes	28
3.3.2 Pixel Chip Requirement	29
3.4 ALPIDE Principle of Operation	29
3.4.1 In-pixel Hit Discrimination	29
3.4.2 ALPIDE Front-End Circuit	30
3.4.3 Pixel Analog Front-End	31
3.4.4 Digital Front-End Section	32
3.4.5 Priority Encoders and Pixel Indexing	33
3.5 Radiation Damage in MAPS	35
3.5.1 Radiation Damage Effects	35
<b>Chapter-4 Methods Materials</b>	<b>37</b>
4.1 ALPIDE Test Board	37
4.2 Chip Tests	38
4.3 Threshold and Noise Measurement	40
4.4 Fake Hit Rate (FHR)	41
4.5 Sealed Radioactive Sources	42
4.6 Proton Beam	43
4.6.1 ALPIDE Proton Beam Test	43
4.6.2 Test Setup	44
4.7 Helium Beam Test	45
4.8 ALPIDE Data Collection	45
4.8.1 Cluster	46
4.8.2 Analysing Cluster Size and Cluster Distribution	47
<b>Chapter-5 Results and Discussion</b>	<b>48</b>
5.1 Test objectives	48
5.2 ALPIDE Chips	49
5.3 ALPIDE Tests	49
5.3.1 Test 1- DAC Scan	49
5.3.2 Test 2- Threshold and Noise Scan with varying $V_{BB}$	50
5.3.3 Test 3- Threshold and Noise Scan with varying ITHR and VCASN	54
5.3.4 Test 4- Noise Occupancy or Fake Hit Rate Test for Three Different $V_{BB}$	56
5.3.5 Test 5- Noise Occupancy or Fake Hit Rate test with varying ITHR and VCASN	60
5.3.6 Test 6- Radiation Effect	62
5.4 Cluster Analysis	72
5.4.1 Alpha Beta and Gamma Source	72
5.4.2 X-ray Source Test	77
5.4.3 Proton Beam Test	81
5.4.4 Energy Deposition/LET versus Cluster Size	83
<b>Chapter-6 Conclusions</b>	<b>86</b>
6.1 Discussion on Performed Test and Findings	86

6.2 Implications of This Research	87
6.3 Direction of Further Research	87
<b>Appendix</b>	<b>89</b>
A.1 Analog Front-End Optimization for Final ALPIDE	89
A.2 List of Helium Beam Test on Chip-2	91
A.3 C++ Code for ALPIDE Cluster Analysis	92
<b>Bibliography</b>	<b>98</b>

## ACKNOWLEDGEMENTS

First of all, I express gratitude and satisfaction to omnipotent Allah who enabled me to carry out this thesis work by keeping me healthy and enthusiastic throughout the period.

This master thesis was conducted at the Department of Physics and Technology, University of Bergen. I would like to thank the department for providing me this excellent opportunity.

I wish to express my heartiest gratitude, indebtedness, and appreciation to my supervisor, Professor Dieter Rohrich who provided constant and immeasurable support, valuable guidance and never-ending inspiration throughout my research period.

My Co-supervisor, Ganesh Jagannath Tambave, PhD at the Department of Physics and Technology, University of Bergen constantly offered wise advice, professional guidance and inspiration. My profound reverence to him.

My heartfelt thanks go to Prof Dr. Renata Gruner for her kind support, guidance, teaching and excellent academic counsel during my course-work and training on application of medical physics.

My special thanks to Maruf Ahmad, Research Fellow, Department of Biomedical Physics and Technology, University of Dhaka, for his support in writing codes and analysing data. I also like to extend my gratitude to Andreas Tefre Samnøy for his assistance in various aspects and practical issues.

Warm thanks to my Medical Physics colleagues Simon Kristian Huiberts and Viljar Nilsen Eikeland for their nice friendship and facilitating a healthy and productive discussion during our thesis at IFT.

Finally, I would like to thank my family, especially my husband Monirul Hoque Pasha for boundless love, support and for creating a joyful atmosphere at home, which was crucial for my study. Special thanks go to my son for being healthy and lovely, and for being a source of all happiness.

---

Bergen, June 2018

## LIST OF ABBREVIATIONS

<b>AERD</b>	Address-Encoder Reset-Decoder
<b>ALICE</b>	A Large Ion Collider Experiment
<b>APS</b>	Active Pixel Sensor
<b>AQUA</b>	Advanced Quality Assurance.
<b>CCD</b>	Charge-Coupled Device
<b>CMOS APS</b>	Complementary Metal Oxide Semi-conductor Active Pixel Sensor
<b>CsI:TI</b>	Thallium-doped Caesium Iodide Scintillator.
<b>CSP</b>	Cubic Spline Path
<b>CSUSB</b>	California State University, San Bernadino.
<b>DACs</b>	Digital-to-Analog Converters
<b>DTC</b>	Digital Tracking Calorimeter
<b>FNAL</b>	Fermilab National Accelerator Laboratory.
<b>HU</b>	Hounsfield Unit
<b>INFN</b>	Istituto Nazionale di Fisica Nucleare.
<b>LANL</b>	Los Alamos National Laboratory
<b>LET</b>	Linear Energy Transfer
<b>LLU</b>	Loma Linda University.
<b>MAPS</b>	Monolithic Active Pixel Sensor
<b>MCS</b>	Multiple Coulomb Scattering
<b>MIP</b>	Minimum Ionizing Particle
<b>MLP</b>	Most-Likely Path
<b>MRI</b>	Magnetic Resonance imaging
<b>NaI:TI</b>	Thallium-doped Sodium Iodide Scintillator.
<b>NIU</b>	Northern Illinois University.
<b>NM</b>	Nuclear Medicine
<b>NM</b>	Nuclear Medicine
<b>NMOS</b>	N-Type Metal-Oxide-Semiconductor
<b>pCT</b>	Proton Computed Tomography
<b>PDD</b>	Percentage Depth Dose
<b>PET</b>	Positron Emission Tomography
<b>PMOS</b>	P-Type Metal-Oxide-Semiconductor
<b>PPS</b>	Passive Pixel Sensor
<b>PRaVDA</b>	Proton Radiotherapy Verification and Dosimetry Applications.
<b>PRIMA</b>	Proton Imaging.
<b>PSD</b>	Position-Sensitive Detector
<b>PTCOG</b>	Particle Therapy Cooperation Group
<b>RBE</b>	Relative Biological Effectiveness
<b>RERD</b>	Residual Energy-Range Detector
<b>RSP</b>	Relative Stopping Power
<b>Sci-Fi</b>	Scintillating Fibre Hodoscope.
<b>SLP</b>	Straight-Line Path
<b>SOBP</b>	Spread out Bragg Peak

---

<b>SPECT</b>	Single-Photon Emission CT
<b>SSDs</b>	Silicon Strip Detectors
<b>TID</b>	Total Ionising Dose
<b>UCSC</b>	University of California Santa Cruz.
<b>VLSI</b>	Very Large Scale Integration
<b>xCT</b>	X-ray Computed Tomography
<b>YAG: Ce</b>	Cerium-doped Yttrium Aluminium Garnet Scintillator.

## LIST OF FIGURES

Figure 1: CT reveals superb anatomical detail, as seen in (a) sagittal, (b) coronal [9].....	5
Figure 2: Dose deposition from a Megavoltage photon beam in a patient. $D_s$ is the surface dose at the beam entrance side, $D_{ex}$ is the surface dose at the beam exit side. $D_{max}$ is the dose maximum often normalized to 100, resulting in a depth dose curve referred to as the Percentage Depth Dose (PDD) distribution. The region between $Z = 0$ and $Z = Z_{max}$ is referred to as the dose buildup region [16]. .....	6
Figure 3: (a) The stopping power of proton in aluminium, plotted over proton energy [19] (b) LET Vs. depth in liquid water for proton with initial energies of 80, 100, 150 and 200 MeV [20].....	7
Figure 4: (a) Depth dose curves for photons and protons. Notice the exponential tail seen in the photon curve that results in dose deposition through the entire patient. The proton curve shows that there is no dose deposition after the Bragg peak [28]. (b) The Spread out Bragg Peak (SOBP). Combining beams with different energies it is possible to describe a longitudinal profile [29].....	9
Figure 5: (a) The first published proton radiograph from 1968 (b) A slice image of a 29 cm diameter phantom from the Los Alamos proton CT scanner in 1978 [38].....	10
Figure 6: Illustration of marginal range radiography concept (a) The flux-depth curves for proton and X-rays passing through a homogeneous medium and highlight the higher sensitivity of proton (b) Dose-depth curve for 148 MeV protons in water, showing the Bragg peak of ionization near the end of the particle range. The position of the region examined (tissue specimen) and of the screen-film detector relative to the Bragg peak are indicated [45].....	12
Figure 7: Principle of proton scattering radiography illustrating intensity distribution near an edge [43]. .....	13
Figure 8: Schematic of pCT. Protons with known entry energy $E_{in}$ are recorded one by one in the detector reference system (s, t, u) as they traverse the image object from many different projection angles $\phi$ . The recorded data include entry and exit positions and entry and exit angles as well as exit energy $E_{out}$ in the energy detector. There are four trackers two upstream, two downstream. Particles are tracked one by one [48].....	14

Figure 9: The path of protons traveling inside an object is determined by a multitude of individual scattering events leading to a zigzag path (red). Both the position and direction of entry and exit proton are registered. Given the object boundary, the intersecting points *A* and *B* of a proton with the object can be obtained. While the intersecting points are sufficient to estimate the straight line path (black) of the proton, additional knowledge of the entry and exit directions permits estimation of the most likely path (blue line) [55]..... 18

Figure 10: Illustration of different path estimations for image reconstruction. In black the proton trajectory, in red estimation made: (a) knowing only the position on downstream detector; (b) knowing the positions upstream and downstream from the object; (c) knowing the position and direction upstream and downstream from the object; (d) estimating the most likely path using the position and direction upstream and downstream from the object [35]. 19

Figure 11: Cross section scheme of a MAPS pixel combines Si sensor and CMOS read-out electronics in a single volume [71]. ..... 22

Figure 12: Landau distribution of the energy loss of highly relativistic particles ( $\beta\gamma \gg 100$ ) in a silicon layer of 320  $\mu\text{m}$  thickness [76]..... 23

Figure 13: Total photon cross section in silicon [71]. ..... 24

Figure 14: Schematic cross section of pixel of MAPS (TowerJazz 0.18  $\mu\text{m}$  imaging CMOS with the deep p-well feature) [73], [82], [83]. ..... 25

Figure 15: (a) Schematic of a full scale ALPIDE chip (1024 pixel column $\times$ 512 row): pixels are arranged in double columns (b) with a priority encoder per double column. This allow space to be used more efficiently for the priority encoder as it is routing dominated and several routing lines can be shared between the two columns [82]..... 27

Figure 16: Readout organization of the chip with details on the pixel cell [82]..... 27

Figure 17: In-pixel hit discrimination block diagram and signal flow [83]..... 30

Figure 18: Pixel analog front end schematic for ALPIDE (a) principle (b) presented circuit [80], [83]. ..... 30

Figure 19: Functional diagram of the pixel digital front-end [82], [84]. ..... 33

Figure 20: Indexing of pixels inside a double column provided by the Priority Encoders [84]. ..... 34

Figure 21: Carrier (black) and DAQ (green) board connected together. There's a glass protector on the top of the Chip. ....	37
Figure 22: S-curve measurement: hit ratio $r(Q_{inj})$ as a function of $Q_{inj}$ [76].....	40
Figure 23: Threshold and noise distributions.....	41
Figure 24: Sealed Radioactive sources for laboratory experiment. (a) $^{241}\text{Am}$ isotope as Alpha source (b) $^{90}\text{Sr}$ isotope as Beta source (c) $^{55}\text{Fe}$ isotope as Gamma source (d) Variable energy X-ray source.....	42
Figure 25: (a) Beam vent (b) Photographic plate placed on the beam vent to measure the diameter (c) measured diameter around 1 cm.....	44
Figure 26: (a) Aluminum base to place the holder on the beam trail (b) Aluminium holder and shielding for ALPIDE chip (c) Chip placement. ....	45
Figure 27: (a) Beam monitoring window (b) Measuring Gamma and Neutron incidence simultaneously. ....	45
Figure 28: Generated data file with 5 columns after source scan. ....	46
Figure 29: Cluster for alpha particle. Notice that the cluster occurs in two frames. ....	47
Figure 30: Plot for all individual DAC. ....	49
Figure 31: Threshold and Noise at 0V $V_{BB}$ . ....	51
Figure 32 : Threshold and Noise at -3V $V_{BB}$ . ....	51
Figure 33: Threshold and Noise at -6V $V_{BB}$ . ....	51
Figure 34: Threshold and Noise at 0V $V_{BB}$ . ....	52
Figure 35: Threshold and Noise at -3V $V_{BB}$ . ....	52
Figure 36: Threshold and Noise at -6V $V_{BB}$ . ....	52
Figure 37: Threshold and Noise at 0V $V_{BB}$ . ....	53
Figure 38: Threshold and Noise at -3V $V_{BB}$ . ....	53
Figure 39: Threshold and Noise at -6V $V_{BB}$ . ....	53
Figure 40: Mean threshold as a function of ITHR and VCASN.....	55
Figure 41: Mean noise as a function of ITHR and VCASN.....	55

Figure 42: Fake Hit Rate at $V_{BB}$ (a) 0V (b) -3V (c) -6V. ....	57
Figure 43: Fake Hit Rate at $V_{BB}$ (a) 0V (b) -3V (c) -6V.....	58
Figure 44: Fake Hit Rate at $V_{BB}$ (a) 0V (b) -3V (c) -6V.....	59
Figure 45: Fake hit rate of chip-1, as a function of number of masked pixels with nominal VCASN=50 DAC and $V_{BB}=0V$ (a) ITHR=10 DAC (b) ITHR=20 DAC (c) ITHR=30 DAC (d) ITHR=40 DAC (e) ITHR=50 DAC. ....	61
Figure 46: Fake hit rate as a function of ITHR and VCASN for $V_{BB}=0V$ and zero pixels masked and its projection along the axis of VCASN. ....	61
Figure 47: Radiation effect in chip-2 in terms of threshold and noise level. Affected pixels in (a) thresholdmap at $V_{BB}=-6V$ (b) noisemap at $V_{BB}=-6V$ (c) thresholdmap at $V_{BB}=-3V$ (d) noisemap at $V_{BB}=-3V$ (e) thresholdmap at $V_{BB}=0V$ (f) noisemap at $V_{BB}=0V$ .....	63
Figure 48: Pixels in the irradiated area (addresses are encircled).....	64
Figure 49: Beam pattern. The red arrows show the way the beam spot is moving. Each dot represents a beam spot, and the beam spot stays in one position for a certain time, the dwell time, before it skips to the next position [99]. ....	64
Figure 50: Activated pixel in a small irradiated area (a) $128 \times 128 \mu m^2$ (b) $128 \times 128 \mu m^2$ (c) L shape area of $2048 \mu m^2$ (d) ) L shape area of $2048 \mu m^2$ . ....	65
Figure 51: Projection of hits from X and Y axis for Area-2 showing maximum hits in inner most few pixels. ....	65
Figure 52: Thresholdmap (Left), Threshold value of irradiated pixels (Right).....	66
Figure 53: Noisemap (Left), Noise value of irradiated pixels (Right).....	66
Figure 54: Thresholdmap (Left), Threshold value for affected pixels (Right).....	67
Figure 55: Noisemap (Left), Noise value for affected pixels (Right).....	67
Figure 56: (a) Threshold and (b) Noise value for affected pixels.....	68
Figure 57: Mean (a) Threshold and (b) Noise over Dose. ....	70
Figure 58: Hitmap for (a) Gamma (b) Beta (c) Alpha. ....	73
Figure 59: (a) A single event cluster of Gamma (b) Cluster Size histogram for Gamma. ....	74

Figure 60: (a) Single event cluster for MIPS particle (b) Single event cluster for low energetic electron (c) A beta track (d) Cluster size histogram for Beta. ....	75
Figure 61: (a) A rare big single event cluster for Alpha (b) Cluster size histogram for Alpha. ....	76
Figure 62: (a) Range of alpha particles in silicon (b) Ionisation energy loss along a particle track due to nearly 5 MeV alpha particle [100]. ....	76
Figure 63: (a) Hitmaps showing number of entries for X-ray with energy 8.04 and 8.91 KeV from Cu (b) Energy vs. Number of pixel hit. ....	78
Figure 64: Cluster size histogram for X-ray with energy (a) 8.04 and 8.91 KeV from Cu (b) 13.37 and 14.97 KeV from Rb (c) 17.44 and 19.63 KeV from Mo (d) 22.10 and 24.99 KeV from Ag (e) 32.06 and 36.55 KeV from Ba (f) 44.23 and 50.65 KeV from Tb. ....	80
Figure 65: Energy vs. Mean cluster size. ....	81
Figure 66: Hitmaps for proton beam at $V_{BB}=-6V$ . ....	82
Figure 67: Clusters for proton at $V_{BB}=-6V$ . ....	82
Figure 68: Cluster Size histogram for proton at $V_{BB}=0V$ and 1.6 m distant. ....	83
Figure 69: Cluster Size vs. Deposited Energy/LET. ....	85
Figure 70: Optimized front end schematic with parasitic capacitance (cause gain reduction) of pALPIDE-3 [83]. ....	90

## LIST OF TABLES

Table 1: Design specifications for a pCT scanner for therapeutic applications [50].....	15
Table 2: A summary of current and recent Proton Radiography (PRG)/Proton CT (pCT) prototypes [38].....	17
Table 3: The prototypes of the ALPIDE family [80].....	28
Table 4: Pixel chip requirement for ALPIDE [83] .....	29
Table 5: Isotope parameters for variable X-ray source [98] .....	43
Table 6: List of ALPIDE Chips .....	49
Table 7: Nominal values for the DACs at 1.8V, expressed in DAC units.....	50
Table 8: Adjusted DAC value for different reverse bias voltage ( $V_{BB}$ ) .....	50
Table 9: Interaction probability with changing X-ray energy for Silicon .....	79
Table 10: ALPIDE sectors [84]. .....	89
Table 11: Details of chip-2 scan for Helium-4 ion beam.....	91

## ABSTRACT

The use of proton beam has been introduced in medical physics for therapeutic purposes in cancer treatment and it has been proven much more efficient than conventional X-ray. Treatment planning in proton therapy is usually provided with information from X-ray CT where X-ray attenuation in tissue is needed to be converted to proton stopping power. This conversion leads to several uncertainties because proton interacts with matter in a different way than the photon. An intuitive way to mitigate this problem is using charged particles as the basis for the CT-scan and this is the time when the idea of “Proton CT” came up. There are nearly 10 pCT prototypes worldwide and all are designed with two separate devices for proton tracking and calorimetry. Few recent studies discovered the potential of merging these two separate systems into one uniquely featured Digital Tracking Calorimeter (DTC). The DTC is made of multiple layers of Monolithic Active Pixel Sensor (MAPS) chips. In this study, ALPIDE chip has been brought in as MAPS for DTC. The ALPIDE was developed for the heavy-ion experiment at CERN to detect high energy charged particles. For pCT, ALPIDE is conceptually an ideal sensor because of its low power consumption and chip area with more than half a million pixels with in-pixel readout scheme. This thesis is carried out in three main parts:

- Characterization of ALPIDE chip focusing particularly on chip’s threshold and fake hit rate.
- Measuring radiation-induced effects on the sensor performance.
- Analysing sensor response for different types of radiation.

In addition, I contributed to Proton Beam Test at OCL, Oslo and analyzed the data afterward. This thesis also includes the analysis performed on proton beam data and significant findings from the analysis.

This study represents a key contribution to pCT in terms of defining the sensor behavior and interpreting sensor response.

**Key words:** pCT, DTC, MAPS, ALPIDE.

## CHAPTER-1 INTRODUCTION

Following the earliest proposition by Harvard physicist Robert Wilson in 1946 that the highly localized deposition of energy from protons offers distinct advantages in radiation therapy, it took more than 40 years until in 1990 the first generation hospital-based proton treatment center launched [1]. Since then especially in the recent decade, the number of cancer patients treated with proton radiation therapy has been increased significantly. The number of patients received particle therapy worldwide from 1954 to 2014 is more than 137,000. In the year 2014, 86% of 15,000 patients who received particle therapy were treated with protons [2]. The proton therapy has been proven more capable than conventional X-ray radiation therapy to deliver high doses to well-defined target volume close to critical normal structures and limits the amount of healthy tissue irradiated to a minimum. Proton therapy also minimizes short term and long term side effects induced by treatment.

For proton therapy, till today the widespread way of dose calculation is X-ray Computed Tomography (xCT). This use of xCT leads to a certain range of uncertainties that obviate the advantage of proton therapy, especially in treatment planning due to dissimilarity in physical interactions between photons and protons. The proton range is important for dose calculations in treatment planning. To obtain this range in a tissue, attenuation of X-rays in Hounsfield Unit (HU) maps needs to be converted to Relative Stopping Power (RSP) maps and this conversion creates range uncertainties. Now to eliminate this uncertainty, a proton-based treatment planning or Proton Computed Tomography (pCT) system is introduced. The pCT uses the same therapeutic proton beam and produces images avoiding any conversion uncertainties and thus results in a better dose accuracy as well as the clinically safe margin for target volume.

The pCT images an object (mainly patient) by using a high energy proton beam passing through it and then measuring the residual energy of proton by a detector placed after the patient [3]. The residual energy from each proton together with proton's estimated path through the patient is used as a basis for reconstructing a volume with RSP. From the currently available pCT prototypes [4], the remaining range and energy of each proton after traversing the object is often measured by calorimeter such as CsI:Tl, YAG:Ce, NaI:Tl and plastic scintillator telescopes. For proton tracking in order to measure how and where the protons lose their energy, the distal and proximal detectors such as Scintillating Fibers or Silicon Strip Detectors are commonly used.

As a part of the ongoing pCT project, in collaboration among the University of Bergen, Bergen University College, Haukeland University Hospital and Utrecht University, a study was conducted to investigate the feasibility of using a high-granularity Digital Tracking Calorimeter (DTC) for particle tracking and measuring individual proton's range and energy [3]. The DTC accommodates multiple layers of Monolithic Active Pixel Sensor (MAPS) chips with a digital readout and is going through several optimizations with next-generation MAPS to achieve a readout time of 5  $\mu$ s and best tracking performance.

The MAPS-ALPIDE has been chosen as the key element of the DTC for this study. The ALPIDE was developed for ALICE (A Large Ion Collider Experiment) at CERN. This study

mainly presents sensor response when exposed by different radiation,  $\gamma$  (from a  $^{55}\text{Fe}$ -source),  $\beta$  (from a  $^{90}\text{Sr}$ -source) and  $\alpha$  (from a  $^{241}\text{Am}$ - source). One of the remarkable response from the sensor chip is cluster size and it is influenced by some factors particularly- particle's energy and charge and mass.

This study also includes chip characterization in terms of the threshold, noise and fake hit rate, and defines their changing pattern over the changing values of associated parameters. Finally, this study contains a part regarding radiation damage that is observed and studied on a particular chip, and discusses the radiation effect consequences.

Chapter-2 of this thesis paper includes a wide discussion on pCT as a highly potential medical imaging modality along with operational details. The Monolithic Active Pixel Sensor-ALPIDE is discussed in Chapter-3 with the technical benefit over previous MAPS. Chapter-4 gives an idea about the standard practice of the methods and materials used for this study along with experimental setup. The results and discussion are presented in Chapter-5, at last, the paper ends with conclusions in Chapter-6.

## **CHAPTER-2 PROTON CT (PCT)**

This chapter covers a brief introduction to medical imaging and the growing need of advance imaging modalities considering high dependency on image for diagnosis. The development and medical implementation of pCT over last half a century with advanced technical benefit is also discussed. Advantage of pCT over conventional X-ray CT in terms of image quality and hazardous dose deposition has brought into contemplation.

### **2.1 Medical Imaging**

Medical imaging mainly comprehends wide varieties of imaging modalities and processes in order to image the human body for diagnostic and treatment purposes. To improve public health in all population group medical imaging is playing a vital role by introducing and inducting convenient and effective way of diagnosis as well as treatment [5].

Acquiring data from human body, that is undoubtedly an incredibly complex system, about its static and dynamic properties leads to enormous amount of information. The biggest challenge for researchers and clinicians was to obtain and display this immense information of the body in order to interpret, understand and employ them for useful diagnostic methods and therapeutic procedures. To address this challenge, the idea of imaging for the presentation of information was proven as most efficient approach. Now the reason of being efficient is the human disposition of relying more on sight rather any perceptual skill on anything in the world. Physician's dependency on medical images to understand the human body as well as intervene in the processes of human illness and injury is increasing.

#### **2.1.1 Advances in Medical Imaging**

The journey of Medical Imaging started from Wilhelm Conrad Roentgen's invention of X-ray in November 1895 [6]. Roentgen discovered the penetration ability of an invisible ray through human flesh better than bones and metal and first to see "radiographs" [7]. X-ray radiography spread out very rapidly due to mass production of X-ray tubes also, the worldwide commercialization makes this technology a great medical advance within a few years.

By 1950, radiopharmaceuticals paved the way of Nuclear Medicine (NM) and NM came into the armamentarium of diagnostic imaging test, based on the cellular function and physiology instead of relying on physical changes in tissue anatomy to perceive the extent of a disease process in the body [7].

Ultrasound imaging that came into clinical use in the 1970s [7] has a storied history of being used in finding German submarines in the protection of North Atlantic convoys during World War II [8]. Its initial involvement was to produce deep heat and ablation of brain lesions for Parkinson's disease in physical therapy. With a fine alteration of wave characteristics along with keeping energy transfer limited and ensuring almost no deep tissue heating at the same

time having no adverse bio-effects, ultrasound has become a very popular imaging technique [8].

In the 1970s, Magnetic Resonance Imaging (MRI) evolved based on a unique observation that is, the nuclear magnetic relaxation time of tissues and tumors is different [7]. For imaging, the magnetic field around 10,000 to 60,000 times stronger than the earth's magnetic field (25 to 65 microteslas) is used in MRI scanners [9]. Nuclear magnetic resonance properties of the proton, which is the main essence of MRI, explicate proton precession about its axis and preferential absorption of radio wave energy under a strong magnetic field. The subsequent remit of this energy after a period of time is picked up by the scanner and turned into a picture by the help of a computer [7], [9].

### **2.1.2 Introduction to Computed Tomography (CT)**

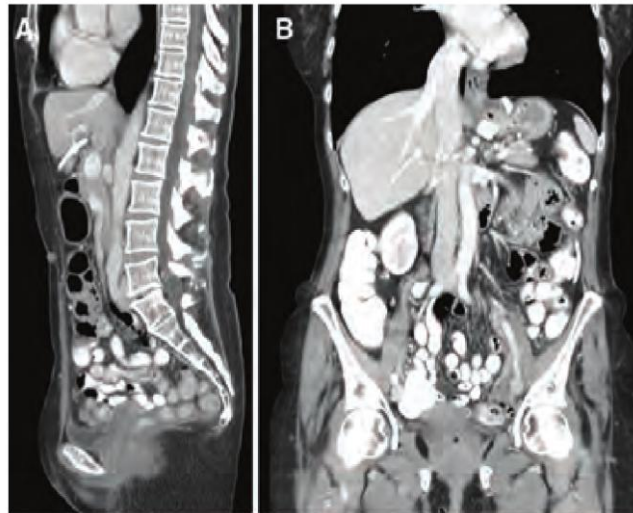
Sir Godfrey Hounsfield's invention of the CT machine in the 1970s showed the first instance of computer technology mixing into the medical field [10]. The pioneering work was reflected in the first commercial CT unit announced in 1972 [11]. The term *Tomography* is derived from ancient Greek *tomos* (slice) and *graphō* (picture) [12]. The CT is a transmission technique that is used to acquire images of individual slabs of tissue in the patient.

In conventional radiograph, a three-dimensional object is depicted as a two-dimensional image and the third dimension is represented as overlapping shadow in the 2D image so as a consequence anatomical structure of interest is frequently obscured by shadow likewise two tissues with similar densities cannot be distinguished by conventional radiograph [12].

The advantages of CT over conventional radiography is related to several of its feature, most importantly [11], [12]:

- Elimination of superimposed structure to obtain an unobstructed view of the detailed anatomy;
- Differentiating small differences in density of anatomic structures and abnormalities;
- And a superior quality image.

The practice of medicine has dramatically changed due to a substantial reduction of the need for exploratory surgery after the advent of CT. Acquisition capability of modern CT scanner is nearly 800 images in 5 seconds [9]. CT image reveals the presence of cancer, ruptured disks, subdural hematomas, aneurysms, and much other pathology. Due to isotropic volume data set, coronal and sagittal CT images, shown in figure-1, are incorporated with the traditional axial images.



(a)

(b)

**Figure 1: CT reveals superb anatomical detail, as seen in (a) sagittal, (b) coronal [9].**

Worldwide use of CT with combination of Positron Emission Tomography (PET) as PET-CT and Single-Photon Emission CT as SPECT is growing [13]. In a broader aspect, the remarkable increase in the volume of medical imaging is due to technological development of new imaging modalities and protocols together with an increased scanner distribution.

Most of the contemporary medicines are relying on X-ray CT diagnosis due to its wide availability but X-ray-based medical imaging provides significantly high dose of radiation to the patient population [14]. Since X-rays are a known and proven human carcinogen, this high dose can cause severe biological damage [15].

### **2.1.3 X-ray Depth Dose Distribution**

Since the use of X-ray based medical imaging and treatment is increasing day by day it is important to have a look at how X-ray beam energy is distributed along a certain track. When a Megavoltage photon beam strikes a patient the typical dose distribution on the central axis is shown in figure-2.

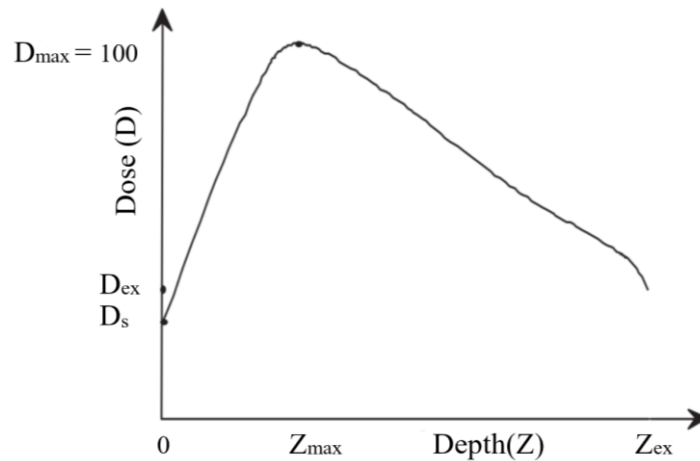


**Figure 2: Dose deposition from a Megavoltage photon beam in a patient.  $D_s$  is the surface dose at the beam entrance side,  $D_{ex}$  is the surface dose at the beam exit side.  $D_{max}$  is the dose maximum often normalized to 100, resulting in a depth dose curve referred to as the Percentage Depth Dose (PDD) distribution. The region between  $Z = 0$  and  $Z = Z_{max}$  is referred to as the dose buildup region [16].**

For a Megavoltage photon beam, the maximum dose is much higher than the surface dose but maximum dose just occurs beneath the patient's surface at a depth  $Z_{max}$ . Both maximum and surface dose depth is dependent on beam energy. Higher the energy lower the surface dose and deeper the  $Z_{max}$ . This relationship and distribution give a general understanding that to treat or image a tumor at a considerable depth we need to apply high energy beam that penetrates more and irradiates healthy tissue before reaching the interest point.

This major drawback of X-ray based medical imaging and treatment has been solved to a large extent after introducing charged particle for the same purposes.

## 2.2 Heavy Charged Particle

Energetic particles having a mass greater than or equal to one atomic mass unit are the heavy particles, in another way heavy charged particle refers to all charged particle except electron and positron. Heavy charged particle includes Alpha particles, protons as well as heavier atomic nuclei from particle accelerators. Charged particle primarily interacts with matter via coulomb force [17]. The positive charge on the particle and the negative charge on electrons that are part of the absorber material create an attraction force. Charged particle transfers momentum while passing by an electron and as a consequence, it slows down and electron gets some kinetic energy.

### 2.2.1 Proton Interaction with Matter

Protons lose most of their energy via inelastic collisions with the outer atomic electrons when traversing matter and that leads ionizations and excitations. There are also elastic collisions with electron and nuclei that deflect protons from their trajectory. However, as proton weigh much more than an electron, the contribution to the energy loss is insignificant. Furthermore

due to Multiple Coulomb Scattering (MCS) proton is deflected by small-angle from the nuclei of the target material. Individual interaction is random and results in a statistical distribution of the principal quantities observed in proton imaging [18]:

- Amount of each proton's energy loss after traversing a layer of given thickness.
- Lateral and angular displacement of the proton from its incident direction.

### 2.2.2 Proton Stopping Power and Linear Energy Transfer (LET)

Stopping power ( $-dE/dx$ ) refers to the average energy loss of the particle per unit path length and measured in MeV/cm. It is dependent on the type and energy of the particle and on the properties of the material it passes. Figure-3(a) illustrates proton stopping power in aluminium.

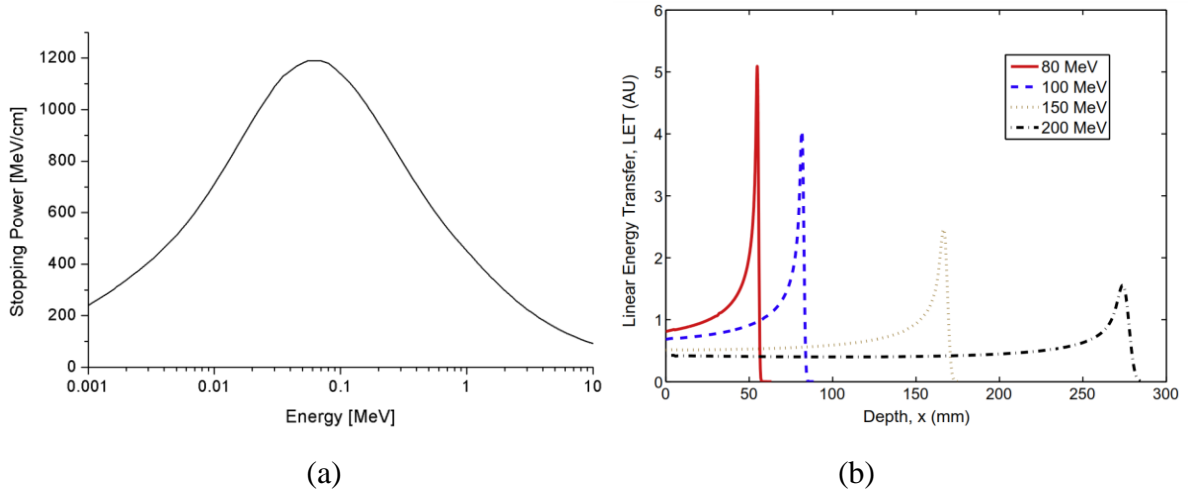


**Figure 3: (a) The stopping power of proton in aluminium, plotted over proton energy [19] (b) LET Vs. depth in liquid water for proton with initial energies of 80, 100, 150 and 200 MeV [20].**

The mean energy loss of charged particle per unit path length which is also called stopping power  $S$ , illustrated in Figure-4(a), is described by Bethe-Bloch theory [21], [22].

$$-\left\langle \frac{dE}{dx} \right\rangle = \frac{4\pi}{m_e c^2} \cdot \frac{nz^2}{\beta^2} \cdot \left( \frac{e^2}{4\pi\epsilon_0} \right)^2 \cdot \left[ \ln \left( \frac{2m_e c^2 \beta^2}{I \cdot (1 - \beta^2)} \right) - \beta^2 \right] \quad (1.1)$$

Where,

$e$  = proton charge

$z$  = charge of the projectile

$\epsilon_0$  = vacuum permittivity

$\beta = v/c$ ;  $v$  is particle velocity and  $c$  is speed of light

$m_e$  = rest mass of electron

$I$  = mean excitation/ionization potential

$n$  = density of electron in the material

$n$  is expressed as,

$$n = \frac{N_A \cdot Z \cdot \rho}{A \cdot M_u} \quad (1.2)$$

Where  $\rho$  = density of material  
 $Z$  = Atomic Number of material  
 $A$  = Mass number of material  
 $N_A$  = Avogadro number  
 $M_u$  = Molar mass constant

LET is linear energy transfer to the material by an ionizing particle in per unit distance, illustrated in figure-3(b), similar to stopping power except that it does not include the delta-rays or effects of radiative energy loss (*i.e.*, Bremsstrahlung). Stopping power and LET are nearly equal for heavy charged particles.

### 2.2.3 Multiple Coulomb Scattering (MCS)

Protons, in the energy range of pCT, experience multiple small angle deflections when passing through the image object. Scattering at the coulomb potential of the target nucleus causes this deflection. It also leads to a random macroscopic deviation up to a few degrees from the original direction and a random displacement up to a few millimeters of the exit point with respect to the entry point. The spatial resolution of proton imaging is limited by MCS [23], [24]. The distribution of coulomb scattering can be explained by Molière theory [25]. For proton CT, the estimation of the trajectory of the particles during image reconstruction is done by gaussian approximation of MCS.

### 2.2.4 Nuclear Interaction

Inelastic nuclear interactions reduce proton fluence with increasing thickness of the object. For pCT, beam with energy above 100 MeV encounters higher probability of nuclear interaction [18]. Nuclear interactions in the object can also generate secondary particles like neutrons, protons are heavier recoil fragments. Energy is locally deposited by recoil fragments. Neutrons can produce another nuclear interaction or exit the patient.

### 2.2.5 Proton and its Depth Dose Distribution

Protons depict an inverted depth-dose profile compared to photons with a maximum (Bragg peak) at the end of the range, shown in figure-4(a). The Bragg curves are the ensuant response of many superimposed depth-dose distributions of the individual particles [26], shown in figure-4(b). Depending on the energy the particle the depth of the Bragg peak in

tissue changes. Bragg peak illustrates the maximum dose deposited in tissue appears close to particle's range [27].

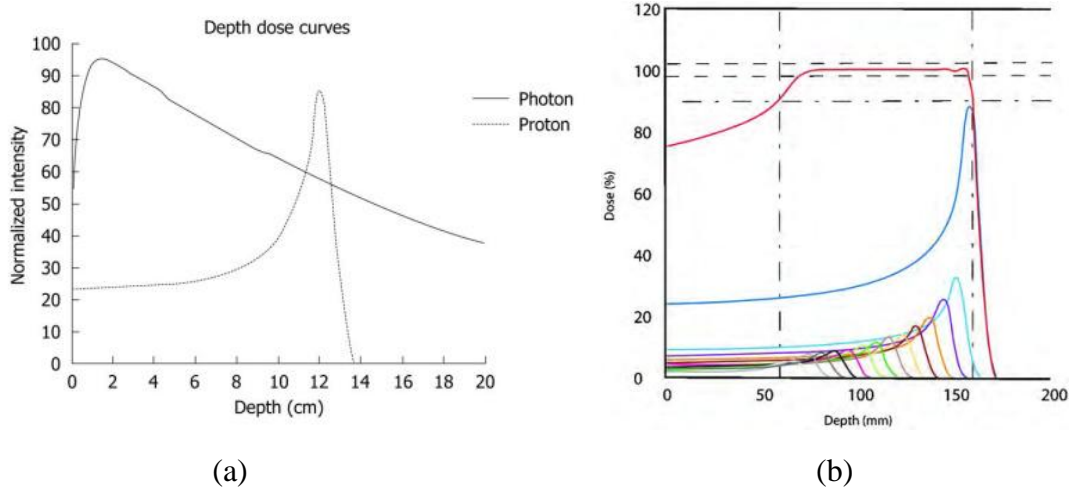


**Figure 4: (a) Depth dose curves for photons and protons. Notice the exponential tail seen in the photon curve that results in dose deposition through the entire patient. The proton curve shows that there is no dose deposition after the Bragg peak [28]. (b) The Spread out Bragg Peak (SOBP). Combining beams with different energies it is possible to describe a longitudinal profile [29].**

### 2.2.6 Potential Advantage of Proton in Radiation Therapy

In 1946 Robert R Wilson first suggested the application of proton in medical physics [30]. He suggested the benefit of treatment with proton because of the energy deposition pattern of protons along their path. Recently, an agile increase in the worldwide availability of proton therapy has been observed. Because of the unique physical properties of protons, compared with the conventional photon therapy, proton therapy offers outstanding advantages in cancer treatment [31]. Basic advantages of proton therapy over photon are,

- In comparison to photons, the main benefit of protons is the lessening of the integral dose to healthy tissue outside the target volume; this is because of Bragg peak (inverse depth-dose profile) of proton beams. Therefore the risk of secondary malignancies including all other radiation-induced side effects is reduced.
- The Relative Biological Effectiveness (RBE<sup>1</sup>) of protons is 1.1 and for photons, it is 1.0, hence protons are biologically more effective than photons. As a result, a lesser dose is needed to produce the equal effect [32].

According to the data, centralized by Particle Therapy Cooperation Group (PTCOG), worldwide there are 66 Proton therapy facilities in operation (last update March 2018) and 43 Proton therapy facilities under construction (update January 2017) and 21 Proton therapy facilities in a planning stage [4].

<sup>1</sup> RBE (Relative Biological Effectiveness): RBE is the ratio of the doses required by two radiations to cause the same level of biological effect.

At present, carbon ion radiotherapy is also in practice for treating deep-seated malignant tumours due to its better dose conformity. Carbon ions are even heavier than proton and give higher RBE nearly 3 [33].

### 2.3 Brief History towards Proton Computed Tomography (Using Energy Loss)

M. Cormack advocated the use of proton for imaging in 1963 [34] for the first time. The first planar radiograph was published by Koehler in 1968. A proton beam was spread by scattering and then directed on to photographic film, for the exposure at the Harvard Cyclotron (Cambridge, MA) [41]. The first image was produced, shown in figure-5(a), where 100-mm pennant-shaped sheet of aluminum was added to generate contrast.

The concept of PCT evolved from marginal range radiography but nuclear scattering imaging and multiple scattering imaging were investigated concurrently [35]. In 1972, M. Goitein explicated the methods to acquire 2-D data and to reconstruct 3-D images with simulation, although this was alpha particle transmission imaging [36]. This was the first example where the charged particle was used in transmission tomography and their energy loss was utilized for contrast. Afterward, an  $\alpha$ -particle scanner was developed and even trialed on humans at the same laboratory [37].

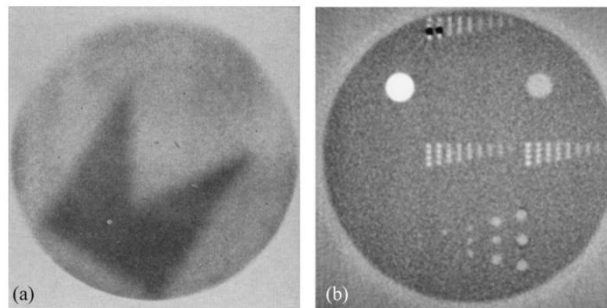


**Figure 5: (a) The first published proton radiograph from 1968 (b) A slice image of a 29 cm diameter phantom from the Los Alamos proton CT scanner in 1978 [38].**

The first human tissue imaging using a high precision range telescope was showed by the Los Alamos National Laboratory (LANL) group of K. M. Hanson et al. in 1982. From their study, pCT was pointed out advantageous over X-ray CT in terms of dose deposition in the tissue [39]–[42]. An early image is given in figure-5(b) where, proton beam energy was 240-MeV. The imaged phantom was comprised of varying size and density inserted plastic cylinder. Two varieties of Detector modules with different functions were utilized, one is Position-Sensitive Detector (PSD) and another one is Residual Energy-Range Detector (RERD). This concept is still used in proton imaging. For tracking each proton position, PSD is used and RERD is for residual energy or range. PSD was a multiwire proportional chamber used in Los Alamos system. PSD determined the exit position of proton at a plane downstream of the phantom. In order to determine residual energy (a “calorimeter”), in early experiments a hyperpure germanium detector was used as a RERD, but later, to determine proton stopping depth (a “range telescope”) a stack of plastic scintillators was used. Undoubtedly this Los Alamos experiment was an advancement both conceptually and experimentally.

In 1990's, interest in proton imaging enhanced with the explicit intent to help with range control and treatment planning for particle beam therapy. Not only in proton beam therapy, in the context of all particle beam therapy as a mean to improve treatment planning, proton-imaging has been investigated. Nowadays X-ray CT images are used in treatment planning and it requires a conversion of the information that comes from the interaction of a photon with a matter, in order to predict the interaction of charged particles in the tissues. As a mean to directly map the relative stopping power of the particle in the tissue, proton imaging has been put forward. For this mapping, the energy loss of the particles is recorded [35].

Due to the ability of direct mapping of relative stopping power of material, proton imaging is considered as one of the alternatives to the conversion of CT number which reduces range uncertainties (voluntary irradiation of the portion of the normal tissue) by checking the expected range with the treatment planning stopping power [35].

## **2.4 Imaging Using Different Properties of the Proton**

Proton imaging by using the energy loss of the particle was not the only explored path, the potential of imaging using other properties of the proton was also investigated parallelly.

### **2.4.1 Marginal Range Radiography**

In marginal range radiography, a mono-kinetic beam of a proton is used and the energy is chosen above 100 MeV so that it penetrates a few centimeters of steel. The rapid change of the specific energy loss ( $\text{MeV/g/cm}^2$ ) near the end of the range of a charged particle is the basis of this type of radiography [43].

The principle of Marginal Range Proton Radiography is illustrated in figure-6 with an object inside a water bath and a radiographic plate at the exit of a water tank. Beam energy is chosen to place the film in the middle of the sharp fluence descent following Bragg Peak.

The marginal range proton radiography was first performed by Koehler in 1968 [44] and then followed by other. In 1973 and 1974 Koehler A. M. and Steward V. W. demonstrated this technique very promising for diagnostic of tumor, strokes or breast carcinoma. In comparison to X-ray radiograph, marginal range proton radiography has better detectability of the malignancies. Despite having some limitation in spatial resolution due to proton scattering, this technique has a higher contrast and even less dose than X-ray for a given energy [35].

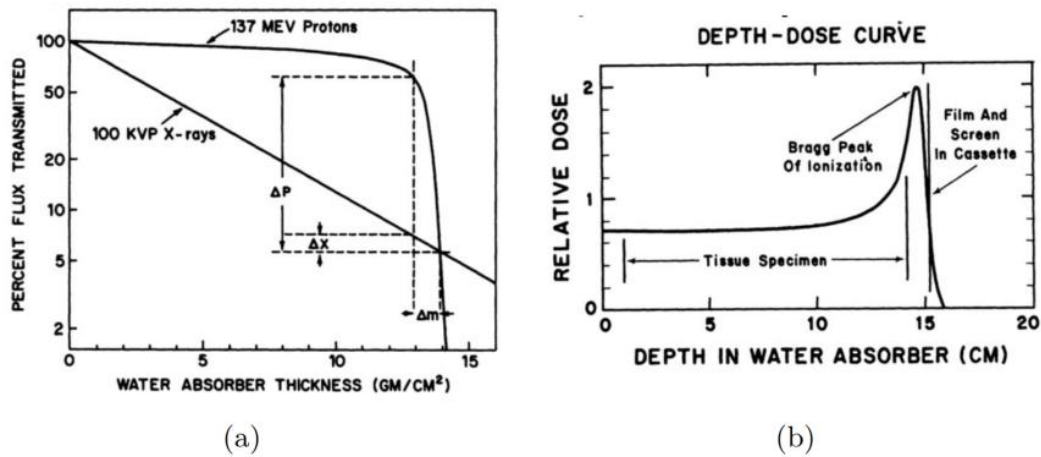


**Figure 6: Illustration of marginal range radiography concept (a) The flux-depth curves for proton and X-rays passing through a homogeneous medium and highlight the higher sensitivity of proton (b) Dose-depth curve for 148 MeV protons in water, showing the Bragg peak of ionization near the end of the particle range. The position of the region examined (tissue specimen) and of the screen-film detector relative to the Bragg peak are indicated [45].**

One of the advantages of heavy ion in radiography is ionization interaction. At the same time, MCS of heavy ion creates a problem by deflecting the particle elastically from their initial line of flight and causes crossovers to occur between adjacent regions. As a result, both spatial resolution and image contrast decreases. This phenomenon can be minimized with a proper match of particle range to the object thickness and by placing the object as near as possible to the image plane [45].

### 2.4.2 Nuclear Scattering Radiography

Nuclear scattering in radiography was first prognosticated in 1975 [46]. This technique uses higher proton energy between 500 MeV to 1 GeV. The idea is to spot protons scattered at wide angles by nuclear interaction. With the help of two position-sensitive detectors, proton's position and direction upstream from the object to image was recorded. Other position-sensitive detectors were used to record the passage of scattered and recoiled protons downstream from the object. The position of the interaction is determined from the intersection of the line describing the trajectory of the incoming and scattered particle. This is how a three-dimensional image is acquired using a single beam direction. Multiple scattering of the secondary protons in the object very much limits the spatial resolution of this technique.

### 2.4.3 Proton Scattering Radiography

This type of radiography depends on MCS and limited to thin object. Image contrast is not as high as it is generated through position dependent scattering. This technique was first explained by West, D. and Sherwood, A. C. in 1972 [47]. The principle of proton scattering radiography is illustrated in figure-7.

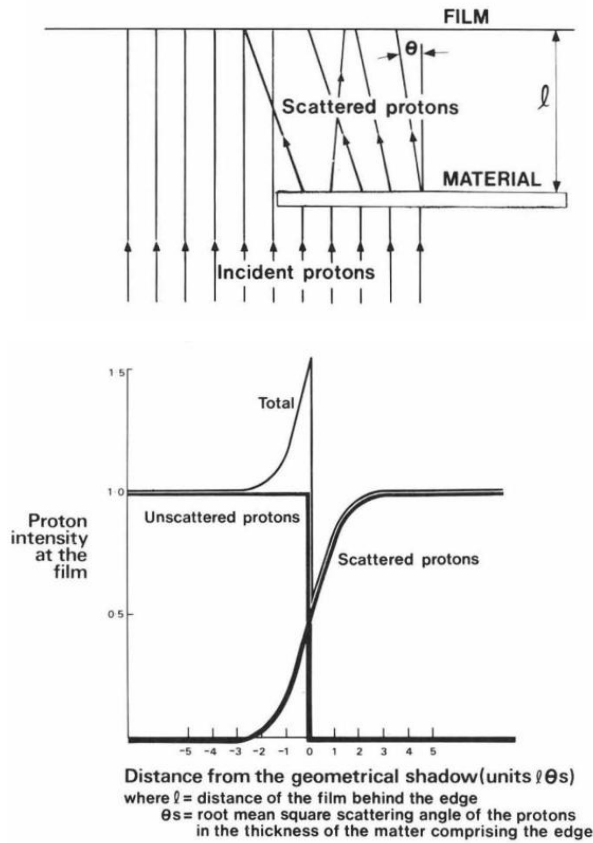


**Figure 7: Principle of proton scattering radiography illustrating intensity distribution near an edge [43].**

The key idea of this imaging was to pass a parallel beam of proton through a uniform depth of material and observe a uniform intensity when particle exits because of having an equal number of coulomb scattering at every point. The same goes for outside of the object. Particles, striking just on the edge of the object are scattered in the non-object part and that's the main reason of less particle detection by the detector at the boundary. This discontinuity generates bright and dark part of the object on radiographic film [47]. Multiple scattering proton radiography was not put forward for clinical application because there was no real interest for its edge-delineation properties found for medical imaging [35].

## 2.5 pCT for Imaging the Relative Stopping Power (RSP)

Charged particle radiography depends on energy loss method. It is based on the residual range of the particles caused by the material being radiographed. Stopping power is energy dependent, so does the RSP, therefore the reconstructed values present an average of particle energy throughout their propagation. For quantification of an image, most of the time it is said that RSP is reconstructed but the precision of estimation of the relative stopping power values is characterized by the “density resolution”.

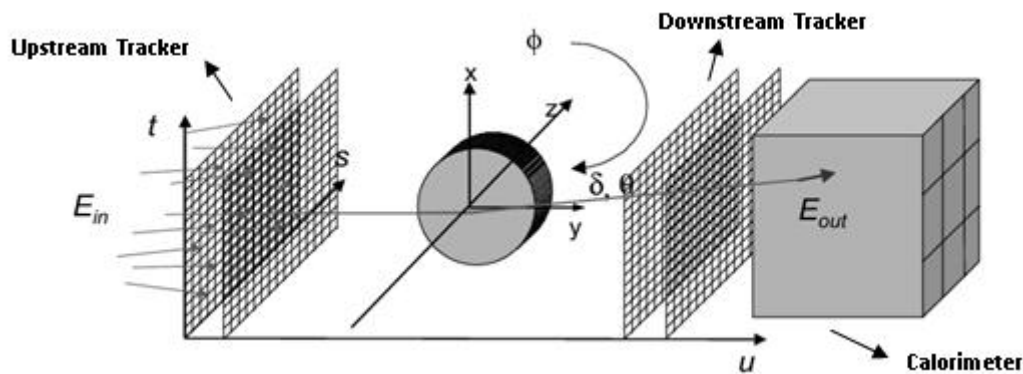


**Figure 8: Schematic of pCT. Protons with known entry energy  $E_{in}$  are recorded one by one in the detector reference system ( $s, t, u$ ) as they traverse the image object from many different projection angles  $\phi$ . The recorded data include entry and exit positions and entry and exit angles as well as exit energy  $E_{out}$  in the energy detector. There are four trackers two upstream, two downstream. Particles are tracked one by one [48].**

### 2.5.1 Phase-1 pCT Scanner (Conceptual pCT Detector Approach)

In proton CT, RSP map is directly acquired from proton energy loss measurement. As a result, it eliminates the associated error in converting the X-ray CT Hounsfield unit to proton RSP. Figure-8 illustrates a pCT system with individual proton tracking facility placed before and after the patient. It provides information regarding direction and position of a proton.

The energy lost by each proton after traversal of the image space is recorded. Also, the position of individual protons is tracked. Specification of proton CT apparatus is given in Table-1. Most commonly a proton CT apparatus consists of a separate system for tracking and energy measurement with,

- Two sets of two tracker planes, upstream and downstream from the object in order to get information on position and direction of each proton.
- A calorimeter or range meter in order to measure the residual energy or range of each proton.

Between 2008 and 2010 the first pCT prototype capable of scanning a head size object was built by collaboration between the Department of Physics at Northern Illinois University, the

Department of Radiation Medicine at Loma Linda University Medical Center (LLUMC), and the Santa Cruz Institute of Particle Physics (SCIPP) at UC Santa Cruz. The design of this system followed the layout shown in figure-8. This system includes front and rear silicon tracker modules, each consisting of 4 XY planes in order to acquire full coordinate and direction data. With the rear tracker modules, energy detector (an array of 18 CsI crystals) is integrated. The scanner is mounted on a rail system at the proton research room at LLUMC to bring the detectors close to the phantom object that rotates on the horizontal proton beam axis. The system is described in more details by R. F. Hurley in this proceeding [49].

**Table 1: Design specifications for a pCT scanner for therapeutic applications [50]**

<b>Category</b>	<b>Parameter</b>	<b>Value</b>
<b>Proton Source</b>	Energy	200MeV (head) 250MeV (trunk)
	Energy Spread	0.1%
	Beam intensity	$10^3 - 10^7$ protons/sec
<b>Accuracy</b>	Spatial resolution	< 1 mm
	Electron Density resolution	< 1%
<b>Time Efficiency</b>	Installation time	< 10 min
	Data acquisition time	< 5 min
	Reconstruction time	< 15 min (treatment planning) < 5 min (dose verification)
<b>Reliability</b>	Detector radiation hardness	> 1000 Gy
	Measurement stability	< 1%
<b>Safety</b>	Maximum dose per scan	< 5 cGy
	Minimum distance to patient surface	10 cm

### 2.5.2 Design Specification

The design specifications of a pCT scanner used in proton therapy are presented in Table-1. The needs for accurate and safe proton beam delivery dictate the requirements of a pCT system designed for applications in proton therapy.

For imaging, it is important to have sufficient energy of proton to penetrate the body part to be imaged. According to the NIST PSTAR database [51], 200 MeV proton is sufficient to penetrate the adult human skull and 250 MeV is sufficient to penetrate an adult trunk.

The accuracy of measured position and direction is given by spatial resolution that has an impact in the reconstructed image. In order not to compromise with the system's overall

performance, the spatial and energy uncertainties of the pCT system should considerably be smaller than those imposed by the physical limitations. For therapy with protons, a clinically meaningful spatial resolution is about 1 mm [52].

To have a short installation, calibration, scanning, and removal time a pCT system should be time-efficient. If the detectors are not sufficiently radiation hard to stay in the beam line permanently then installation and removal of the system are required. The scanning time of a patient for treatment planning should not be longer than 15 min (including installation and removal of an impermanent system but excluding image reconstruction time) [50].

Detectors need to have sufficient radiation hardness in order to sustain their function within 1% of specified performance values for at least one year, ideally for 5 years or more. Furthermore, the system is expected to be insensitive to changes in temperature, humidity, and magnetic fields present in the treatment room [50].

### **2.5.3 Proton Tracking System and Energy/Range Measurement**

Proton tracking system is based on three basic criteria [35]:

- Spatial resolution that determines the accuracy of measured direction and position.
- A ratio between the thickness and radiation length is called material budget of the tracker planes. The material budget determines the amount of scattering the proton undergoes as well as the additional uncertainty on the measured direction.
- For event-by-event proton tracking, one of the essential factors is time resolution and readout performance. There is no parameter to measure the exact requirement of these criteria as an image has multiple impacts by different parameter.

Nevertheless, for perfect imaging, best spatial resolution, lowest material budget and fastest acquisition rate are looked for. Prototypes have been developed following different approaches.

Table-2 is a summary of all prototype systems. This represents the current state of the field. However, most of the systems are in continued development and yet to reach a meticulous summary.

**Table 2: A summary of current and recent Proton Radiography (PRG)/Proton CT (pCT) prototypes [38]**

<b>Group</b>	<b>Year of reference</b>	<b>Area (cm<sup>2</sup>)</b>	<b>Position-sensitive detector technology (number of units)</b>	<b>Residual energy-range detector technology</b>	<b>Proton rate (Hz)</b>	<b>pCT or pRG</b>
<b>Paul Scherrer Institute</b>	2005	22.0 ×3.2	x-y Sci-Fi (2)	Plastic scintillator telescope	1 M <sup>a</sup>	pRG
<b>LLU/UCSC/NIU</b>	2013	17.4 ×9.0	x-y SSD (4)	CsI (Tl) calorimeters	15 k <sup>a</sup>	pCT
<b>LLU/UCSC/CSUSB</b>	2014	36.0 ×9.0	x-y SSD (4)	Plastic scintillator hybrid telescope	2M <sup>a</sup>	pCT
<b>AQUA</b>	2013	30.0 ×30.0	x-y GEMs (2)	Plastic scintillator telescope	1 M <sup>a</sup>	pRG
<b>PRIMA I</b>	2014	5.1 ×5.1	x-y SSD (4)	YAG: Ce calorimeters	10 k <sup>a</sup>	pCT
<b>PRIMA II</b>	2014	20.0 ×5.0	x-y SSD (4)	YAG: Ce calorimeters	1 M	pCT
<b>INFN</b>	2014	30 ×30	x-y Sci-Fi (4)	x-y Sci-Fi	1 M	pCT
<b>NIU/FNAL</b>	2014	24.0 ×20.0	x-y Sci-Fi (4)	Plastic scintillator telescope	2 M	pCT
<b>Niigata University</b>	2014	9.0 ×9.0	x-y SSD (4)	NaI(Tl) calorimeter	30 <sup>a</sup>	pCT
<b>PRaVDA</b>	2015	9.5 ×95	x-u-v SSD (4)	CMOS APS telescope	1M	pCT

**AQUA**= Advanced Quality Assurance; **CMOS APS**= Complementary Metal Oxide Semi-conductor Active Pixel Sensor; **CsI:Tl**= Thallium-doped Caesium Iodide Scintillator; **CSUSB**= California State University, San Bernardino; **INFN**= Istituto Nazionale di Fisica Nucleare; **FNAL**= Fermilab National Accelerator Laboratory; **LLU**= Loma Linda University; **NaI:Tl**= Thallium-doped Sodium Iodide Scintillator; **NIU**= Northern Illinois University; **PRaVDA**= Proton Radiotherapy Verification and Dosimetry Applications; **PRIMA**= PROton IMAGING; **Sci-Fi**= Scintillating Fibre Hodoscope; **CSC**= University of California Santa Cruz; **x-y (or x-u-v) SiSDs**= Two-plane (or Three-plane) Silicon Strip Detectors; **YAG: Ce**= Cerium-doped Yttrium Aluminium Garnet Scintillator.

## 2.6 Expected Performance of PCT

### 2.6.1 Path Estimation and Spatial Resolution

The proton path in an object is affected by MCS, illustrated in figure-9. It makes reconstruction of pCT images challenging and spatial resolution much less satisfying than X-ray CT.

The first proton path estimation approach was taken considering only the position of the particle on the calorimeter in a similar fashion of X-ray CT [39] illustrated in figure-10(a). It is possible to define a straight line trajectory of a proton by adding position sensitive tracker before and after the object [53], illustrated in Figure-10(b). Recording angle of the particle with more trackers can give a trajectory with broken straight lines [54], shown in Figure-10(c) and this is how the idea of curved path began.

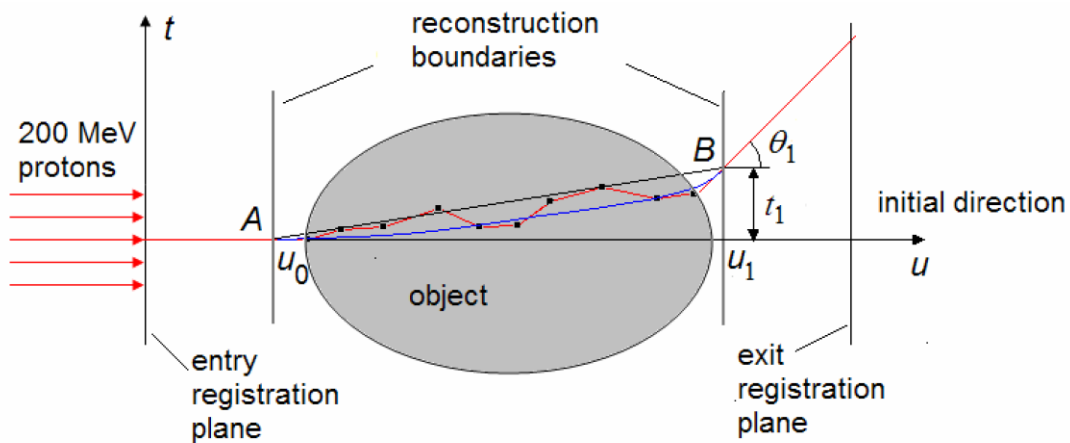


**Figure 9:** The path of protons traveling inside an object is determined by a multitude of individual scattering events leading to a zigzag path (red). Both the position and direction of entry and exit proton are registered. Given the object boundary, the intersecting points  $A$  and  $B$  of a proton with the object can be obtained. While the intersecting points are sufficient to estimate the straight line path (black) of the proton, additional knowledge of the entry and exit directions permits estimation of the most likely path (blue line) [55].

There were three different approximations on path trajectory of proton,

- **Straight-Line Path (SLP)** — SLP is the simplest estimation of the proton path. This is the intersection line between the entry and exit of each proton illustrated in figure-10(a).
- **Most-Likely Path (MLP)** — Proton's internal path is followed by a certain probability distribution. An object with homogeneous electron density over the entire scan region and both directions of entry and exit point is known then MLP of all possible trajectories can be analytically derived. MLP considers that the object has scattering and energy loss properties like water [24]. MLP is shown in figure-10(d)
- **Cubic Spline Path (CSP)** — When the positions and tangential directions of the proton at the entrance and exit are known, despite considering MLP as the best

statistical estimate for proton path through a uniform medium, an alternative simpler method can be used to fit the two endpoints with a smooth polynomial. A cubic spline is used to estimate the cubic spline path or CSP.

The SLP, MLP, and CSP estimators of the proton paths are iterative reconstruction algorithm. Compared to analytical image reconstruction, algebraic method based iterative image reconstruction is advantageous. MLP gives better spatial resolution than CSP and SLP [55]. The sub-milimetric spatial resolution can be reached, shown by published studies when considering few centimeters thick object and energies greater than 100 MeV for proton beams [56]–[58].

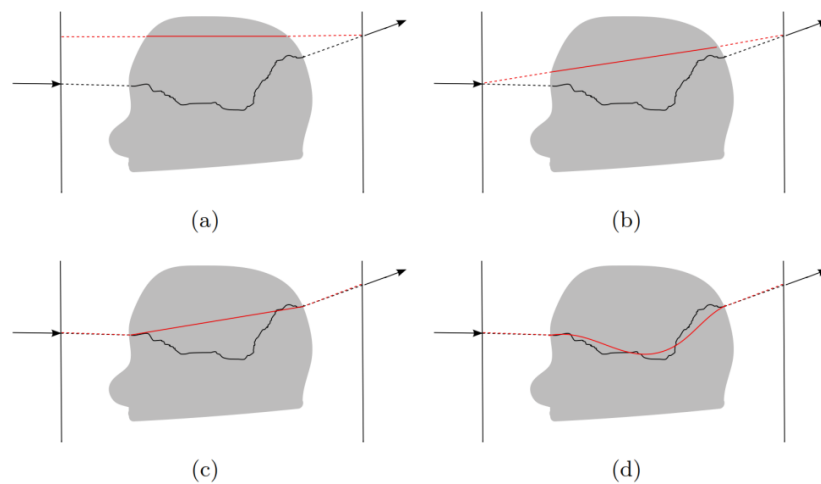


**Figure 10: Illustration of different path estimations for image reconstruction. In black the proton trajectory, in red estimation made: (a) knowing only the position on downstream detector; (b) knowing the positions upstream and downstream from the object; (c) knowing the position and direction upstream and downstream from the object; (d) estimating the most likely path using the position and direction upstream and downstream from the object [35].**

### 2.6.2 Dose and Density Resolution

For an improved treatment planning, reconstructed relative stopping power resolution should be less than 3% achievable with X-ray CT (1% ideal). Density resolution of pCT depends on proton energy and per voxel<sup>2</sup> proton number in the reconstructed image. There's always a trade-off between delivered dose and density resolution [59], [60].

Lower energy protons lose more energy that is responsible for higher dose deposition and greater contrast whereas for higher energy protons, the effect of multiple scattering is ignorable and more protons are used to calculate average energy loss. Therefore, there is always a compromise between energy and number of particle needed but most of the cases higher energy proton is chosen because of less scattering.

<sup>2</sup> Voxel: A unit of graphic information that refers a point in three-dimensional space.

## **2.7 Next-Generation pCT**

### **2.7.1 Digital Tracking Calorimeter (DTC)**

The currently used detector approach for pCT is discussed in section-2.5. Next generation pCT design is working to merge these separate systems for tracking and energy measurement into one robust system and that is named as DTC.

The high-granularity digital sampling pixel detector was developed at CERN. To measure the particle distribution at large rapidity an electromagnetic calorimeter is designed as a part of the proposed upgrade of detector experiment [61]. The high pixel granularity helps to discriminate particle at high momenta. The designed DTC prototype with 24 telescopic sensor layers has been tested for pCT purpose at the proton accelerator at Kernfysisch Versneller Instituut-Center for Advanced Radiation Technology (KVI-CART) in Groeningen, Netherlands [3]. After that, simulation-based research work has been carried out to see how the DTC performs in a therapeutic particle beam [62]. The DTC consists of multiple layers of Monolithic Active Pixel Sensor (MAPS) chips with digital readout. The detail discussion about MAPS is presented in Chapter-3.

## CHAPTER-3 MONOLITHIC ACTIVE PIXEL SENSOR (MAPS)

Monolithic pixel sensors were proposed as a viable substitute to Charge-Coupled Device (CCD) for visible imaging, in the early 1990s [63]. These sensors are often called CMOS imagers because of being made in a standard Very Large Scale Integration (VLSI) technology [64]. Two main types of sensors are:

- Passive Pixel Sensor (PPS): With an integrated photodiode in a pixel together with selection switches to connect the photodiode directly to the output line for readout.
- Active Pixel Sensor (APS): With an integrated amplifier in each pixel to directly buffers the charge signal.

Because of better performance, most CMOS imagers have an APS structure. Also, several advantages of CMOS APS, or Monolithic Active Pixel Sensors (MAPS), were immediately recognized:

- MAPS avoids the drawbacks of bump-bonding or other types of connections [65].
- Making very small pixel size and integrating more functionality in the same pixel is possible because of shrinking size of transistor [65]–[68].
- MAPS usually have low power consumption [65].
- MAPS allows integration of multiple functionalities on the same chip together with the sensor arrays that simplify system level and hence reduce the costs. Random access to pixels ensure tracking of very high-speed object but there is a trade-off between resolution or array size and readout speed [69].
- The readout is always massively parallel to analog-to-digital conversion [66]–[68].
- Limiting the readout system requirements to digital I/Os, MAPS can be made very easy to use [65].

In particle physics experiments, sensors and readout electronics that are used for vertexing and tracking require high performance in terms of granularity, read-out speed, material thickness, radiation hardness and power consumption. Silicon (Si) semiconductor technology based sensor and CMOS technology based readout electronics accomplished majority of the above requirements but the shortcoming was the interface between the sensor and the readout electronics, i.e. typically separate components. This limitation was eliminated by merging both sensor and read-out electronics into a single detection device that introduces CMOS MAPS [70]. Figure-11 illustrates the cross section scheme of MAPS.

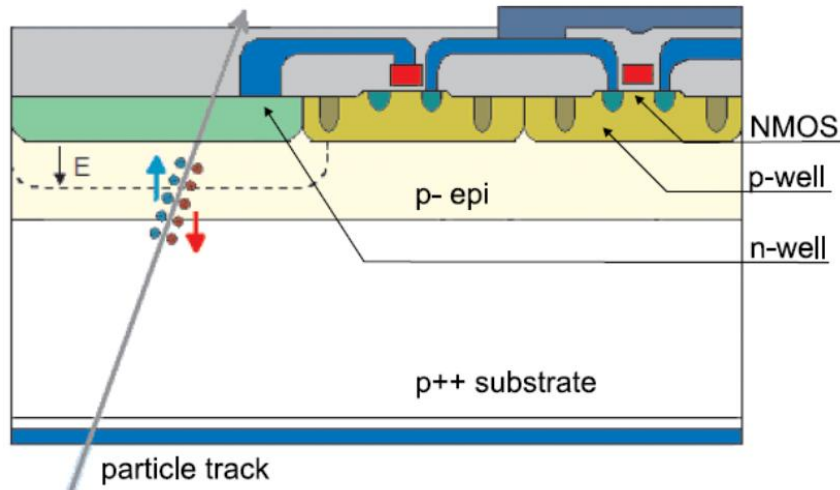


Figure 11: Cross section scheme of a MAPS pixel combines Si sensor and CMOS read-out electronics in a single volume [71].

### 3.1 Interaction of Particles with Silicon Sensor

Charged particle interacts with the material of the sensor to generate charge carriers. Detection of these charge carriers ascertains the detection principle of semiconductor detectors.

#### 3.1.1 Energy Loss of Charged Particle

When a charged particle passes through the sensor, it collides with the electrons of the interacting medium. For heavier particle than an electron, average energy loss due to this scattering process is expressed by the Bethe-Bloch formula (cf. section-2.2.2).

Energy loss of particles, much heavier than an electron, depends on the velocity of the crossing particle. At high energy, Lorentz factor<sup>3</sup> ( $\gamma$ ) cannot be neglected. For electrons and positrons, the Bethe-Bloch formula is corrected for interaction between identical particles and further energy-loss mechanism, like bremsstrahlung.

For low energies, the dominating factor for energy loss is  $1/\beta^2$  ( $\beta$  = speed of light). Energy loss from the Bethe-Bloch equation-1.1 reaches a minimum when a particle with  $\beta\gamma \sim 3$ . A particle in such energy conditions is called a Minimum Ionizing Particle (MIP).

##### 3.1.1.1 Energy Loss Distribution

Large fluctuations of the energy loss occur because of the statistical nature of the ionizing process during the passage of a fast charged particle through matter [72]. Bethe-Bloch formula provides the average energy-loss per path unit and the probability distribution of the

<sup>3</sup> Lorentz factor ( $\gamma$ ) – This is a factor by which; a moving object changes its length, time and relativistic mass.

energy loss is defined by absorber thickness [73]. Thick absorbers give gaussian distribution whereas thin absorbers show asymmetric distribution because of higher energy fluctuation. For silicon sensors, theoretical calculation of energy loss distribution was carried out by Landau and Vavilov [74], [75]. To produce an electron-hole pair the average energy needed for silicon is equal to 3.68 eV [72]. Figure-12 shows the landau distribution for a charged particle in silicon.

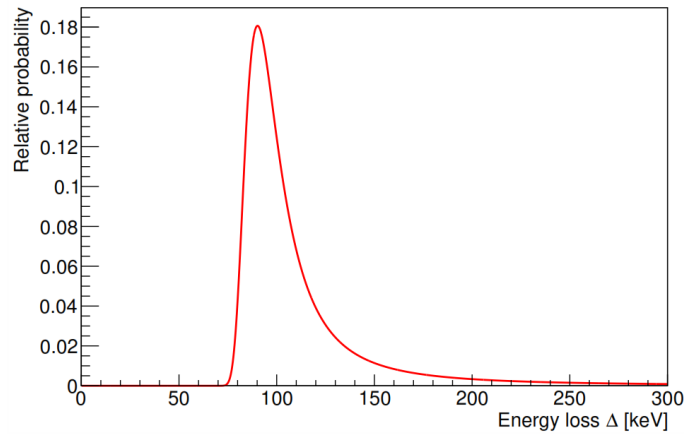


**Figure 12: Landau distribution of the energy loss of highly relativistic particles ( $\beta\gamma \gg 100$ ) in a silicon layer of 320  $\mu\text{m}$  thickness [76].**

While traversing a detector, charged particles suffer from MCS apart from energy loss. Successive small angle deflections by this scattering causes small deviations of the track. The scattering angle ( $\Theta$ ) gives a gaussian distribution [77] with a root mean square

$$\sqrt{\langle \theta^2 \rangle} = \frac{13.6 \text{ MeV}}{\beta p c} z \sqrt{\frac{X}{X_0}} \left[ 1 + 0.038 \log \frac{X}{X_0} \right] \quad (3.1)$$

Where,  $\beta$  = Velocity;  $P$  = Momentum;  $z$  = Charge of the particle

$X/X_0$  = Thickness of absorption medium in unit of radiation length

### 3.1.2 Energy Loss of Electromagnetic Radiation

Electromagnetic radiation interacts with semiconductor detectors mainly via three processes [78]:

- Photoelectric Effect
- Compton Effect
- Pair Production

In these interactions, photons are either completely absorbed in a single process (photoelectric effect and pair production) or scattered by relatively large angles (compton

effect). The attenuation of monochromatic photon beam in intensity while traversing the sensor is given by [73]

$$I(x) = I_0 e^{-x/\mu} \quad (3.2)$$

Where,  $I_0$  = Intensity of incident beam;  $x$  = Thickness of traversing medium

$\mu$  = Attenuation length

The photoelectric effect is the dominant process at energy below 100 keV for silicon. Compton scattering process becomes dominant at higher energies. Figure-13 shows the photon cross section in silicon. Silicon is used for detecting photon with energy up to 100 KeV.

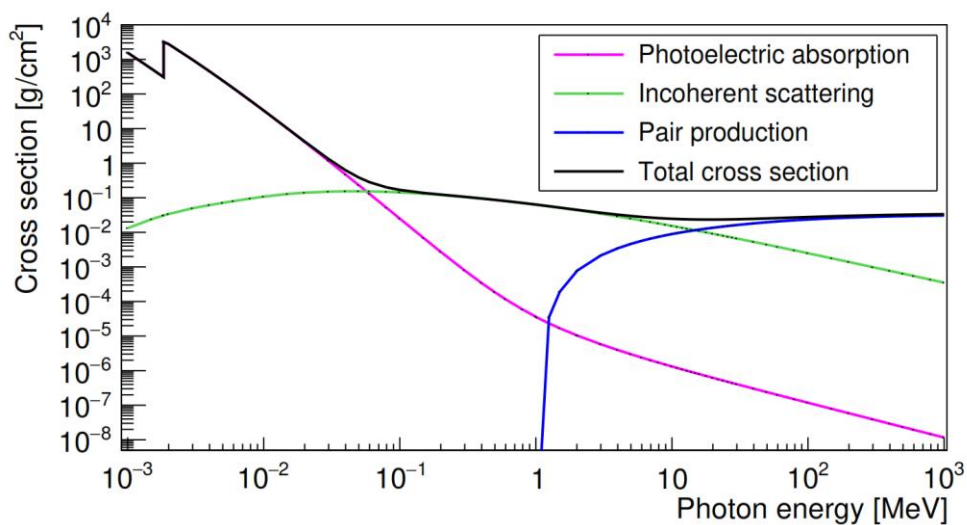


Figure 13: Total photon cross section in silicon [71].

### 3.1.3 Detection Principle of MAPS

Electron-hole pairs are generated near the point of interaction when electromagnetic radiation interacts with the semiconductor. Due to applied reverse bias or diffusion caused by concentration variation, these charge carriers move by drift and collected by the electrode associated with the front end readout electronics. In standard MAPS, charges are collected by diffusion. Impinging particles generate charge carrier in the epitaxial layer. Because of the potential barrier between the lightly doped p-type epitaxial layer and the heavily doped p-type substrate, generated electrons are deflected. On the other hand, the containment of the majority of the electrons within the epitaxial is due to a similar potential barrier between the lightly doped epitaxial layer and the heavily doped p-wells of the NMOS transistors. When diffusing electrons reach the built-in electric field at the junction which is formed by the n-well of the sensing diode and the p-type epitaxial layer, they are collected as a signal [73].

## 3.2 ALPIDE

As a high performing MAPS, ALPIDE is the most advanced sensor that is developed for the particle tracking of ALICE experiment at CERN [79]. The ALPIDE pixel chip is manufactured using the commercial 0.18  $\mu\text{m}$  CMOS imaging sensor process by TowerJazz [80]. AC-sensitive low power front-end coupled with a hit-driven in-matrix zero-suppression circuit makes it less power consuming and much faster than the typical MAPS [79]. ALPIDE chip has a pixel matrix of  $1024 \times 512$  pixels and total thickness is thinned down to 50  $\mu\text{m}$  [81]. A schematic cross section of ALPIDE sensor is shown in figure-14.

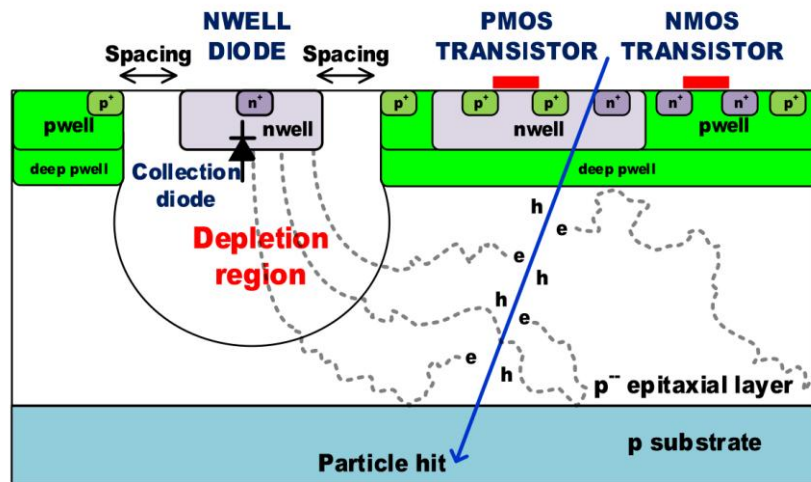


**Figure 14:** Schematic cross section of pixel of MAPS (TowerJazz 0.18  $\mu\text{m}$  imaging CMOS with the deep p-well feature) [73], [82], [83].

### 3.2.1 ALPIDE in Pixel Architecture

The ALPIDE sensor features the option to embed an n-well on top of a deep p-well (cf. figure-14) and this is how the active volume i.e. the epitaxial layer, becomes separated from all n-wells except for the collection diodes. This separation creates the possibility to implement PMOS transistors inside the pixels with no deterioration of the charge collection efficiency [71]. A pixel sensor consists of following parts [73],

**Substrate:** lowest layer of a pixel that is made of highly doped (p-type), low resistivity crystalline silicon. The substrate provides mechanical stability to host all other structures.

**Epitaxial layer:** This is the layer top of the substrate which is lightly doped (p-type) and provides an active volume of the detector where impinging particles generate charge carriers. This layer is implanted with all active devices.

**Well implantations:** To integrate PMOS and NMOS transistors, N-well and p-well implantations are used.

**Diffusion implantations:** Source and drain of the transistors are formed by them. They have higher doping in comparison to the wells in which they are embedded into.

**Collection diode:** Generated charge collecting diode. The depletion region is formed in the junction between the diode n-well and the p-epitaxial layer.

**Metal lines:** Different silicon structures are connected by them. They are generally used as an insulator and made of aluminium or copper and embedded into silicon oxide.

Some benefits of 0.18  $\mu\text{m}$  CMOS technology are [73],

- With transistor feature size of 0.18  $\mu\text{m}$  and gate oxide thickness below 4 nm, CMOS process becomes substantially more robust to Total Ionising Dose (TID) than other technologies.
- This technology provides 6 metal lines that allow implementing high density and low power digital circuits with a reduced area for the digital circuitry at the periphery of the pixel matrix. As a consequence insensitive area of the pixel chip is reduced.
- Epitaxial layers can be developed with resistivity from 1  $\text{K}\Omega \text{ cm}$  to 6  $\text{K}\Omega \text{ cm}$ . This makes bigger depletion area in the epitaxial layer and improves the signal to noise ratio of the sensor as well as its resistance to nonionizing radiation.
- The Material Budget<sup>4</sup> can be reduced to a great extent by producing wafers with an epitaxial layer from 18  $\mu\text{m}$  to 40  $\mu\text{m}$  thicknesses and making chips thin up to 50  $\mu\text{m}$ .
- The most important feature of this technology is the use of a deep p-well. Parasitic charge collection by n-wells is a problem that the front-end electronics face. To eliminate this problem deep p-well is used. The PMOS transistor embedded in n-well is fabricated on top of the deep p-well.
- The stitching technology for the sensors production is one of the unique features that help manufacturing of die sizes up to a single die per 200 mm diameter wafer.

### 3.2.2 ALPIDE Pixel Matrix Architecture

In-pixel architecture of ALPIDE is quite complex. Each pixel includes its own amplifier and shaper, connected to a comparator and multiple hit buffers. To perform zero-suppression<sup>5</sup> within matrix an Address-Encoder Reset-Decoder (AERD) circuit, illustrated in figure-15(b), is engaged. The same readout-circuitry is shared by two neighboring columns as depicted in figure-15(a). AERD circuit ensures propagation of hit pixel's address to the end-of-column logic and resetting the corresponding in-pixel hit buffers. In this architecture, pixels are read in a continuous acquisition mode [80] or by an external trigger controlled mode (global-shutter mode). The ALPIDE architecture is by design hit-oriented and allows less power-consumption, shorter integration time and smaller pixels pitches with a total chip dimension of 15 mm  $\times$  30 mm.

---

<sup>4</sup> Material Budget ( $X/X_0$ )- This is the ratio of radiation length of a particle in a material ( $X$ ) and radiation length ( $X_0$ ) required by the relativistic charged particles to reduce its energy by the factor  $1/e$  [105].

<sup>5</sup> Zero-Suppression- This indicates reading only the hit pixels.

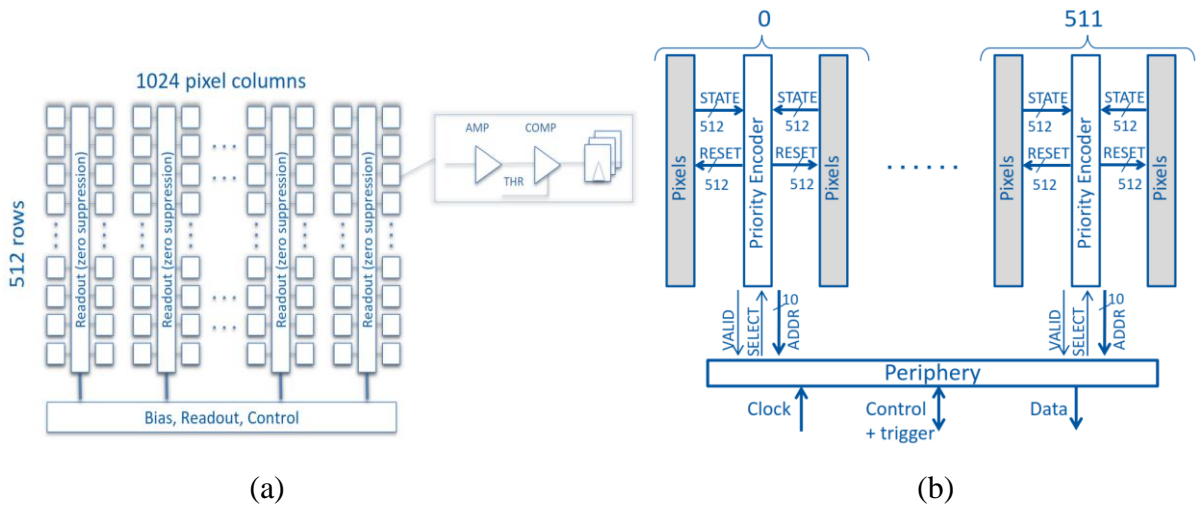


**Figure 15: (a) Schematic of a full scale ALPIDE chip (1024 pixel column x 512 row): pixels are arranged in double columns (b) with a priority encoder per double column. This allow space to be used more efficiently for the priority encoder as it is routing dominated and several routing lines can be shared between the two columns [82].**

### 3.2.3 ALPIDE Readout Architecture

Readout of a detector indicates the detection of a particle when it crosses a pixel. This information is acquired by setting a collection node threshold to the analog signal [73]. In ALPIDE, the available digital information in a pixel is fed into an encoder circuit to generate the address of a hit pixel directly. The 32 regions of pixel matrix (each region is a matrix of  $512 \times 32$  pixels) are read out in parallel shown in figure-16. The pixel is reset to move to the next valid one and until all pixels are read out this procedure is iterated. The ALPIDE chip uses a global strobe signal in order to capture the comparator front-end output into a local memory thus provides effective integration time of about  $4 \mu s$  [73] with given front-end shaping time  $1-2 \mu s$  [82].

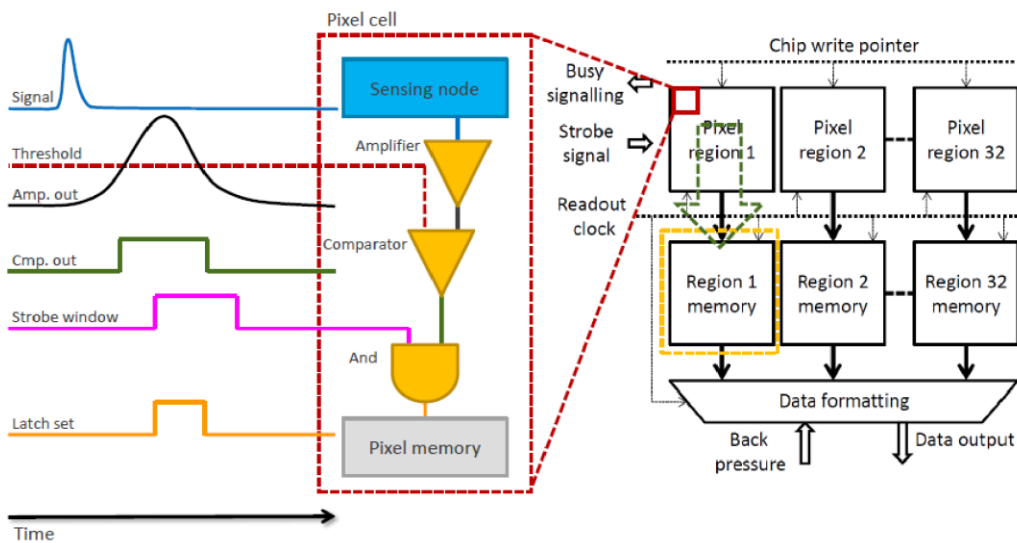


**Figure 16: Readout organization of the chip with details on the pixel cell [82].**

### 3.3 The ALPIDE Family

#### 3.3.1 ALPIDE Prototypes

Different ALPIDE prototypes with their key specifications are described in Table-3. The improvements were done from one prototype to another over several years keeping all features provided by the TowerJazz CMOS process.

**Table 3: The prototypes of the ALPIDE family [80]**

Year	Prototype	Specification
2012	Explorer	<ul style="list-style-type: none"> <li>➤ analog readout</li> <li>➤ <math>20 \times 20 \mu\text{m}^2</math> and <math>30 \times 30 \mu\text{m}^2</math> pixels</li> <li>➤ pixel and collection-electrode geometry</li> <li>➤ reverse substrate bias</li> <li>➤ radiation hardness</li> </ul>
2013	pALPIDE <sub>ss</sub> -0	<ul style="list-style-type: none"> <li>➤ Matrix with 64 columns x 512 rows</li> <li>➤ <math>22\mu\text{m} \times 22 \mu\text{m}</math> pixels</li> <li>➤ In-pixel discrimination and buffering</li> <li>➤ Zero suppression within pixel matrix</li> </ul>
2014	pALPIDE-1	<ul style="list-style-type: none"> <li>➤ First full-scale prototype</li> <li>➤ Pixel pitch: <math>28 \mu\text{m} \times 28 \mu\text{m}</math></li> <li>➤ 4 sectors with pixel variants</li> <li>➤ 1register/pixel, no final interface</li> <li>➤ on-chip bias DACs</li> </ul>
April 2015	pALPIDE-2	<ul style="list-style-type: none"> <li>➤ 4 sectors with pixel variants</li> <li>➤ Optimization of circuits</li> <li>➤ Allowing integration in ITS modules</li> <li>➤ No high-speed serial output</li> </ul>
October 2015	pALPIDE-3	<ul style="list-style-type: none"> <li>➤ 8 sectors with pixels variant</li> <li>➤ front-end optimisation</li> <li>➤ three in-pixel hit buffer per pixel</li> <li>➤ high-speed link</li> </ul>
August 2016	ALPIDE	<ul style="list-style-type: none"> <li>➤ Single pixel variant</li> <li>➤ All features and optimization</li> </ul>

### 3.3.2 Pixel Chip Requirement

Table-4 shows the pixel chip requirement for ALPIDE. The ALPIDE development aims to reduce power density well below  $100 \text{ mW/cm}^2$  and integration time shorter than  $30 \text{ }\mu\text{s}$  [83].

**Table 4: Pixel chip requirement for ALPIDE [83]**

Parameter	Value
Chip Size	$15\text{mm} \times 30\text{mm}$
Silicon Thickness	$50\mu\text{m}$
Pixel Size	$(30 \times 30) \mu\text{m}^2$
Readout Time	$< 30 \mu\text{s}$
Power density	$< 100 \text{ mW/cm}^2$
Detection Efficiency	$> 99\%$
Fake Hit Rate	$< 10^{-5}$ per readout frame and pixel
TID Radiation Hardness	$2.7 \text{ Mrad}$
NIEL Radiation Hardness	$1.7 \times 10^{13} \text{ MeVn}_{\text{eq}}/\text{cm}^2$

## 3.4 ALPIDE Principle of Operation

### 3.4.1 In-pixel Hit Discrimination

The signal-flow inside the pixel circuitry of ALPIDE can be shown by simplified block diagram, illustrated in figure-17. At the input node PIX\_IN, the charge signal is integrated with a typical collection time of  $\sim 10 \text{ ns}$  [83]. The amplitude of PIX\_IN voltage signal is equal to the ratio of  $Q_{\text{IN}}$  to  $C_{\text{IN}}$  where  $Q_{\text{IN}}$  is collected charge and  $C_{\text{IN}}$  is total input capacitance. It takes around  $1 \text{ ms}$  for the reset circuit to restore the input baseline voltage level. The front-end amplify the signal and operate as a delay line with a peaking time of around  $2 \text{ }\mu\text{s}$ . If output OUT\_D coincides with STROBE signal then the hit information is latched in the multi-event buffer memory. By a hit-driven architecture, the data is read out only when there are stored hits.

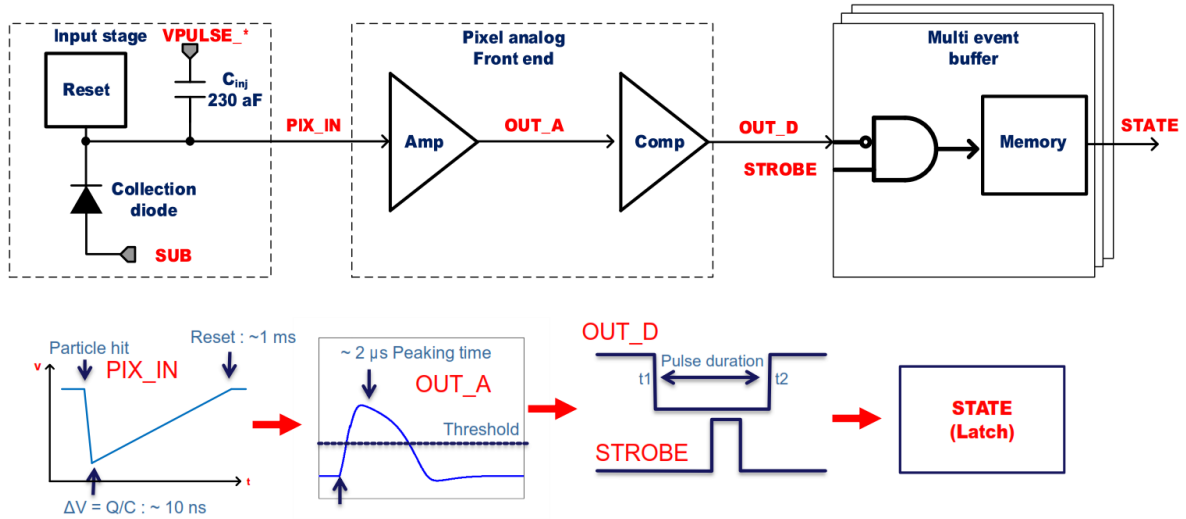


Figure 17: In-pixel hit discrimination block diagram and signal flow [83].

### 3.4.2 ALPIDE Front-End Circuit

The ALPIDE in-pixel front-end circuitry consists of an analog part and a digital part [76]. The analog part mainly shapes and discriminates the signal and digital part contains the hit register and further logic to test and mask (disable) the pixel. The front-end circuitry is similar for all prototypes based on the ALPIDE architecture but in the final ALPIDE chip the analog front-end is slightly optimized that is attached in the section-A.1.

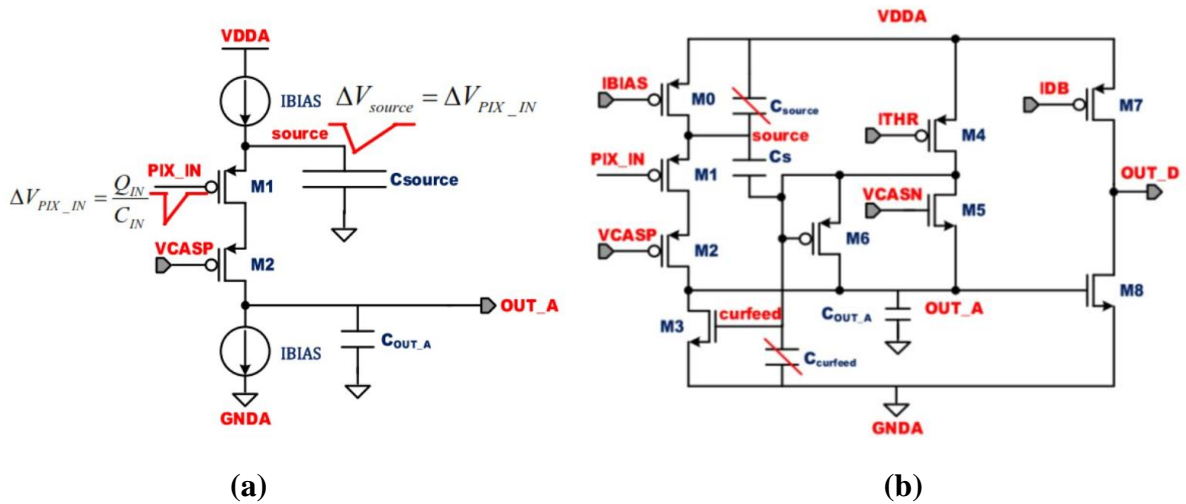


Figure 18: Pixel analog front end schematic for ALPIDE (a) principle (b) presented circuit [80], [83].

### 3.4.3 Pixel Analog Front-End

Figure-18 illustrates the in-pixel analog front-end. The working principle of analog front-end is based on charge transfer. Charges are transferred to a small capacitor in order to generate voltage gain [83]. A negative voltage step at the input node PIX\_IN created by charge signal is expressed as,  $\Delta V_{PIX\_IN} = Q_{IN}/C_{IN}$ . The M1 transistor works as a source follower with current source IBIAS (cf. section-3.4.3.2) from VDDA. Also, source voltage is being forced to follow the M1 gate voltage. This results in charge transfer,  $Q_{source} = C_{source} \cdot \Delta V_{PIX\_IN}$  from  $C_{source}$  to  $C_{OUT\_A}$  if IBIAS current sink to GNDA. So apparently  $\Delta V_{OUT\_A}$  is,

$$\Delta V_{OUT\_A} \approx \frac{Q_{source}}{C_{OUT\_A}} = \frac{C_{source} \Delta V_{PIX\_IN}}{C_{OUT\_A}} = \frac{C_{source}}{C_{OUT\_A}} \Delta V_{PIX\_IN} = \frac{C_{source}}{C_{OUT\_A}} \frac{Q_{IN}}{C_{IN}} \quad (3.3)$$

A large Voltage gain is obtained with  $C_{source} \gg C_{OUT\_A}$

Figure-18(b) shows the practical implementation of analog front-end circuit. A low-frequency feedback generated using transistor M4 and M5 and called curfeed net. Curfeed net is loaded with  $C_{curfeed}$  capacitance and connected to the gate of M3. This is also adjusted for M3 to absorb IBIAS+ITHR current. The baseline value for OUT\_A and the reset to baseline after particle hit is defined by voltage bias VCASN and current bias ITHR. The gate of M8 transistor is controlled by OUT\_A and baseline is defined in a way that  $I_{M8} < I_{DB}$ . The charge threshold is defined by the distance between baseline voltage of OUT\_A and the point where  $I_{M8} = I_{DB}$ . When OUT\_A has the higher voltage level than the threshold point  $I_{M8} > I_{DB}$ , OUT\_D receives a discriminated active low output.

All front-end transistors are operated in weak inversion [80]. That's why current flow change is proportional to  $\exp(\Delta V_{gs})$ , where  $V_{gs}$  is the voltage between gate and source of the transistor. The nominal assigned for the current bias parameter is IBAIS = 20 nA and ITHR = 0.5 nA [83].

The  $C_{source}$  and the  $C_{curfeed}$  are combined in one capacitance  $C_s$  in order to have a compact layout of front-end circuit. Transistor M6 in diode connection: drain is connected to the OUT\_A node and source and gate are connected to the curfeed node, helps to achieve a clipping mechanism to limit the pulse duration for very large input signals. Typically M6 is reverse biased but it becomes forward bias when the OUT\_A signal is high enough and then it compresses the pulse duration by providing additional discharge current. When the input charges larger than 1.4 times the charge threshold both for OUT\_A and OUT\_D, this clipping effect is perceptible [83].

#### 3.4.3.1 Charge Threshold

The charge threshold is determined by the collected charge amount at the sensing node in order to make a hit at the front-end output. Analog front-end circuit shapes a pulse that is fed to a discrimination stage. Voltage excursion at the sensing node increases with a smaller pixel-input capacitance for a given collected charge and the conversion gain of charge-to-voltage eventually makes a larger pulse height within the frontend. The discrimination stage

does voltage comparison; therefore, smaller pixel-input capacitance decreases the charge threshold. Combination of ITHR and VCASN determines threshold where ITHR control the pulse shape (i.e. relative height and width) and baseline voltage of the analog front-end OUT\_A node defined by VCASN. This baseline voltage at OUT\_A is connected to the gate of transistor M8 (cf. figure-18b) and when it exceeds a critical voltage for which the current through M8 surpasses  $I_{DB}$ , the OUT\_D of the pixel becomes low (active). With increasing ITHR, pulse height and width reduce, whereas when VCASN increases, baseline voltage also increases and comes closer to the critical voltage for driving the output node. Consequently, rising ITHR increases the charge threshold whereas charge threshold is reduced by rising VCASN.

### 3.4.3.2 Front-End Biasing

Both current and the voltage on-chip bias Digital-to-Analog Converters (DACs) feature an 8-bit resolution [80] and placed in chip periphery. Their reference voltage (1.8V) [76] is supplied by a dedicated pad positioned at the edge of the sensor externally. The DAC values are obtained from device simulation that gives the front-end circuit a first working point. Only the reverse substrate bias<sup>6</sup> ( $V_{BB}$ ) is applied using an external power supply. Nominal DAC values seen by the pixel are given in Table-7 in chapter-5.

### 3.4.4 Digital Front-End Section

Digital front end of a pixel sensor is illustrated in figure-19. The digital part consists of three registers [76]:

- **A state register:** Hit information is kept by state register which is a set-reset latch. Simultaneous assertion of front-end discriminated output PIX\_OUT\_B and STROBE\_B sets the state register. When a hit is detected by the sensor, PIX\_OUT\_B is driven low and if it coincides with STROBE\_B the hit information is stored in the state register. Afterward, it can either be reset by a PIX\_RESET pulse generated by Priority Encoder during the readout.
- **A mask register:** Once the mask register is set, the registered hit in state register doesn't propagate to the AERD (MASK\_EN is set high, the STATE output is forced to 0). This confines malfunctioning and excessive noise interruption in the readout.

---

<sup>6</sup> Reverse-Substrate Bias Voltage- The reverse-substrate bias voltage ( $V_{BB}$ ) influences extending the depletion region between collection diode and substrate.

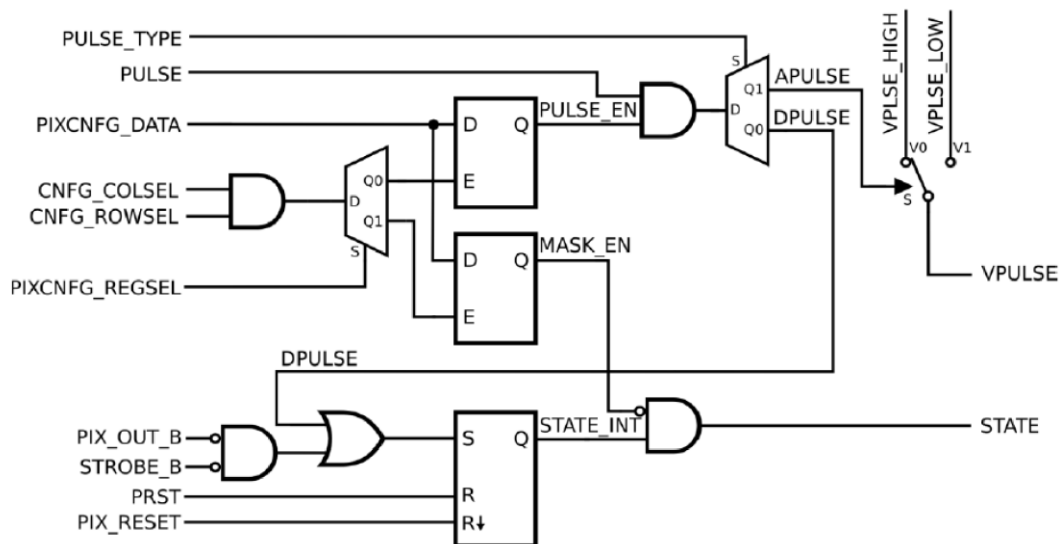


**Figure 19: Functional diagram of the pixel digital front-end [82], [84].**

- **A pulse register:** Front-end response and state register's functionality is tested by accessing each pixel that is enabled by pulse register. When the pulse register is set to one, the test pulse (digital or analog) is propagated to the pixel. For two different pulse modes the test can be performed by applying global PULSE signal to the respective chip pad to steer the test pulse. PULSE\_EN=1 enable the testing functionality, disable otherwise. Digital pulsing is provided by PULSE\_TYPE=0 and PULSE\_TYPE=1 activate analog pulsing [82].
  - **Digital Pulsing-** The digital testing allows to stimulate the state register and forced to logic high the hit latch (STATE\_INT) bypassing STROBE\_B signal and analog front-end [82]. STATE signal must go high with the assertion of the PULSE signal provided the pixel is not masked and state register is functioning properly [76].
  - **Analog Pulsing-** Analog pulsing indicates injection of a test charge  $Q_{inj}$  into the sensing node through a capacitor. Difference between VPULSE\_HIGH and VPULSE\_LOW defines the amplitude of the applied pulse. Both edges of charge signal provoke the charge injection of opposite polarities where the leading edge corresponds to the discharge of the collection diode similar to a traversing particle [76], [82].

### 3.4.5 Priority Encoders and Pixel Indexing

Address-Encoder and Reset-Decoder (AERD) is an asynchronous full-custom circuit for a fast readout of the pixel matrix. An AERD circuit was shown in figure-15(b). AERD consists of a fast OR logic, priority address encoder and a one-hit reset decoder [79], [85]. The 1024 STATE signals of the pixels of the related double column are provided as an input of AERD and then AERD generates addresses of the hit pixels as follows: generated VALID signal by the fast OR logic is set high if at least one pixel is hit in double column [76]. The subsequent

SELECT signal asserted by the digital periphery propagates through the reset decoder in the various layers to the hit pixel with the lowest address (highest priority). The SELECT signal's forward propagation brings pixel address to the digital periphery. Once the address is read by the digital periphery, the pixel is reset. Setting VALID signal to low all hit pixels connected to the AERD is read for several iterative processes. Unless there's a hit present, there is no activity in the circuitry.

An array of 512 Priority Encoder blocks readout the matrix of pixels [82]. The pixels are arranged in double columns and Priority Encoders occupies the regions at the middle of each double column. Priority Encoder defines the indexing of the pixels in the readout data. Figure-20 illustrates the indexing of pixel in double column.

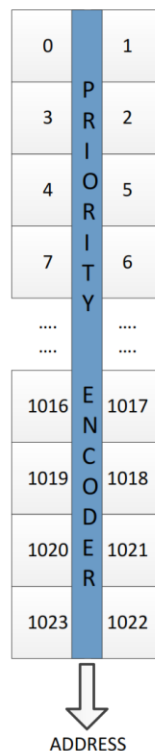


Figure 20: Indexing of pixels inside a double column provided by the Priority Encoders [84].

## 3.5 Radiation Damage in MAPS

ALPIDE was mainly developed to be applied in upgraded seven layers of ALICE Inner Tracking System (ITS) at CERN. These Silicon Pixel Detectors are expected to work in harsh radiation environment [82]. The high radiation creates an unprecedented challenge in required prolonged operability for MAPS. So recently developed MAPS is assumed to have much high radiation tolerance and above that tolerance limit, it is most likely to show some radiation damage. Radiation effects on silicon detector are discussed in following paragraphs.

### 3.5.1 Radiation Damage Effects

Radiation-induced effects can be subdivided into two types of defect [76]:

- Bulk Defect- Displacement of lattice atoms due to non-ionizing energy loss;
- Surface Defects- This is the ionizing radiation effect on the dielectrics and the silicon-dielectric interface;

In the ALPIDE, following radiation-induced effects are expected to occur:

#### 3.5.1.1 Bulk Damage

Bulk damage is originated from the inelastic displacement of nuclei in the sensor. That creates imperfections in the crystal structure and helps producing additional energy levels within the silicon bandgap which eventually changes the properties of the material. This type of radiation damage is caused by hadrons. Bulk radiation damage is scaled using the Non-Ionizing Energy Loss (NIEL)<sup>7</sup> in order to compare the damage induced by different particle types with different energies [86]. Radiation-induced bulk defects mainly cause a change in the macroscopic property of the silicon detector [87], [88] as follows:

- **Increase of leakage current-** The lattice defects caused by radiation, increase the volume-related leakage current across a p-n junction that is strictly proportional to the equivalent fluence  $\Phi_{eq}$  (fluence of any particle related to fluence of 1 MeV neutron).

$$\Delta I = \alpha \Phi_{eq} V \quad (3.4)$$

Where,  $V$ = Depleted volume.

$\alpha$ = Current related damage rate (For silicon at 20°C  $\alpha$  is about  $3.9 \times 10^{-17}$  A/cm) which is independent of the type and initial resistivity and the material [78]

---

<sup>7</sup> NIEL: Neutrons of 1 MeV are commonly used as reference particles. The damage due to a fluence of another particle has therefore to be related to the equivalent fluence of 1 MeV neutrons causing the same damage. The energy dependent conversion factor is called NIEL.

The increasing leakage current increases shot noise, as well as a larger power dissipation of the sensor [76]

- **Effective doping concentration-** When there is any involvement of impurity atoms, which are used as doping, in the radiation-induced crystal defects they might become electrically inactive, hence losing their function as donors or acceptors. At the same time, during the radiation-induced generation of defects new acceptor or donor states may be created. The difference of all donor and acceptor-like states is quantified by a term that is effective doping concentration  $N_{eff}$ . The fluence dependency of  $N_{eff}$  is following,

$$N_{eff}(\Phi_{eq}) = N_{A,0} \cdot e^{-c_A \Phi_{eq}} - N_{D,0} \cdot e^{-c_D \Phi_{eq}} + b_A \Phi_{eq} - b_D \Phi_{eq} \quad (3.5)$$

Where,  $N_{A,0}$  = Acceptor concentration before irradiation

$N_{D,0}$  = Donor concentration before irradiation

$c_A, c_D, b_A, b_D$  constants to be determined experimentally [76].

- **Decrease of the charge collection efficiency-** Crystal defects set up a state called trapping centers for charge carriers. While moving through the sensor material, the carrier's probability of encountering a trap is proportional to the elapsed time. Trapping is therefore described by a parameter that is carrier lifetime  $\tau$ . At a given carrier lifetime  $\tau$ , an amount of charge generated in a single point,  $Q_0$ , will decay so that after a time  $t$  the remaining charge is given by,

$$Q(t) = Q_0 e^{-t/\tau} \quad (3.6)$$

So, if the carrier lifetime decreases to the order of the charge collection time, part of the signal charge is lost that manifest degradation of the Charge Collection Efficiency (CCE) of the sensor.

### 3.5.1.2 Surface Defects

This type of effect is mainly caused by Ionizing radiation and can be scaled with Total Ionizing Dose (TID)<sup>8</sup>. Surface defect affects the surface oxide layers, and the lateral isolation oxides of MOSFET transistors, by trapping the positive charge carrier in the insulation layers (usually SiO<sub>2</sub>). For CMOS pixel sensors, this causes a shift of threshold voltages, an increase of noise and parasitic leakage currents [76].

---

<sup>8</sup> TID- Accumulating the radiation dose over time.

## CHAPTER-4 METHODS MATERIALS

For pCT, recently proposed sensor is ALPIDE. For ALICE ITS upgrade ALPIDE development has gone through several optimizations. This thesis is mostly confined to analyzing data from final ALPIDE chip for different radioactive sources as well as proton beam. The detector configuration and circuit details are discussed widely in chapter 3. This chapter will focus on the ALPIDE chip setup (single chip with DAQ board) for reading particles, the software used to perform standard tests of the chip, details of standard tests, data analyzing and other relevant methods.

### 4.1 ALPIDE Test Board

For the test of the ALPIDE chip, a DAQ and a carrier board are used. Figure-21 shows how these two boards are coupled. The Carrier board, electrically connected to ALPIDE chip with wire bonds, holds the chip. Concerning the DAQ board, this board is powered by a voltage of 5V and to connect it to a PC it has a USB connection. The biggest black chip in the middle called FPGA chip that allows programming the DAQ board. There is a connector for the carrier board. The DAQ board also contains the potentiometers to vary the analog and digital power (The VDDA and VDDD, respectively) and nominal value is 1.8V.

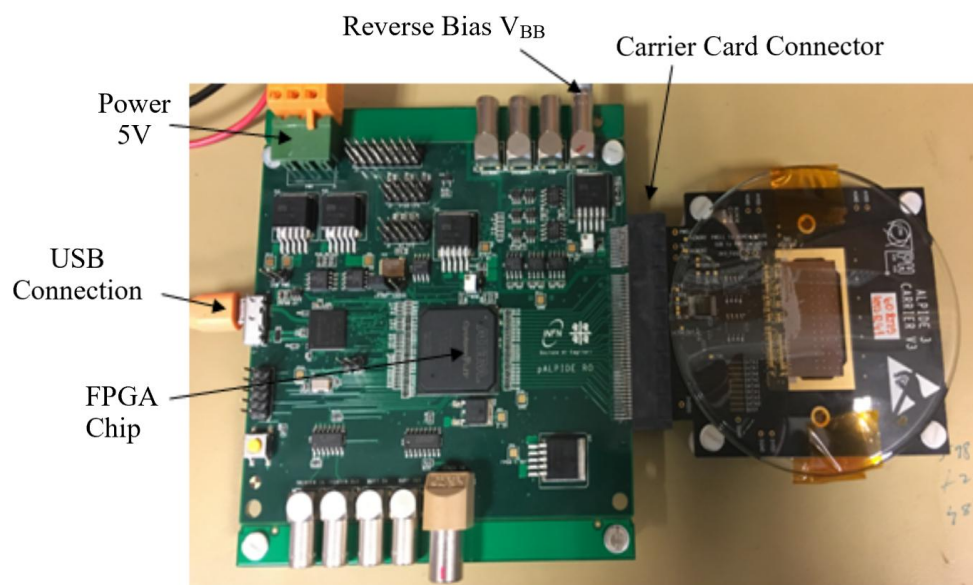


**Figure 21: Carrier (black) and DAQ (green) board connected together. There's a glass protector on the top of the Chip.**

## 4.2 Chip Tests

ALPIDE software that is installed in the PC connected by a USB with the DAQ board provides standalone test programs. A dedicated command line is executed for each test. Test parameters' (number of mask stages, number of injections etc.) values are set in the configuration file name config.cfg. This config file is saved in the same subdirectory of the ALPIDE test programs. Each test generates output in a data file. Some of its main test functions are described in the following paragraphs.

### FIFO Test

This is a quick test to verify communication with the chips' control interfaces. It writes three different bit patterns (0x0000, 0xffff and 0x5555) into each cell of the end-of-column FIFOs [89] and reads them back. During the test it also checks the correctness or the read-back values. The test is executed by asserting the parameter FIFO to the program:

**`./test_fifo`**

### On-Chip DAC Scan (DAQ Board Only)

On-chip DACs output can be connected to monitoring pins of the ALPIDE chip and this is measured by ADCs on the DAQ board. Characteristics of all on-chip DACs are measured by DAC scan. The output is obtained for each DAC by looping over the values from 0 to 255. For each DAC the output values are written into a file. These files contain two columns of numbers: the first one has a number from 0 to 255 and the second one has the correspondent voltages or currents. The test is executed by running:

**`./test_dacscan`**

### Digital Scan

Digital scan injects a digital pulse in a number of pixels and readout the hits. For this test number of injected pixels and number of injections is configurable in the config file by three parameters **NINJ**, **PIXPERREGION**, **NMASKSTAGES**. NINJ decides the number of injections in a pixel. The parameter PIXPERREGION gives the number of simultaneously injected pixels per region. After injecting to one-pixel group the scan moves to the next one. The Number of such steps or mask stage is given by NMASKSTAGES. To analyze all pixel of the entire chip the mask has to be staged 16384. Digital scan test starts with command:

**`./test_digital`**

The output data is written into a file DigitalScan.dat containing three columns

### Doublecol Address NHits

Doublecol ranges from 0 to 511 and Address from 0 to 1023. This digital data can be visualized by a macro analysis Hitmap.C. The macro is invoked in a form **.x Hitmap.C (<filename>)**

### **Threshold Scan**

This test provides analog injection or in other words a programmable charge injection into the preamplifier, looping over the charge. 50 injections are performed for each charge point. Command line for this test is,

**./test\_threshold**

The output raw data that are the number of hits for each charge point is presented in a file, name ThresholdScan.dat and organized in 4 column,

### **Doublecol Address Charge NHits**

Charge range for the threshold scan can be configured in the config file. Default setting ranges from 0 to 49 DAC units (1 DAC=10 e<sup>-</sup>) [71] . Now a macro **FitThresholds.C** can be used to fit the s-curves for the scanned pixels. The compiled form of this micro is **.x FitThresholds.C+ (<filename>)**. An output file **FitValues... .dat** is generated with all the fitted values in a format,

### **doublecol address thresh noise chisq**

A macro **ThresholdMap.C** is performed to visualize the data in form of a threshold map.

### **Noise Occupancy**

The selectable number of random triggers is given in this test and number of hits is returned. The dedicated command for this test is,

**./test\_noiseocc**

It has an identical output file format like a digital scan. A histogram of the noise occupancy as a function of the number of masked pixels can be produced by macro **NoiseOccupancyRawToHisto.C**

### **Source Scan**

A source scan is performed with the single event information by the command,

**./test\_noiseocc\_singevent**

This instruction is used when a random trigger is generated internally by the chip itself. The default strobe duration for internal strobe is 2  $\mu$ s and a delay between pulse and strobe is 500 ns. But External triggering can also be used to provide flexibility of adjusting the strobe duration and delay the command is,

**./test\_noiseocc\_ext\_singevent**

The hitmap macro is then used to show the hit data.

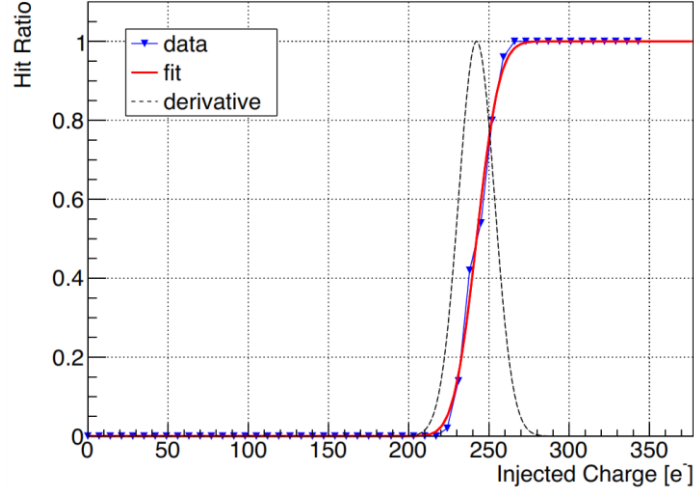


Figure 22: S-curve measurement: hit ratio  $r(Q_{inj})$  as a function of  $Q_{inj}$  [76].

### 4.3 Threshold and Noise Measurement

The charge threshold and Noise of the front-end circuit of the ALPIDE prototypes are usually determined by so-called S-Curve scan. The noise of MAPS generates from various spots in the circuitry [90], [91]. One of these noises is shot noise<sup>9</sup>. The S-Curve scan is done with keeping fixed front-end settings. Front-end node is injected by a charge  $q_{inj}$  by giving a negative voltage step on the injection capacitor  $C_{inj}$  (cf. figure-17). The  $q_{inj}$  can be varied by varying the voltage step. If a range of test charge ( $q_{inj}$ ) is injected for  $N$  times in a pixel and number of times the pixel has registered a hit is measured then the response function  $r(Q_{inj})$  is given by following equation [76] and illustrated in figure-22.

$$r(Q_{inj}) = \frac{N_{hit}(Q_{inj})}{N} \quad (4.1)$$

The hit-detection probability  $p$  of the pulsed pixel is measured for each injected charge. Assuming the noise has a gaussian distribution then the response function of the pixel is given as following [80]

$$p_{Hit}(q_{inj}) = \frac{1}{2} \left( 1 + \text{Erf} \left[ \frac{q_{inj} - \mu}{\sqrt{2} \cdot \sigma} \right] \right) \quad (4.2)$$

Where,

$q_{inj}$  = Injected charge

$\mu$  = Charge threshold

$s$  = Noise.

<sup>9</sup> Shot Noise- Noise generated from the discrete nature of electric charge carried by charge carrier.

The response function has a characteristic S-shape, therefore, the measurement is called S-Curve scan. Here  $\mu$  and  $s$  values are obtained from the pixel-by-pixel fit. Figure-23 shows the distribution of threshold and noise.

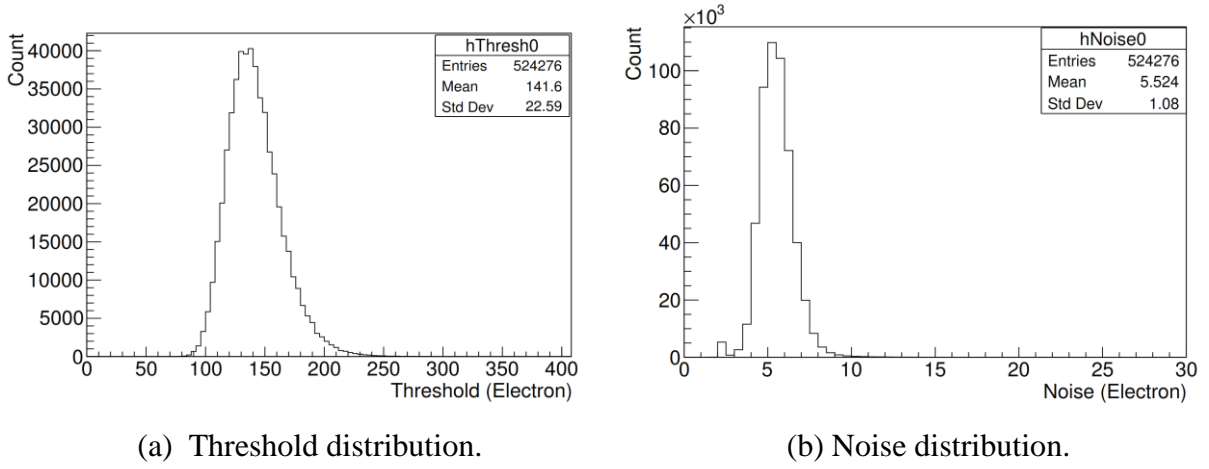


**Figure 23: Threshold and noise distributions.**

Threshold and Noise have an influence of  $V_{BB}$ ,  $V_{CASN}$ , and  $ITHR$ . Experimental data and plot will be presented in chapter-5.

#### 4.4 Fake Hit Rate (FHR)

The threshold and noise, both give gaussian distribution. However, for most of the chips, there are few pixels that do not exhibit a response function. These are the pixels that control the fake hit rate if not masked. The fake hit rate is the rate at which pixels show a hit when there are no ionizing particles. Due to its strong effect on the performance of tracking device fake hit rate is considered very important in pixel chip. The fake hit rate is estimated by reading out the chip without providing an external stimulus like a radioactive source, beam or external pulsing in a sequence of consecutive events. The  $R_{FH}$ , average fake hit rate is calculated as following [80]

$$R_{FH} = \frac{N_{Hits}}{N_{Pixels} \cdot N_{Events}} \quad (4.3)$$

Where,  $N_{Hits}$  = the number of hits detected

$N_{Pixels}$  = the number of pixels under study

$N_{Events}$  = number of recorded events

## 4.5 Sealed Radioactive Sources

Sealed radioactive source restrains radioactive substance in such a way that under normal circumstances these substances cannot escape. These radioactive sources are broadly used and generally preferred for their small size and mobility in industry, medicine, and research. This study includes the use of several sealed radioactive sources in the laboratory to check the detection performance of proposed ALPIDE pixel detector. The types of sources used for this thesis is discussed in the following paragraphs.

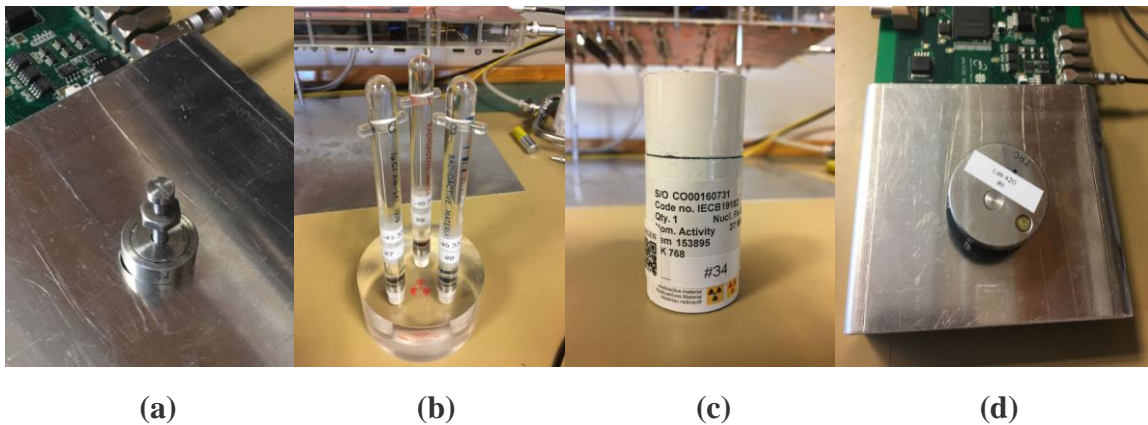


**Figure 24: Sealed Radioactive sources for laboratory experiment. (a)  $^{241}\text{Am}$  isotope as Alpha source (b)  $^{90}\text{Sr}$  isotope as Beta source (c)  $^{55}\text{Fe}$  isotope as Gamma source (d) Variable energy X-ray source.**

### Alpha source ( $^{241}\text{Am}$ )

Americium-241 ( $^{241}\text{Am}$ ) is one of the radioactive isotopes of Americium with half life 432.2 years [92]. This isotope has a specific activity of 3.43 Ci/g (curies per gram) or  $1.27 \times 10^{11}$  Bq/g (Becquerel per gram) [93]. The  $^{241}\text{Am}$  contains alpha energy of 5486 keV (85%), 5443 keV (13%) and 5388 keV (1%). Figure-24(a) shows the alpha source used in the laboratory.

### Beta Source ( $^{90}\text{Sr}$ )

Strontium-90 ( $^{90}\text{Sr}$ ) is a radioactive isotope of Strontium. It has a half-life of 28.2 years. This beta emitter with one decay mode decays into Yttrium-90 by emitting  $\beta^-$  with maximum energy 546 KeV [94]. The daughter  $^{90}\text{Y}$  has a half life of 64 hours and decays to stable Zirconium-90 by emitting negative beta with maximum energy 2.27 MeV. Specific Activity of  $^{90}\text{Sr}$  is  $1.41 \times 10^2$  Ci/gram or  $5.21 \times 10^{12}$  Bq/g. The beta source used in the laboratory is shown in figure-24(b).

### Mono-Energetic Radiation Source ( $^{55}\text{Fe}$ )

Iron-55 ( $^{55}\text{Fe}$ ) is a radioactive isotope of Iron. Half-life of  $^{55}\text{Fe}$  is 2.737 years. Generally, photons emitted from  $^{55}\text{Fe}$  are in two emission modes with energies of 5.9 keV and 6.5 keV, with a probability of 24.40 % and 2.85 %, respectively [95]. These photons have attenuation

lengths of 29  $\mu\text{m}$  and 37  $\mu\text{m}$  in silicon [96].  $^{55}\text{Fe}$  is also called a source of mono-energetic radiation of 6 keV photon energy with a probability of about 28% [97]. Specific Activity of ( $^{55}\text{Fe}$ ) is  $2.43 \times 10^3$  Ci/gram or  $8.98 \times 10^{13}$  Bq/g. Figure-24(c) is the used one for this thesis.

### Variable Energy X-ray Source

Figure 24(d) shows a Variable energy X-ray source on the top of the ALPIDE chip. There is a hole just beneath the round shaped source and through this hole, particles hit the chip. This X-ray source contains 6 different isotopes that are responsible for variable energy. The list of isotopes and their corresponding energy is given in Table-5.

**Table 5: Isotope parameters for variable X-ray source [98]**

Isotope	Cu	Rb	Mo	Ag	Ba	Tb
Energy	8.04	13.37	17.44	22.10	32.06	44.23
KeV	8.91	14.97	19.63	24.99	36.55	50.65

## 4.6 Proton Beam

Proton is a microscopic particle known as a building block of an atom. A proton beam is generated by focusing protons into a narrow ray and shooting them at extremely high speed. Proton beam is generated by a particle accelerator. This accelerator runs with the principle of coulombs law (same charge repels and opposite charge attracts) and uses electromagnets to accelerate and focus the protons. The electromagnet changes its charge from positive to negative to pull and push the proton. This is how protons are speeded up and a proton beam is generated from a bunch of protons.

Most commonly used accelerator for treatment is cyclotron that is a circular accelerator. Particle's path is made circular by the magnetic field to spin the proton beam around and around until they reach a certain speed to shot out to their target.

### 4.6.1 ALPIDE Proton Beam Test

To ensure detection performance for proton, ALPIDE was irradiated by proton beam at Oslo Cyclotron Laboratory (OCL) from 30<sup>th</sup> October to 3<sup>rd</sup> November 2017. The energy of proton beam for ALPIDE testing was approximately 16 MeV. Beam diameter was measured close to 1 cm by a photographic plate shown in figure-25. The beam was monitored from the control room shown in figure-27(a) and monitoring window shows all relevant parameter like current, presence of other ionizing radiation (Gamma, Neutron) and their measured dose, illustrated in figure-27(b). The goals of this test were,

- To examine the chip's performance at different distance and angle along with identifying the Bragg Peak and spreading of the applied proton beam. Also to observe cluster sizes and their distribution for proton.

- Defining the position (distance & angle) where chip shows pileup or it becomes saturated and the position where single proton is read per event.

#### 4.6.2 Test Setup

The test setup includes,

- Accurate positioning of ALPIDE chip on the beam trail confirming all necessary power supply and other connection.
- Providing proper shielding to avoid radiation induced effect.
- Collecting data and monitoring beam and chip performance from the control room.

To hold the ALPIDE chip with required shielding, 2 mm Aluminium plate was used, shown in figure-26(b). The holders were placed on the top of an aluminium base to place it on the beam trail given in figure-26(a). Figure-26(c) shows the final placement of ALPIDE chip along the beam trail. A laser beam was used to measure the distance and angle of the ALPIDE chip from the proton beam vent. For remote controlling, patch panel was used.

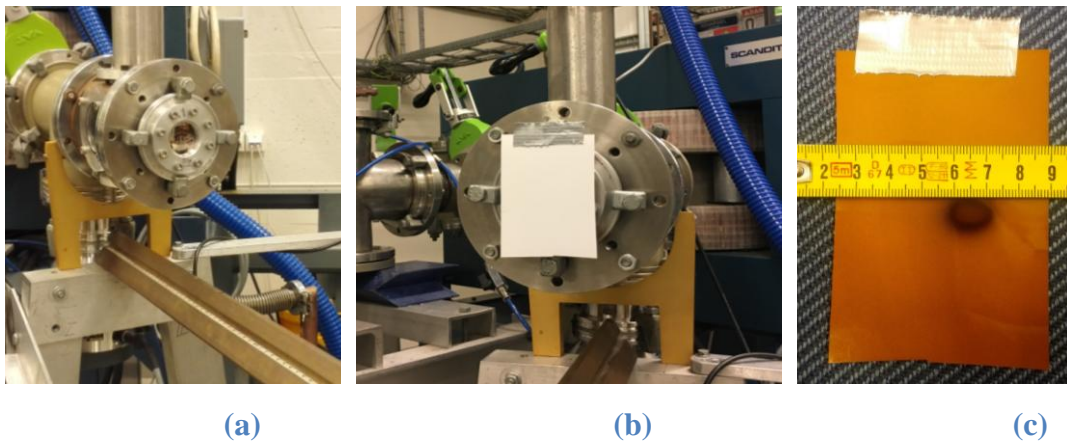


**Figure 25: (a) Beam vent (b) Photographic plate placed on the beam vent to measure the diameter (c) measured diameter around 1 cm.**

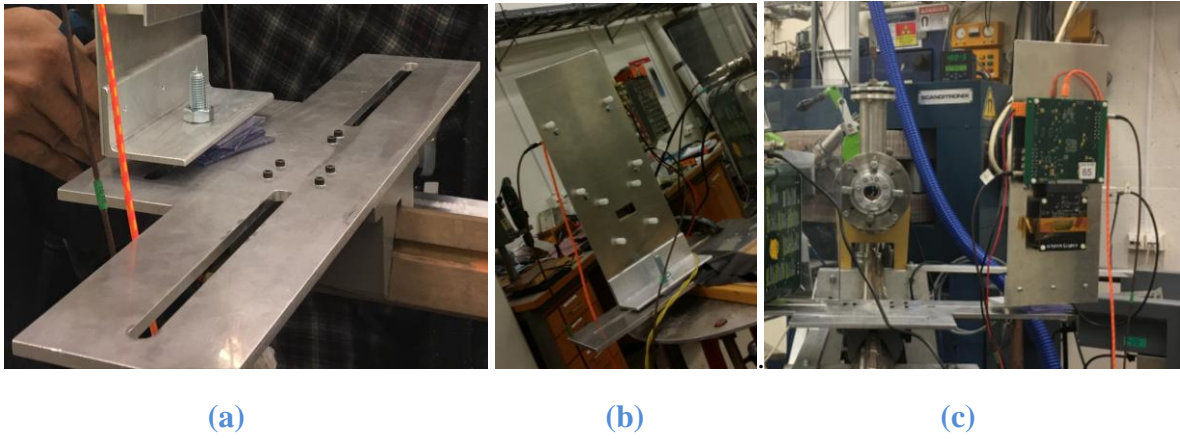


**Figure 26: (a) Aluminum base to place the holder on the beam trail (b) Aluminium holder and shielding for ALPIDE chip (c) Chip placement.**



**Figure 27: (a) Beam monitoring window (b) Measuring Gamma and Neutron incidence simultaneously.**

#### 4.7 Helium Beam Test

The Helium (He) micro beam experiment was conducted at Australia Nuclear Science and Technology Organisation (ANSTO) in Australia in January 2018. The experimental goal was to observe how the cluster size changes with the departed energy to the epitaxial layer of the ALPIDE, and at the same time to see if the cluster size varies with the position of where the charge departed. The tests were performed with a Helium-4 ion beam with a fixed energy of 10 MeV that unfortunately could not be changed. The ion rate was 2 KHz and 10 KHz. The test setup was almost similar to proton beam test. The micro beam had high resolution with beam diameter less than 1  $\mu\text{m}$ . This will be discussed and explained in more details in a future master thesis by Simon Huiberts, “Characterization of the ALPIDE chip with Helium and Proton beam”.

#### 4.8 ALPIDE Data Collection

ALPIDE chip undergoes the standard test for source scan and it generates a data file with certain information like pixel address, event number, number of hits and so forth. These data

files are obtained and stored by dedicated software (cf. section-4.2) installed in a computer. Figure-28 shows how the data file looks. Each file consists of 5 columns (First two columns define column and row number of pixel, the third column gives event no which is the number of strobes provided, fourth one is a clock and the fifth one gives number of hits/number of the activated pixel). A trigger signal mainly performs for the data request. Three available trigger modes are following [76],

- **Internal Trigger:** FPGA on the DAQ unit implements this trigger.
- **External Trigger:** the trigger is provided from an external device to the DAQ unit upon the incidence of a signal.
- **Software Trigger:** Trigger issued by software, and can acquire any data at the maximum achievable rate.

The strobe duration given internally by the chip itself is  $2\ \mu\text{s}$  with 500 ns delay. For proton as well as other source scan, the strobe duration was adjusted externally at  $9.7\ \mu\text{s}$  with 250 ns delay. In order to limit registering the same pixel multiple time, strobe duration was externally increased by a signal generator.

Row	Column	Event No	Clock	Hits/Activated Pixel
25	3	51	5	2081451935 78
26	3	52	5	2081451935 78
27	5	51	5	2081451935 78
28	4	51	5	2081451935 78
29	4	52	5	2081451935 78
30	5	52	5	2081451935 78
31	41	270	5	2081451935 78
32	42	270	5	2081451935 78
33	42	271	5	2081451935 78
34	129	128	5	2081451935 78
35	129	129	5	2081451935 78
36	128	129	5	2081451935 78
37	128	130	5	2081451935 78
38	129	130	5	2081451935 78
39	129	131	5	2081451935 78
40	130	128	5	2081451935 78
41	130	129	5	2081451935 78
42	130	130	5	2081451935 78
43	130	131	5	2081451935 78
44	515	501	5	2081451935 78

**Figure 28: Generated data file with 5 columns after source scan.**

### 4.8.1 Cluster

The file generated by the source scan contains hit information of pixels. The number of active pixels in each frame depends on the source type and its corresponding energy. The term cluster means a pixel group showing signal above a certain threshold and it causes by sharing the same charge created by ionizing radiation among several pixels [76]. Every source leads to a cluster distributions and a characteristic signal depending on their process of energy loss

and conversion; for instance, X-rays are absorbed by photoelectric conversion in a point like region. The MIPS particle creates e-h pairs uniformly along their track and can cross a thin sensor. Charged particle like proton, alpha, and atomic ion losses energy while traversing a material because they transfer energy when interacting with an electron of atoms in the material. For pCT it's important to know how the cluster size changes when proton or any other particle strikes the detector.

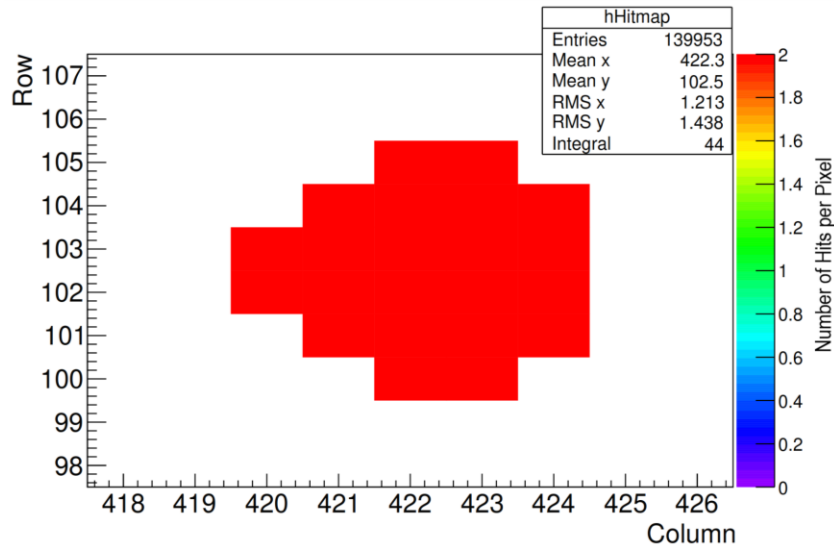


**Figure 29: Cluster for alpha particle. Notice that the cluster occurs in two frames.**

#### 4.8.2 Analysing Cluster Size and Cluster Distribution

Figure-29 shows how cluster looks for alpha particle. All activated pixels are plotted in a hitmap where X-axis represents the number of column (0-1023) of sensor chip, Y-axis is number of row (0-511) and the coloured scale at right side shows the number of hits per pixel. This hitmap is generated by a root macro for the initial visualization of all registered pixels. Cluster sizes can also be determined from the data file because it copies the address of nearby pixel. So counting the number of pixels those are at close vicinity and forming a group gives the cluster size. The distribution pattern of this cluster sizes can also be obtained if the number of clusters is calculated for each event. This is further discussed in Chapter-5. This study mainly covers cluster analysis by root and C++ programming. Analyzing code is attached in section-A.3.

## CHAPTER-5 RESULTS AND DISCUSSION

This chapter will present all the experimental result and relate it to theoretical standard and previous research findings. ALPIDE silicon pixel detector has been chosen as the main element for high-granularity DTC in pCT. Since different prototype of ALPIDE has been studied over several years at CERN for ALICE experiments, there are several published methods and procedure to characterize the chip and analyze data. The methods, explained in chapter-4, are used firstly, to test the chips and see if the result is as expected or not also to verify the influence of related parameters. Secondly, to analyze the response of pixel detectors for different radiation like Alpha, Beta, X-ray as well as particle like proton. Thirdly, the radiation effects on a chip and measuring the level of effect in terms of threshold and noise. Finally, there are findings related to cluster size and cluster distribution to see how they vary with radiation type and energy.

### 5.1 Test objectives

In the following paragraphs, results from three different ALPIDE chips are presented and commented. Here follows a general description of ALPIDE tests with their objectives:

- DAC Scan with nominal configuration for three different chips. The aim of this test is to see the linear fit for each DAC and conversion from DAC to volt as well as DAC to electrons.
- Full chip Threshold and Noise Scan for three different chip at different Reverse Bias Voltage ( $V_{BB}$ ), generally given 0V, -3V and -6V, to see the change in threshold and noise level in terms of  $V_{BB}$ .
- Threshold and Noise scan with varying ITHR (10-70 DAC) and VCASN (50, 57, 63, and 69 DAC) the test objective is to see change in threshold and noise level in terms of ITHR and VCASN.
- Noise Occupancy or Fake hit rate test for three different  $V_{BB}$  (0V, -3V and -6V) in order to see the variation of fake hit rate with changing  $V_{BB}$ .
- Noise Occupancy or Fake hit rate test with varying ITHR (10-70 DAC) and VCASN (50 and 57 DAC) in order to see how they are related.
- Threshold and Noise scan for three chips where, one is not irradiated and two are irradiated by heavy charged particle Helium (He) with variation in average dose per chip. The test objective is to see the radiation effect by monitoring the drop and rise of threshold and noise respectively.
- Source scanning for three different particles  $\alpha$ ,  $\beta$ ,  $\gamma$  and analyze their cluster sizes.
- Source scanning for X-ray with six different energies (8.04 KeV - 50.65 KeV) and observe how cluster size changes with energy deposition.
- Proton beam test and see the cluster shape and size.

## 5.2 ALPIDE Chips

Three ALPIDE chips are listed with their number in Table-6. For chip characterization, these three chips were used. None of these chips were used in proton beam test. Chip-1 and 2 were irradiated by different ionizing particle most importantly Helium-4 ion of 10 MeV.

**Table 6: List of ALPIDE Chips**

Chip 1	Chip 2	Chip 3
608519 W13R41	608520 W07R05	608519W13R07

## 5.3 ALPIDE Tests

### 5.3.1 Test 1- DAC Scan

DAC Scan is performed to understand the characteristics of all on-chip DACs (Explained in section-4.2). The test result for chip-1 is shown in figure-30. Two other chips give the same plots. The linear fit is calculated for the linear part from the number of hits vs. injected charge plot (cf. figure-22). From the slope of the line, the conversion from DAC to volt and DAC to electron can be done.

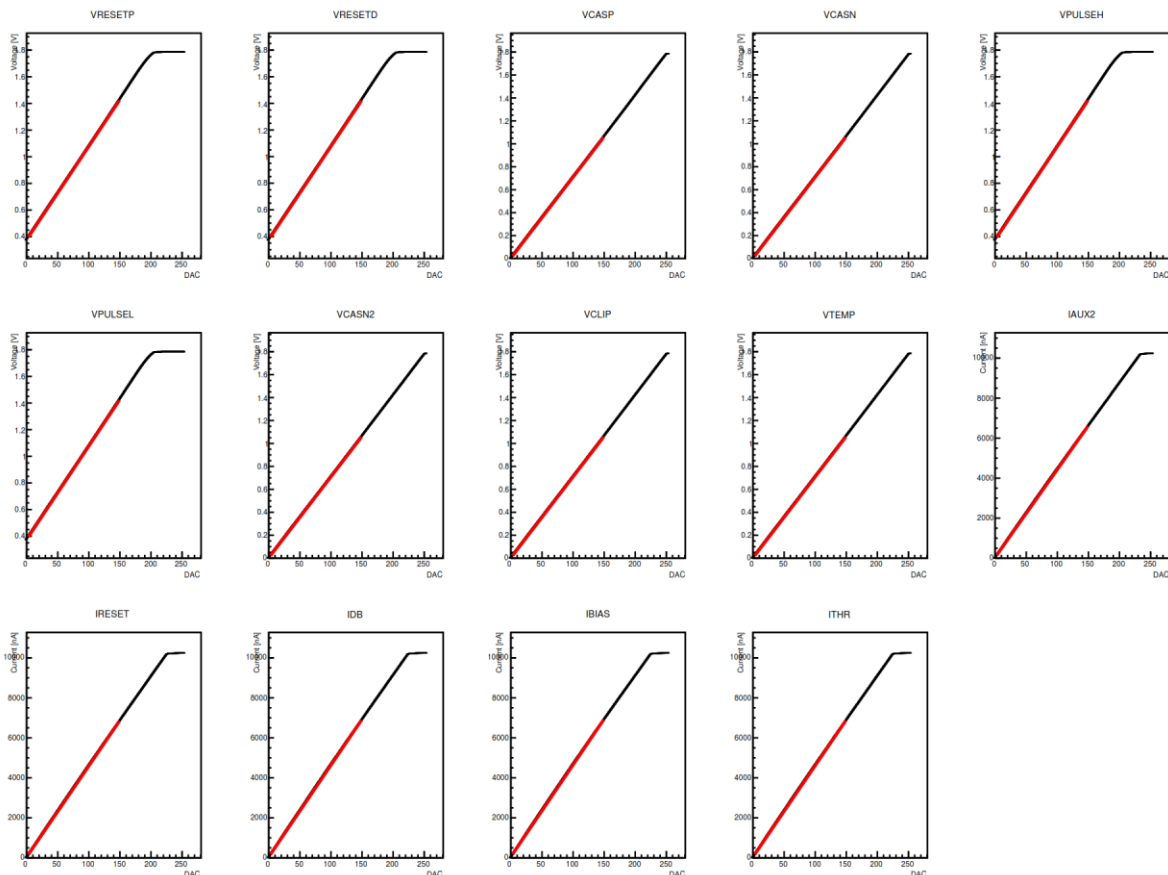


**Figure 30: Plot for all individual DAC.**

Similar graphs are generated for all the DACs from the individual DACScan file. The slope of these lines can be changed only with changing supply voltage. For our experiment, the supply voltage was fixed,  $V_{DDD}=V_{DDA}=1.8\text{ V}$ . The set DAC values for some of the main DACs are shown in Table-7 also some DAC values needs to be adjusted with changing reverse bias voltage, given in Table-8.

**Table 7: Nominal values for the DACs at 1.8V, expressed in DAC units**

VCASN	VCASN2	VCLIP	VRESETD	ITHR	IDB	VCASP	IBIAS	VPULSEH
50	62	0	147	50	29	86	64	170

**Table 8: Adjusted DAC value for different reverse bias voltage ( $V_{BB}$ )**

	0V $V_{BB}$	-3V $V_{BB}$	-6V $V_{BB}$
VCASN	50	105	135
VCASN2	62	117	147
VCLIP	0	60	100
VRESETD	147	147	170

### 5.3.2 Test 2- Threshold and Noise Scan with varying $V_{BB}$

Threshold scan is performed on three chips to obtain threshold and noise level of pixels. To ensure all pixels' participation, the full chip was scanned adjusting relevant parameters. Applied  $V_{BB}$  was 0V, -3V and -6V (required set up for this voltages are given in table-8). Required configurations for this test are given below:

- $PIXPERREGION=4$ .  $PIXPERREGION$  is the number of enabled pixels per region or in one mask stage.
- $NMASKSTAGES=4096$  (for full chip scan when  $PIXPERREGION=4$ ). In the config file,  $NMASK$  is a parameter that determines the number of mask stage for a chip in a particular test.  $NMASKSTAGES$  means how many times a group of a pixel will be read in one of the 32 regions of ALPIDE chip.
- Charge looping from 0 to 49 DACs.

Once the test is complete, a file names *ThresholdScan.dat* is created by the software described in paragraph 4.2. After that, a ROOT macro read and analyzes the file to determine the threshold and noise for each sector. The number of hits for all pixels is available in the output file and this is analyzed as a function of injected charge. The macro makes the S-curve (cf. figure-22) with the charge on the x-axis and the number of hits on the y-axis and gaussian error function that includes two parameters, threshold, and noise.

# Chip 1

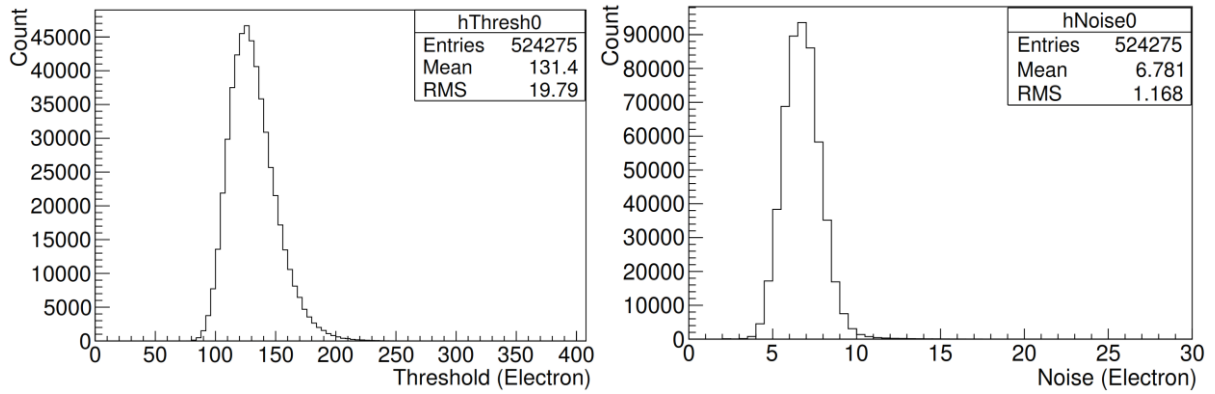


Figure 31: Threshold and Noise at 0V  $V_{BB}$ .

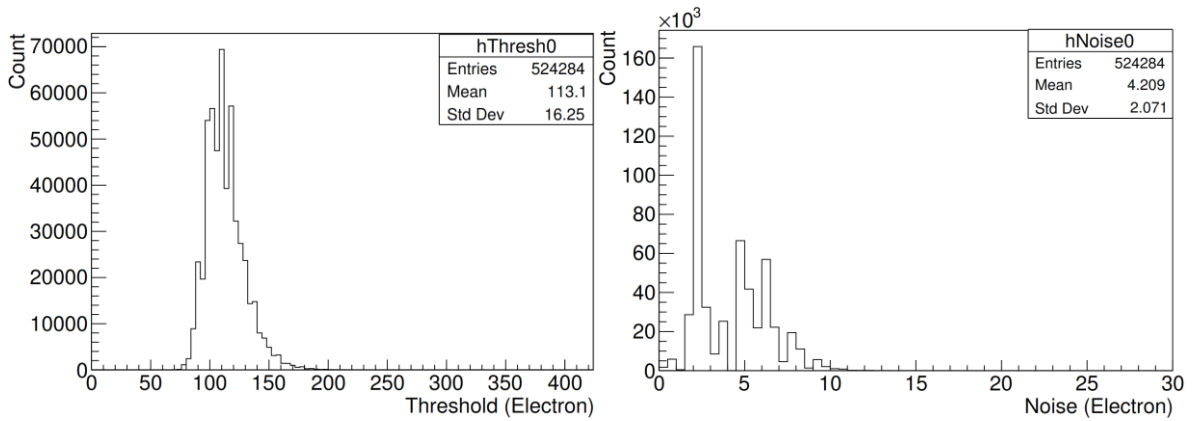


Figure 32 : Threshold and Noise at -3V  $V_{BB}$ .

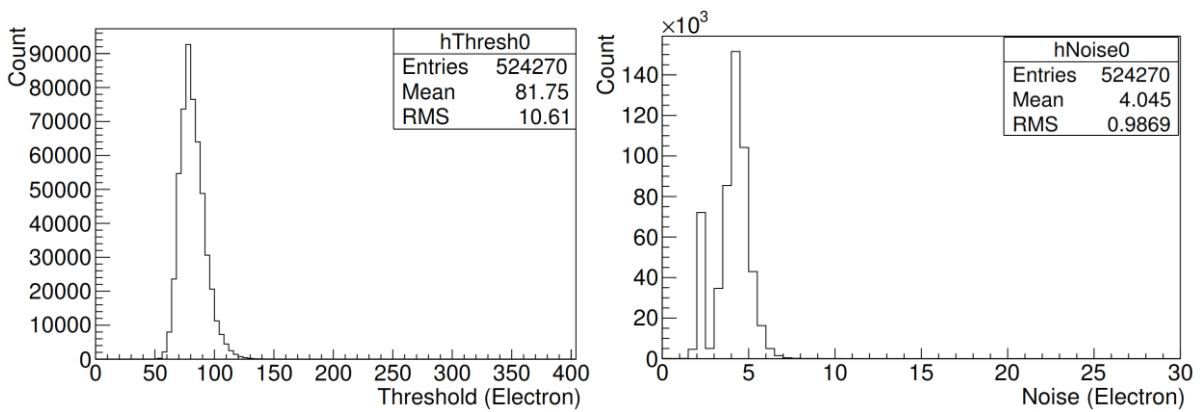


Figure 33: Threshold and Noise at -6V  $V_{BB}$ .

## Chip 2

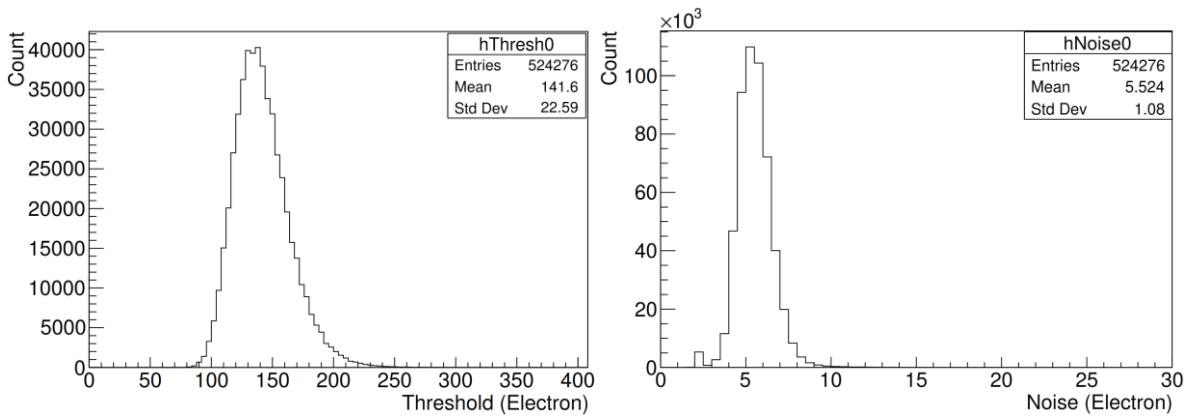


Figure 34: Threshold and Noise at 0V  $V_{BB}$ .

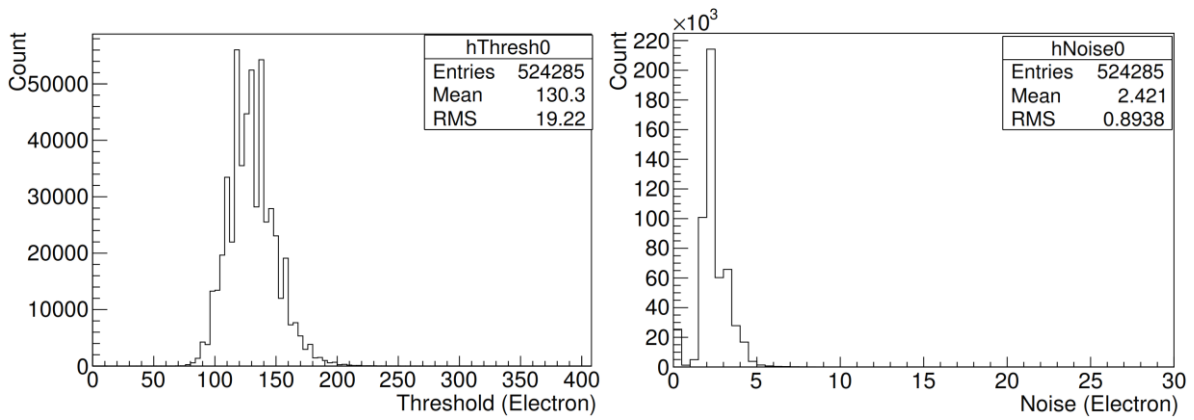


Figure 35: Threshold and Noise at -3V  $V_{BB}$ .

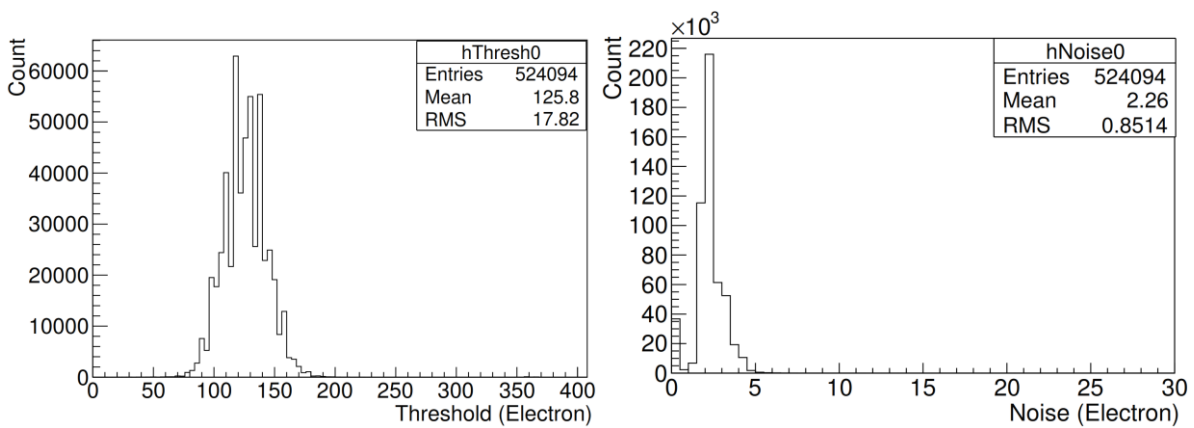


Figure 36: Threshold and Noise at -6V  $V_{BB}$ .

### Chip 3

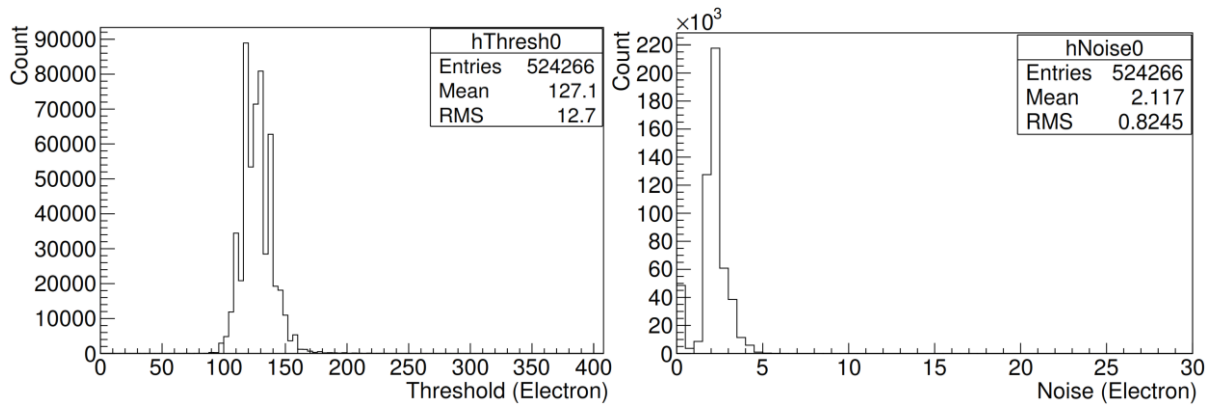


Figure 37: Threshold and Noise at 0V  $V_{BB}$ .

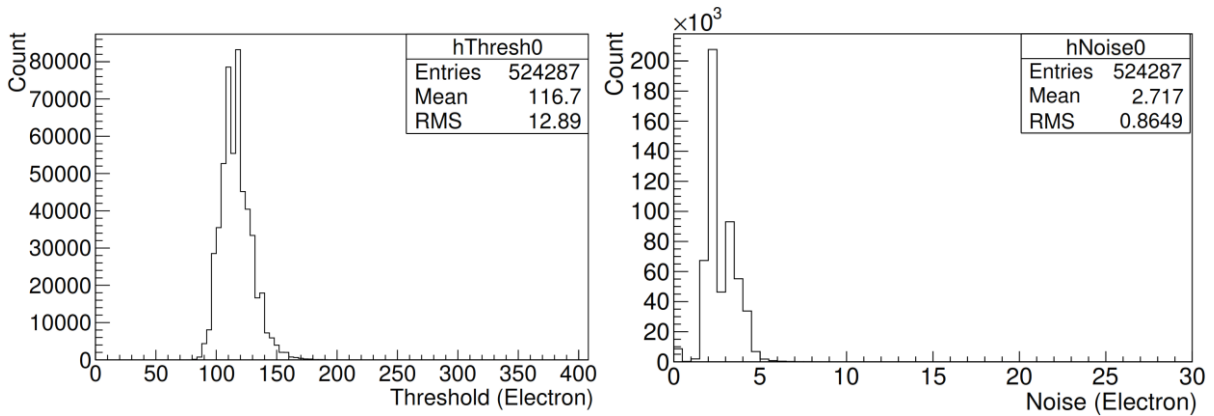


Figure 38: Threshold and Noise at -3V  $V_{BB}$ .

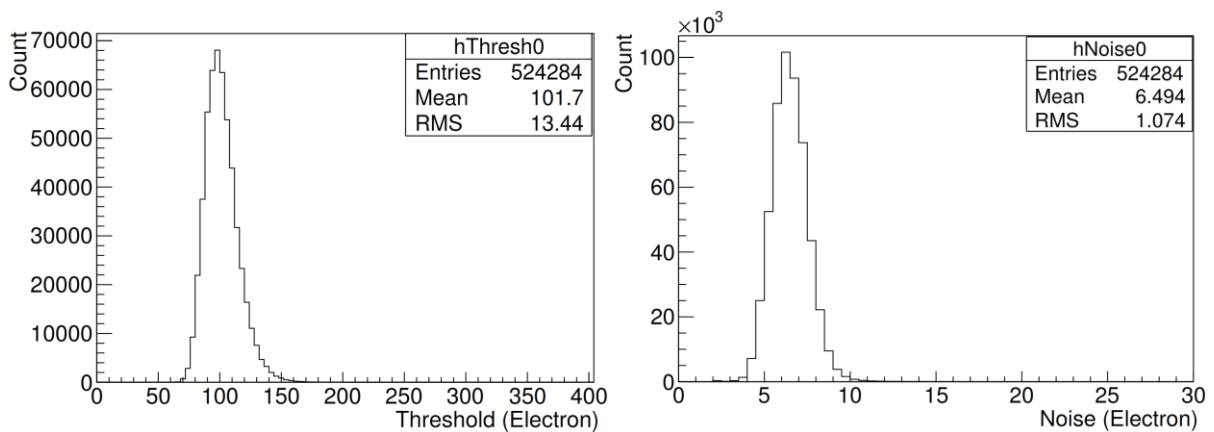


Figure 39: Threshold and Noise at -6V  $V_{BB}$ .

### 5.3.2.1 Influence of $V_{BB}$

For steering the chip performance the key parameter is the charge threshold. The threshold value of the chip is influenced by  $V_{BB}$ . From the figure- 31 to 39, the change of mean threshold and noise for three chips at different reverse bias voltage is seen. Threshold and noise both decrease with increasing  $V_{BB}$  for first two chips. For chip-3, with increasing  $V_{BB}$  the threshold reduces but noise increases.

The reason why threshold value reduces with increasing  $V_{BB}$  is explained in one of the CERN studies on ALPIDE [76] and it says, increasing  $V_{BB}$  reduces pixel-input capacitance and that leads to reduced charge threshold. So basically, for threshold test, a range of test charge is injected via the pulsing capacitance and when this capacitance drops with rising  $V_{BB}$ , conversion gain of charge-to-voltage increases and produce larger pulse height. This high gain also increases the baseline voltage of the threshold defining point OUT\_A, given in equation-3.3 (cf. figure-18b). As a consequence of increasing baseline voltage, the threshold which is the distance between baselines to critical point reduces. This is how change in  $V_{BB}$  affects the threshold level. The Noise should behave in opposite way. Higher the threshold, lower the noise, that is obtained only for chip-3. The reason why chip-1 and 2 give noise value in opposite pattern is hard to define, only few assumptions can be made such as:

- Radiation effect- Chip-1 and 2 are irradiated chips. They were highly irradiated during Helium micro beam test whereas, chip-3 is completely nonirradiated. Radiation can cause a behavioral change in chip.
- Temperature effect- The tests were not temperature stable. So change in temperature can also influence the test output.

### 5.3.3 Test 3- Threshold and Noise Scan with varying ITHR and VCASN

Once again threshold scan was performed with varying ITHR and VCASN. These are two parameters that have great influence on threshold level (explained in section-3.4.3.1). For this test only chip-1 with following configurations was used:

- NMASKSTAGES= 100.
- VCASN has been chosen to be 50, 57, 63 and 69 (DAC value) and corresponding parameter VCASN2 is adjusted to 62, 69, 75 and 81 (DAC value). This entire configuration is done in config file saved in software subdirectory.
- ITHR ranges from 10-70 DAC in steps of ten for each VCASN.
- $V_{BB}=0V$ .

#### 5.3.3.1 Influence of ITHR and VCASN

The threshold and noise can be regulated by changing ITHR and VCASN (explained in section-3.4.3.1); these are some frontend bias parameters. It is observed from the figure-40

that threshold increases almost linearly with increasing ITHR, and decreases with increasing VCASN so different combination of ITHR and VCASN can help to attain the same threshold.

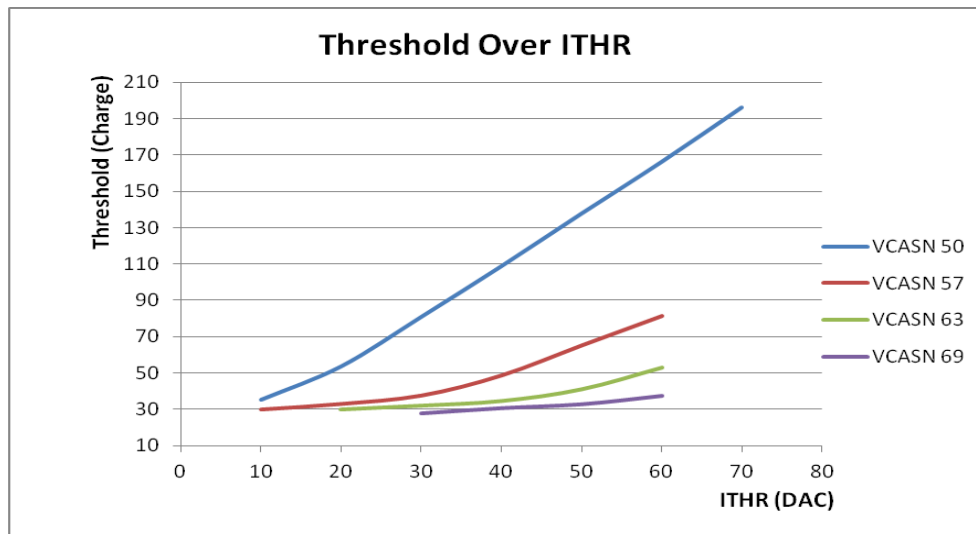


**Figure 40: Mean threshold as a function of ITHR and VCASN.**

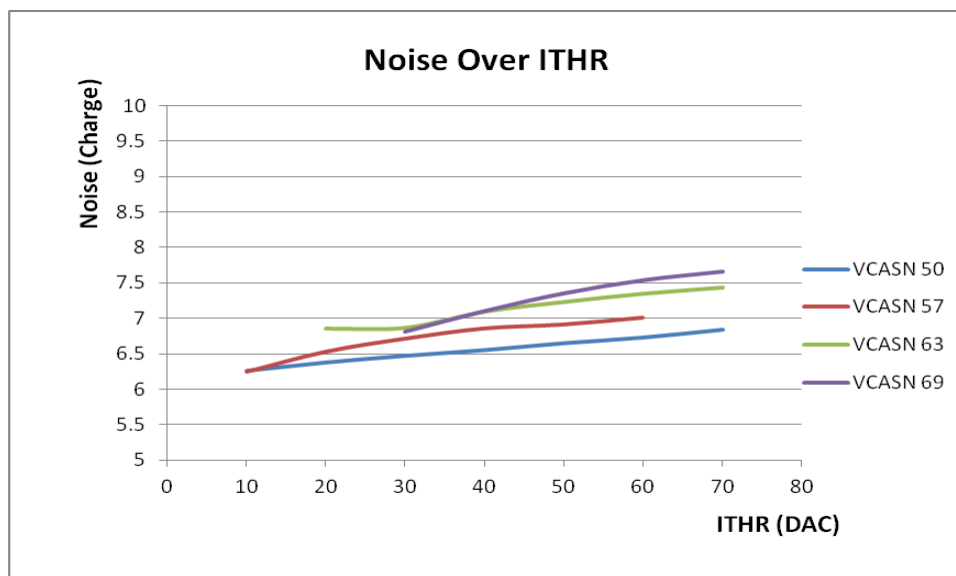


**Figure 41: Mean noise as a function of ITHR and VCASN.**

The mean noise is also increasing with increasing ITHR and VCASN illustrated in figure-41. A similar test was performed with first ALPIDE prototype known as pALPIDE-1 [76] and it was observed that the mean noise reduces with increasing ITHR whereas it was almost uninfluenced by VCASN. In our case, we used the final version of ALPIDE chip and also experiments were not temperature stable so there might have some temperature effect as we know high temperature causes more current burn and increased noise.

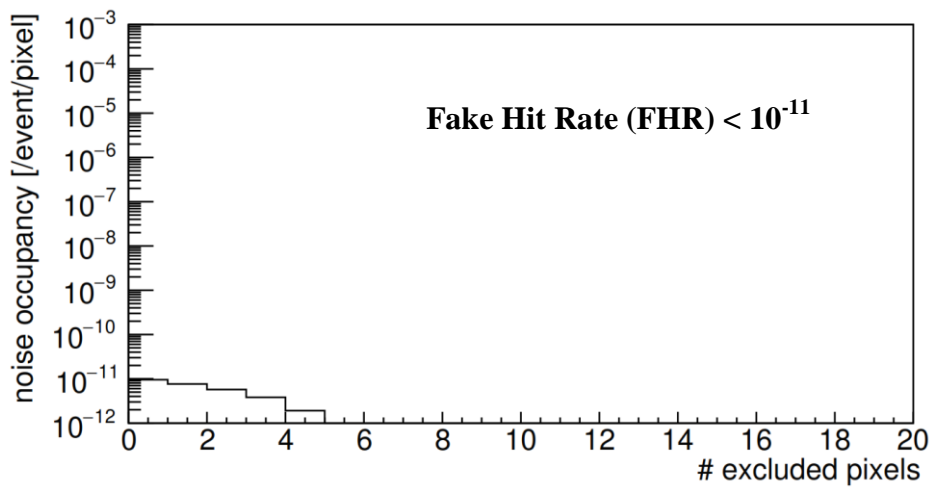
### 5.3.4 Test 4- Noise Occupancy or Fake Hit Rate Test for Three Different $V_{BB}$

This test is performed on three chips with the following setup:

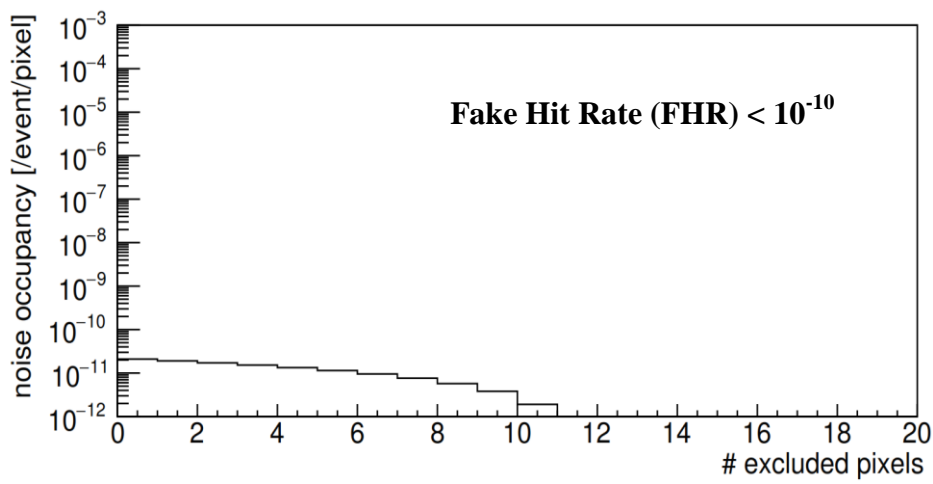
- Number of internally given event/ STROBE was 10,000.
- STROBE duration was 2  $\mu$ s.
- Value of certain parameters was adjusted for different  $V_{BB}$  (cf. Table-8).
- ITHR=50.

At the end of the test, a file *NoiseOccupancy.dat* is generated with a line format as described in section-4.2. Paragraph 4.4 explains how the fake hit rate is calculated from the total number of hits. Now how this fake rate is influenced by  $V_{BB}$  is discussed in the following paragraph.

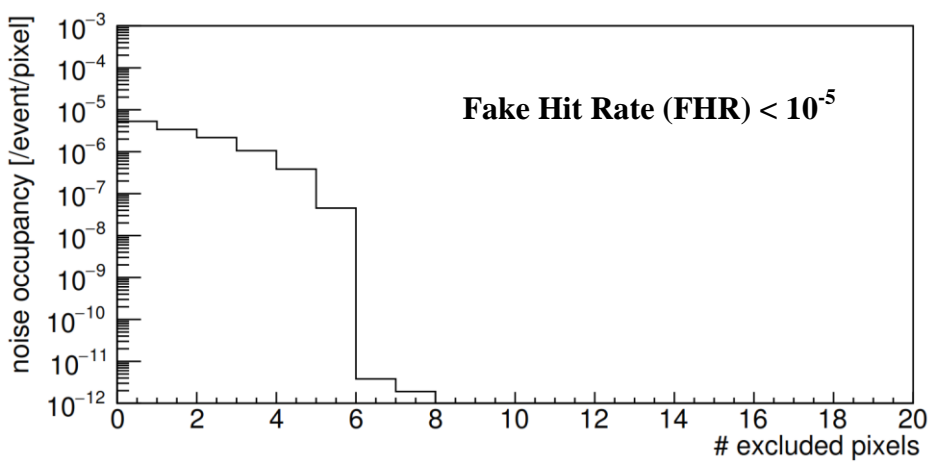
# Chip 1



(a)



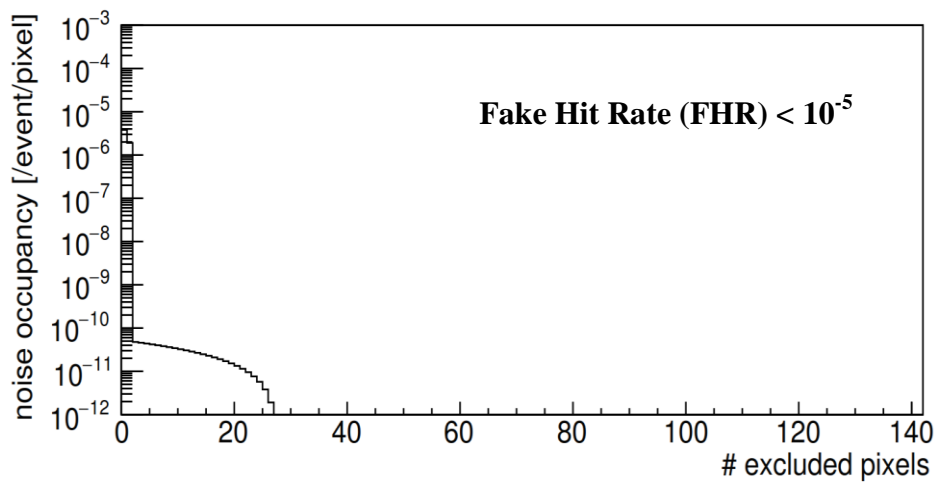
(b)



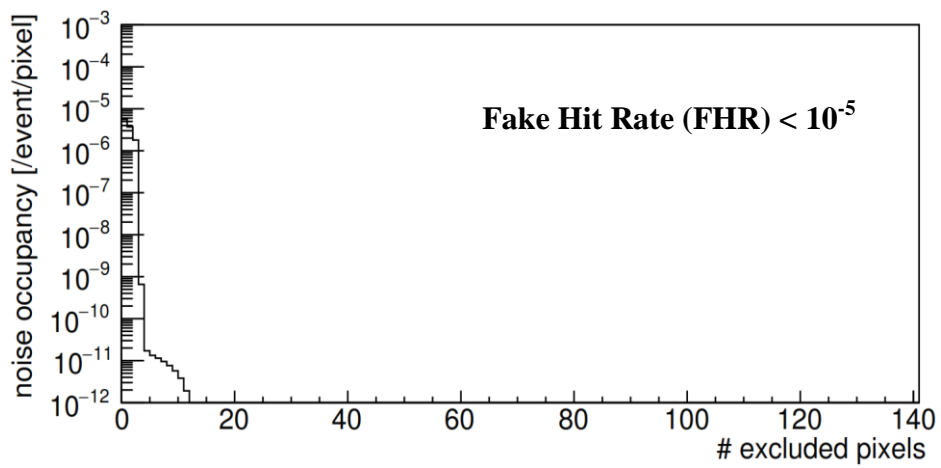
(c)

**Figure 42: Fake Hit Rate at  $V_{BB}$  (a) 0V (b) -3V (c) -6V.**

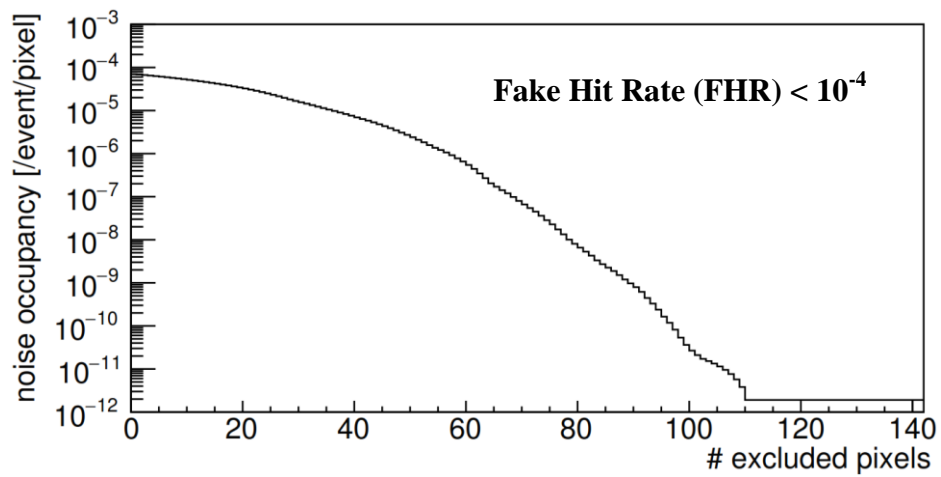
## Chip 2



(a)



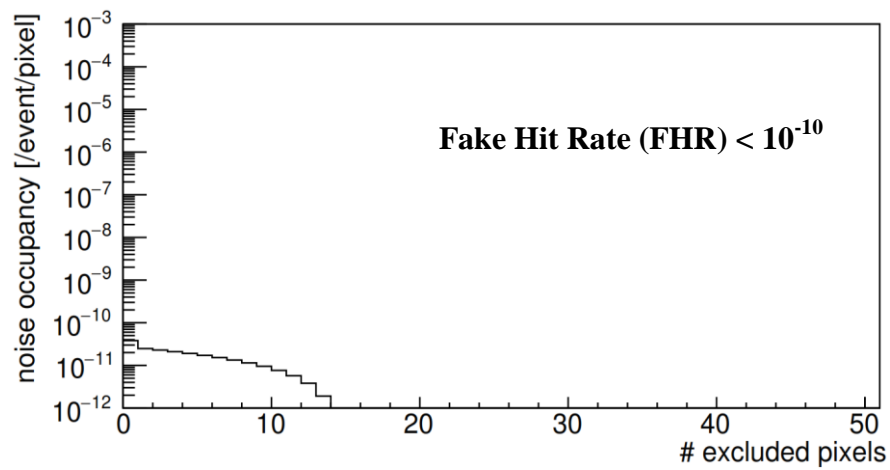
(b)



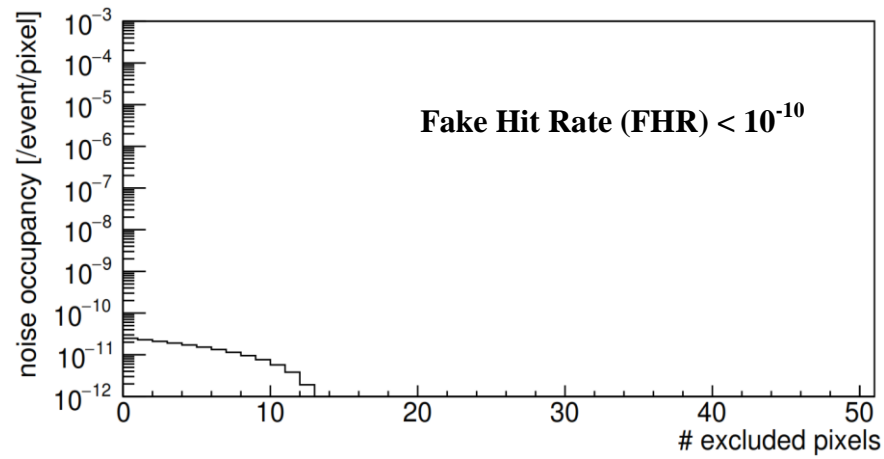
(c)

Figure 43: Fake Hit Rate at  $V_{BB}$  (a) 0V (b) -3V (c) -6V.

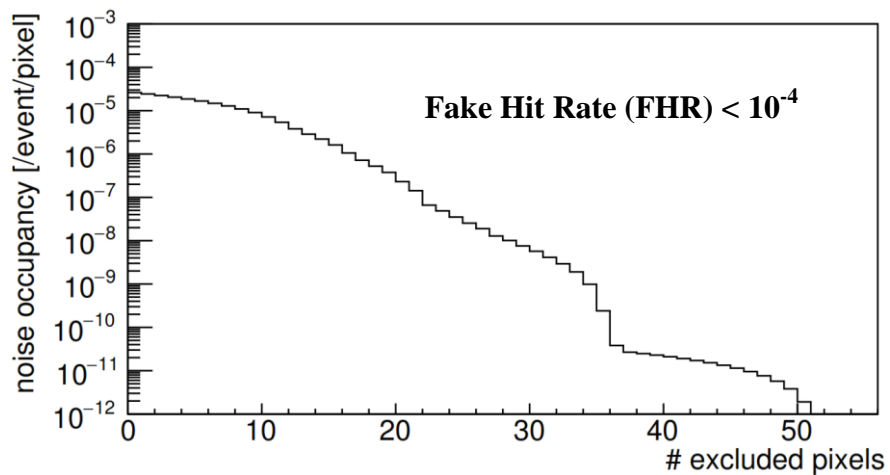
### Chip 3



(a)



(b)



(c)

Figure 44: Fake Hit Rate at  $V_{BB}$  (a) 0V (b) -3V (c) -6V.

#### 5.3.4.1 Influence of $V_{BB}$

The Fake hit rate is most likely to be influenced by the threshold. If the threshold is low, the probability of fake hit rate increases, so all the parameters those are responsible for changing threshold level have some effect on fake hit rate.  $V_{BB}$  is considered one of those parameters. When  $V_{BB}$  increases, threshold drops therefore fake hit rate increases and this effect is illustrated in figure-42, 43 and 44. Fake hit rate increases with increasing  $V_{BB}$ , for instance, in figure-43,

At  $V_{BB}=0V$ ,  $FHR=10^{-10}$  /event/pixel  $\rightarrow$  masked pixels nearly 2

At  $V_{BB}=-3V$ ,  $FHR=10^{-10}$  /event/pixel  $\rightarrow$  masked pixels nearly 4

At  $V_{BB}=-6V$ ,  $FHR=10^{-10}$  /event/pixel  $\rightarrow$  masked pixels nearly 100

A similar test was also performed with pALPIDE-1 [76] and it was observed that FHR reduces with increased  $V_{BB}$  that is opposite to our finding. But that test was done with 500 ns STROBE duration and our experiment was at 2  $\mu$ s so there is 4 times higher probability of noise gain and increasing FHR. Again temperature was not controlled throughout the experiment so temperature effect shouldn't be underestimated.

Radiation has an effect on the fake hit rate. Chip-2 is highly irradiated with Helium ion and as a consequence, the fake hit rate for this chip is reasonably higher even at  $V_{BB} = 0V$  and  $-3V$  in comparison to other chips. But still, it does not cross the maximum limit of fake hit rate assigned for ALPIDE chip (cf. Table-4) that is  $< 10^{-5}$  per readout frame and pixel.

#### 5.3.5 Test 5- Noise Occupancy or Fake Hit Rate test with varying ITHR and VCASN

This test was done only on Chip-1 and required setup is following:

- Number of internally given event/ STROBE was 10,000.
- STROBE duration was 2  $\mu$ s.
- ITHR ranged from 10-70 DAC in steps of ten for each VCASN 50 and 57 DAC.
- $V_{BB}$  was fixed at 0V.

Results are illustrated in the following figures and paragraphs where the influence of certain parameters is also discussed in detail.

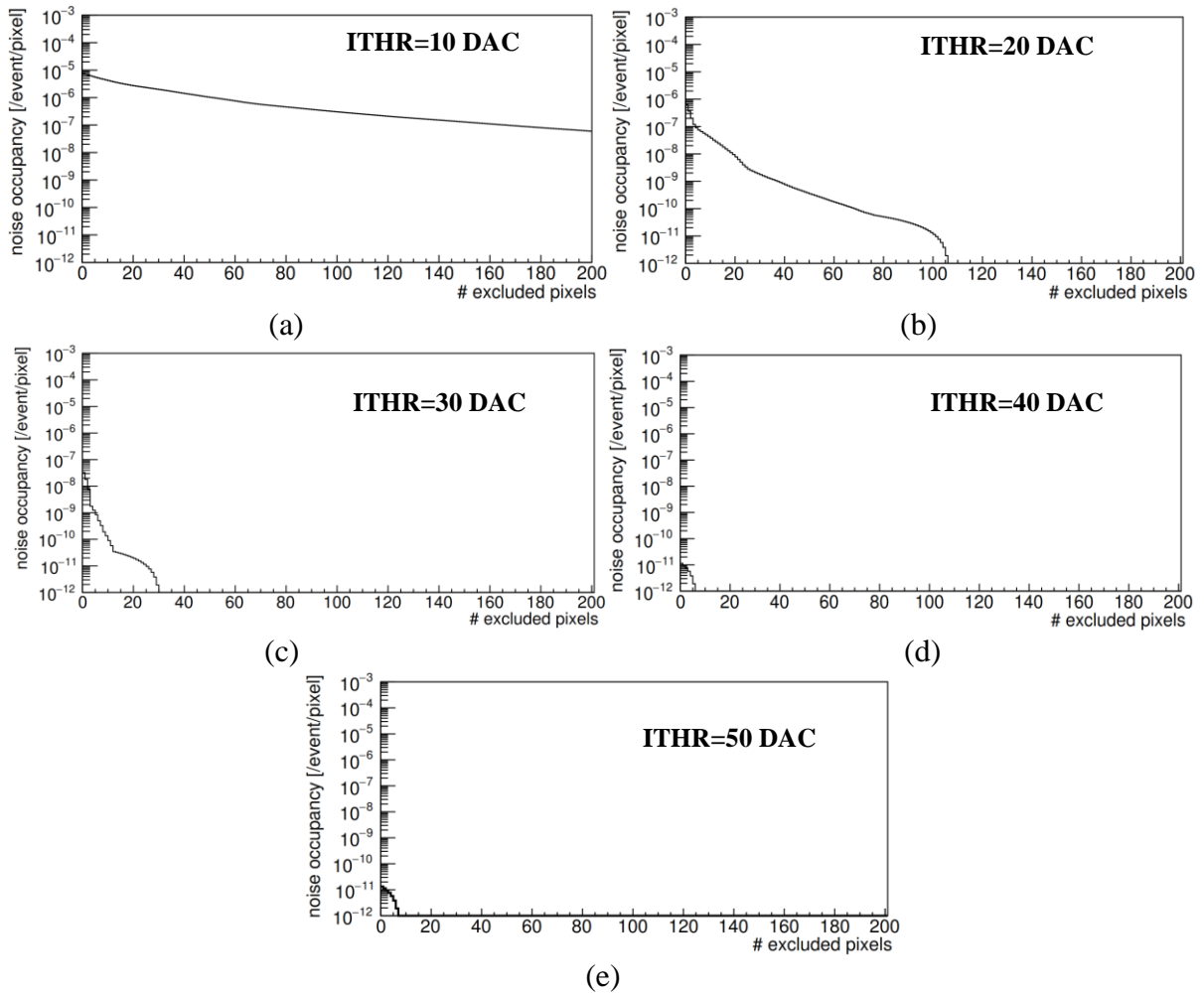


**Figure 45: Fake hit rate of chip-1, as a function of number of masked pixels with nominal  $V_{CASN}=50$  DAC and  $V_{BB}=0V$  (a) ITHR=10 DAC (b) ITHR=20 DAC (c) ITHR=30 DAC (d) ITHR=40 DAC (e) ITHR=50 DAC.**

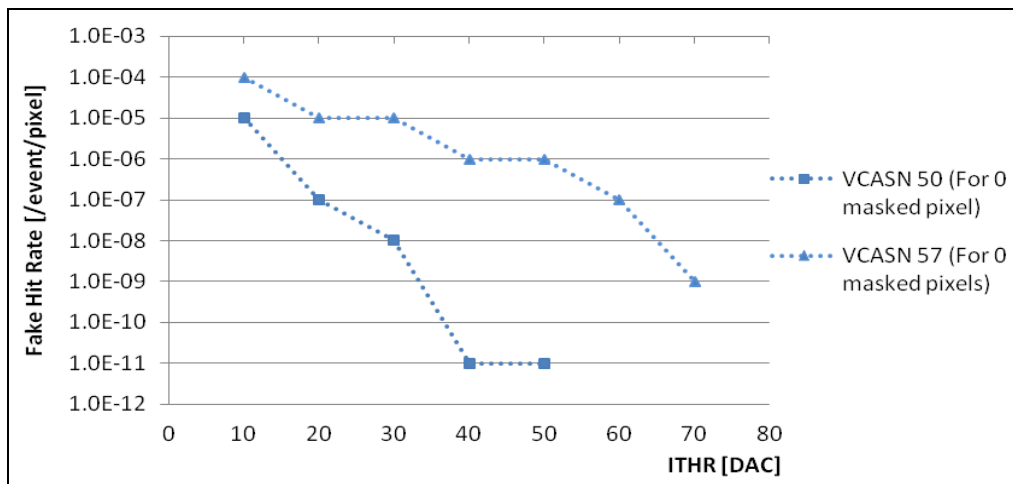


**Figure 46: Fake hit rate as a function of ITHR and VCASN for  $V_{BB}=0V$  and zero pixels masked and its projection along the axis of VCASN.**

### 5.3.5.1 Influence of ITHR and VCASN

Figure-45 shows results for the fake hit rate as the function of masked pixels or excluded pixels for different ITHR. Figure includes only ITHR up to 50 DAC because above that fake hit rate becomes zero. To see the change in fake hit rate over ITHR, for this test VCASN was chosen 50 DAC. It is observed that Fake-hit-rate reduces with increasing ITHR.

Also in figure-46, fake-hit-rate is shown as a function of ITHR and VCASN. It is clearly visible that fake hit rate drops with increasing ITHR when the number of masked pixels is fixed at 0. Now if we correlate this relation with the threshold value as function of ITHR and VCASN (cf. figure-40), where increasing ITHR makes the threshold value increased so, we can conclude that higher the threshold value lower the fake hit rate because pixel has to cross the threshold level in order to be recorded as hit.

On the other hand, when VCASN increases, threshold value drops that leads to higher fake hit rate, illustrated in figure-46. VCASN defines the baseline voltage at the OUT\_A node, which is connected to the gate of the transistor that controls the output stage (cf. M8 in figure-18b). For any chosen value of VCASN if OUT\_A node exceeds that certain critical voltage, outputs of all pixels will be constantly activated (i.e. a fake hit rate equal to one) and leading to a non-functioning of the chip. The nominal value of VCASN is chosen 50 DAC for ALPIDE tests.

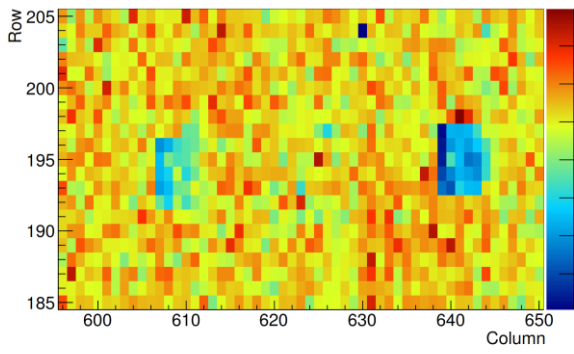
### 5.3.5.2 Influence of Masked Pixels

It is known that fake hit rate is dominated by a few, so-called hot pixels rather than the gaussian noise, therefore, masking those hot pixels might be an easy way to get rid of high fake-hit-rate and this is assumed from the figure-49 that shows lower fake-hit-rate when excluded pixels are more.

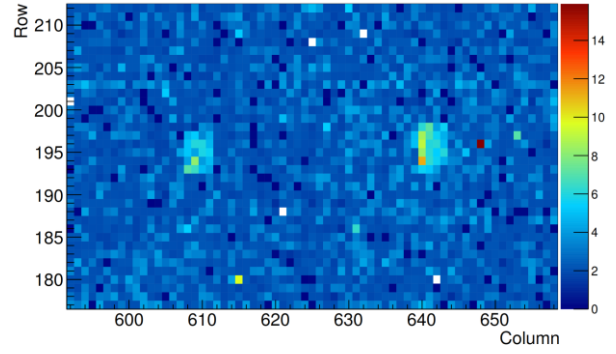
### 5.3.6 Test 6- Radiation Effect

In this study three ALPIDE chips were used mainly for characterizing. As mentioned in section-5.2, two of them are irradiated with different particles with different energy but some radiation effect was noticed only in chip-2 from the irradiation by “Helium-4” ion.

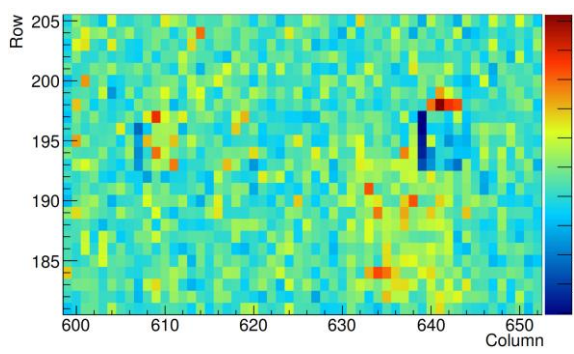
Chip-1 and 2 went through the micro beam experiment with Helium-4 ion in Australia Nuclear Science and Technology Organisation (ANSTO), Australia in January 2018. These two chips were tested for radiation damage in April 2018. A random threshold scan with  $V_{BB}=0V$  to  $-6V$  was performed for this test and a permanent radiation effect is observed in the noise and threshold map for chip-2. It is said permanent as it wasn't healed by the chip itself in three months. Figure-47 shows how the affected pixel matrixes in chip-2 look, both in terms of threshold and noise level. The highly irradiated pixel matrixes are visible at  $V_{BB}=-3V$  to  $-6V$ . But at  $0V$  (without bias) these pixels are not visible in thresholdmap due to higher threshold value but noisemap still confirms the poor performance of those affected pixels with the high noise level.



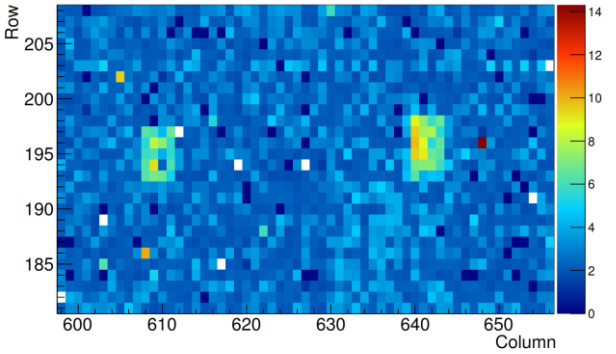
(a) Thresholdmap,  $V_{BB}=-6V$ .



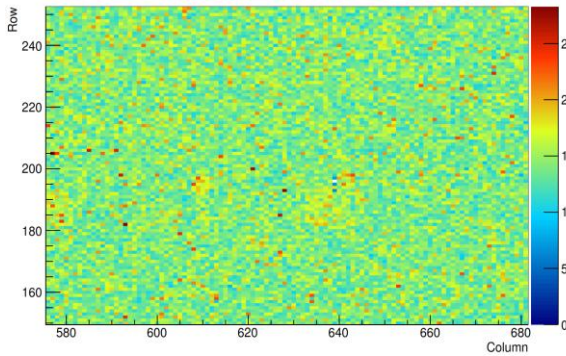
(b) Noisemap,  $V_{BB}=-6V$ .



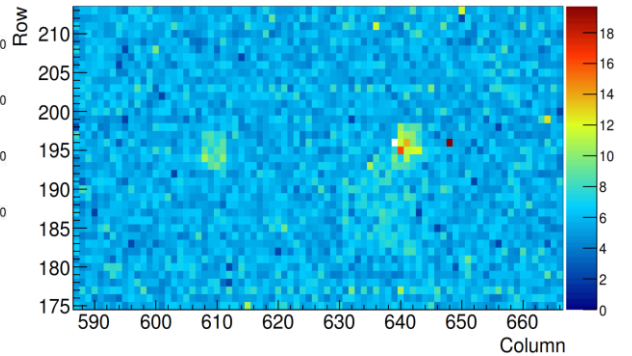
(c) Thresholdmap,  $V_{BB}=-3V$ .



(d) Noisemap,  $V_{BB}=-3V$ .



(e) Thresholdmap,  $V_{BB}=0V$ .



(f) Noisemap,  $V_{BB}=0V$ .

**Figure 47: Radiation effect in chip-2 in terms of threshold and noise level. Affected pixels in (a) thresholdmap at  $V_{BB}=-6V$  (b) noisemap at  $V_{BB}=-6V$  (c) thresholdmap at  $V_{BB}=-3V$  (d) noisemap at  $V_{BB}=-3V$  (e) thresholdmap at  $V_{BB}=0V$  (f) noisemap at  $V_{BB}=0V$ .**

The pixels got hit are also seen in data file. Figure-48 shows how the address and hit information are recorded in the data file.

639	200	6527	819497419	13
639	201	6527	819497419	13
638	201	6527	819497419	13
638	202	6527	819497419	13
639	202	6527	819497419	13
639	203	6527	819497419	13
640	200	6527	819497419	13
641	201	6527	819497419	13
640	201	6527	819497419	13
640	202	6527	819497419	13
641	202	6527	819497419	13
640	203	6527	819497419	13
638	201	6528	819498219	4
638	202	6528	819498219	4
641	201	6528	819498219	4
639	196	6551	819516623	13
639	197	6551	819516623	13
638	197	6551	819516623	13
638	198	6551	819516623	13
639	198	6551	819516623	13

**Figure 48: Pixels in the irradiated area (addresses are encircled).**

Despite being in the same irradiated area all pixels don't receive the same dose, therefore, the threshold and noise value varies pixel to pixel (cf. figure-47). This is because of beam moving pattern illustrated in figure-49. The red line shows how the Beam Spot<sup>10</sup> moved to cover the entire area. The ion incidence rate is decreasing with time, the more they move to the right the lesser they deposit dose.

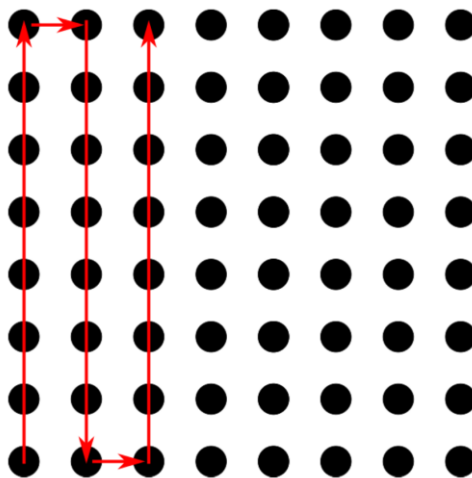


**Figure 49: Beam pattern. The red arrows show the way the beam spot is moving. Each dot represents a beam spot, and the beam spot stays in one position for a certain time, the dwell time<sup>11</sup>, before it skips to the next position [99].**

<sup>10</sup> Beam Spot: Where the beam hits.

<sup>11</sup> Dwell Time: The time the beam spot stays in one position before it moves to the next is called the Dwell Time (DT).

### 5.3.6.1 Threshold and Noise for highly irradiated Pixels

There were four areas irradiated by the Helium-4 ion. Two areas of  $128 \times 128 \mu\text{m}^2$  and two “L” shaped area of  $2048 \mu\text{m}^2$ , shown in figure-50. The scanning details of these four areas are attached in section-A.2.

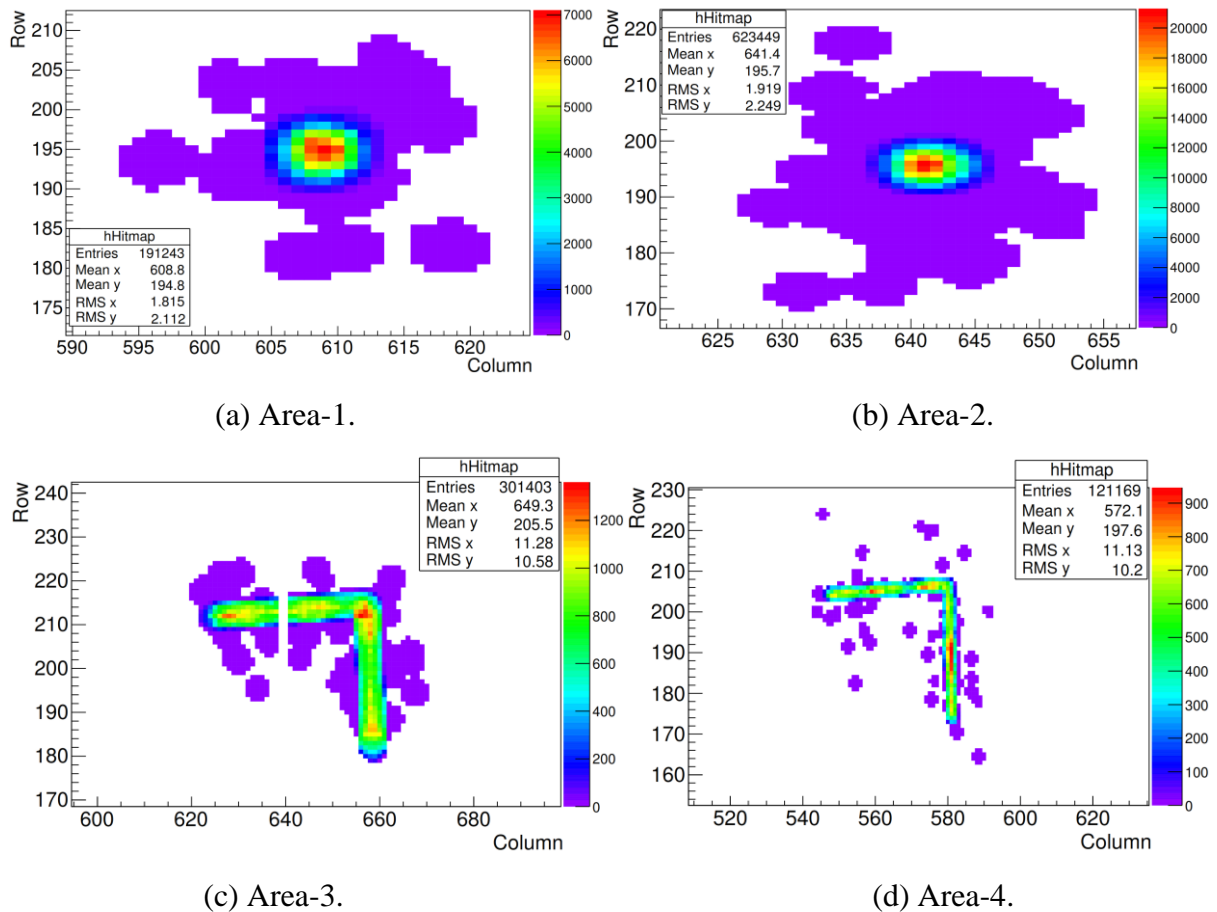


**Figure 50: Activated pixel in a small irradiated area (a)  $128 \times 128 \mu\text{m}^2$  (b)  $128 \times 128 \mu\text{m}^2$  (c) L shape area of  $2048 \mu\text{m}^2$  (d) L shape area of  $2048 \mu\text{m}^2$ .**

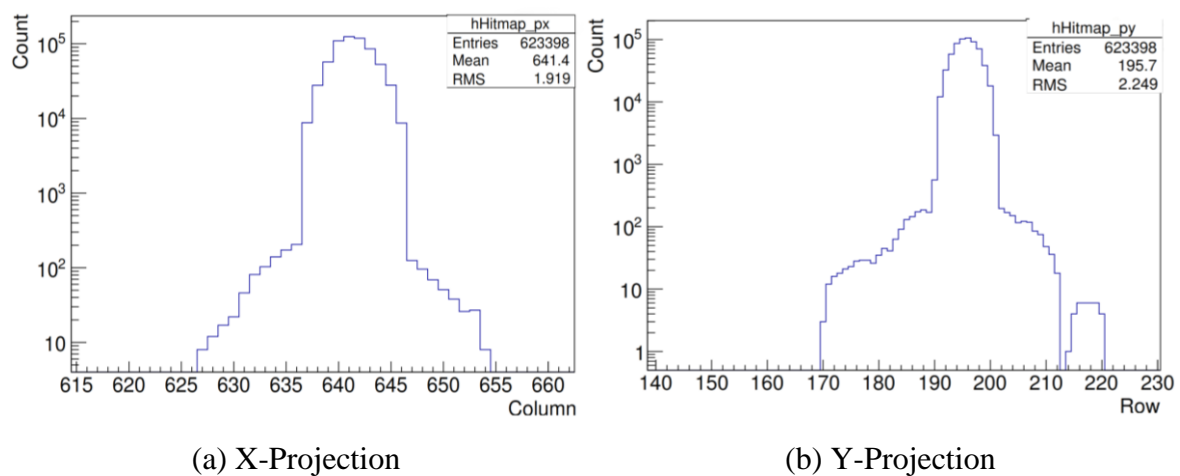


**Figure 51: Projection of hits from X and Y axis for Area-2 showing maximum hits in inner most few pixels.**

The total number of hit pixel in area 1 & 2 was 81 (Counted from the data file) and from the figure-50(a) & (b) it is seen that the inner most 9 pixels got the highest dose and registered with maximum hit. The projection of hit for Area-2 (cf. figure-50b) is illustrated in figure-51.

In Area- 1 & 2, matrix of innermost 9 pixels shows high deviation from the regular threshold and noise value (cf. figure-47). The pixels in the “L” shaped area, shown in figure-50(c) & (d), don’t show any radiation effect.

Radiation effect leads to a reduced threshold value and increased noise value for a pixel. Before measuring these threshold and noise values for the highly irradiated pixels, it should be noted that they are measured with  $V_{BB}=-6V$  to have clear distinguishability. The mean threshold measured for full chip-2 at  $V_{BB}=-6V$  is 125.8 with standard deviation 17.82 and the mean noise is 2.26 with standard deviation 0.85 (cf. figure-36).

Figure-52 shows the thresholdmap and threshold value for 81 irradiated pixels in Area-2 (cf. figure-50b) and the mean threshold value is measured 106. The noisemap and noise value is shown in figure-53 and mean noise value is measured 3.581.

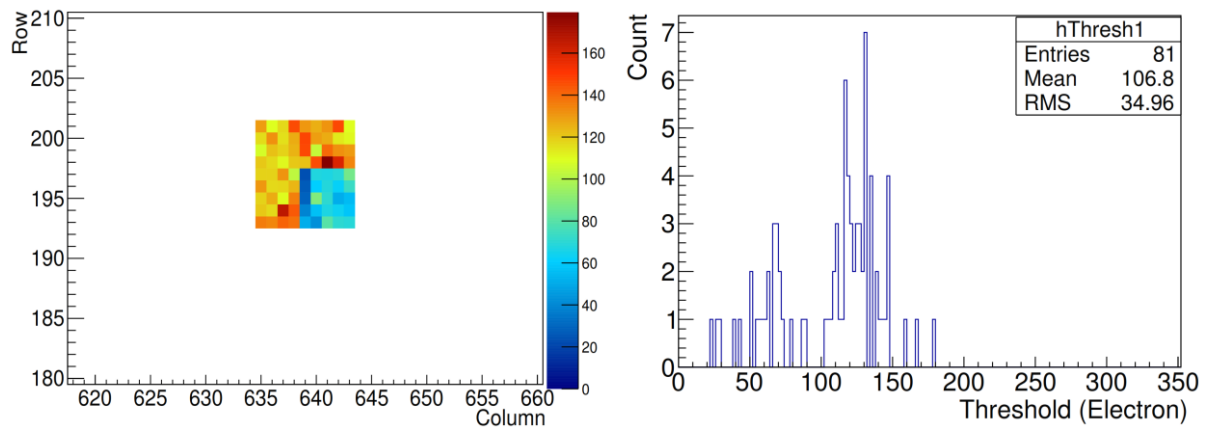


**Figure 52: Thresholdmap (Left), Threshold value of irradiated pixels (Right).**

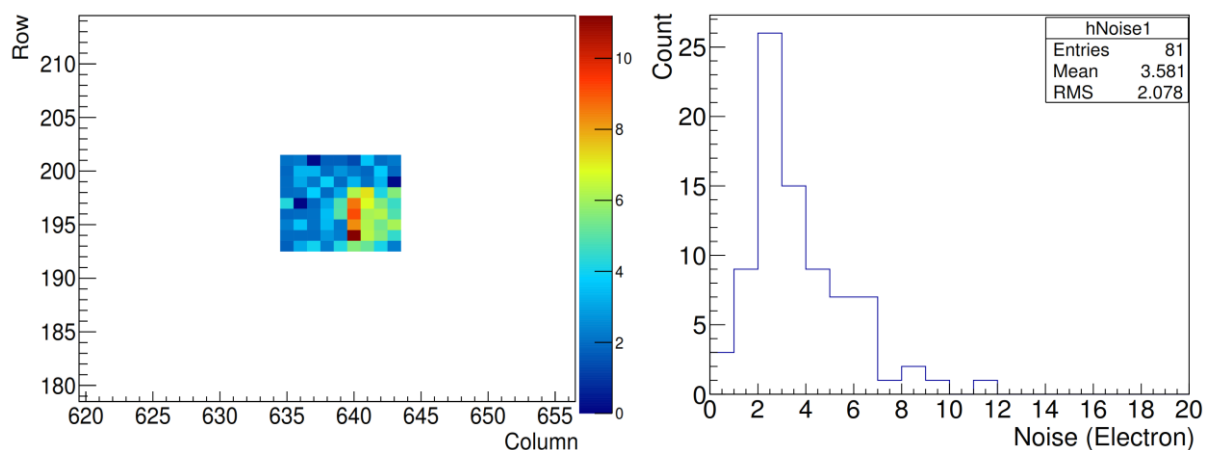


**Figure 53: Noisemap (Left), Noise value of irradiated pixels (Right).**

Now, the inner most highly irradiated 9 pixels in Area-2 (cf. figure-50b) give mean threshold around 65, illustrated in figure-54 and mean noise around 7, illustrated in figure-55. These values are far beyond the mean values (including standard deviation) for the whole chip. So this cannot be any random deviation in fact this is a consequence of radiation effect.

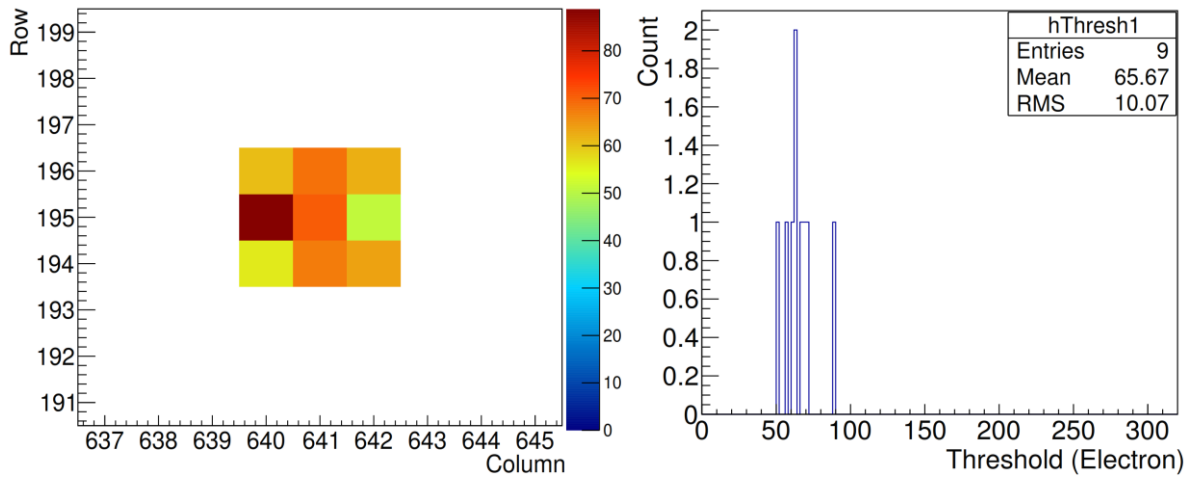


**Figure 54: Thresholdmap (Left), Threshold value for affected pixels (Right).**

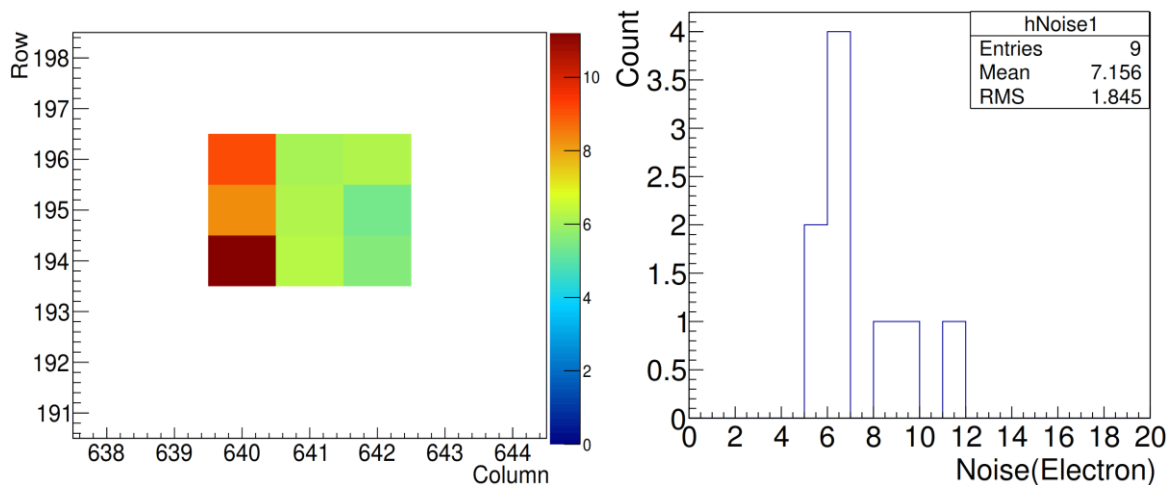


**Figure 55: Noisemap (Left), Noise value for affected pixels (Right)**

Similarly, for the highly irradiated 9 pixels in Area-1 (cf. figure-50a), the recorded threshold and noise value is 91 and 5.6 respectively, shown in figure-56.

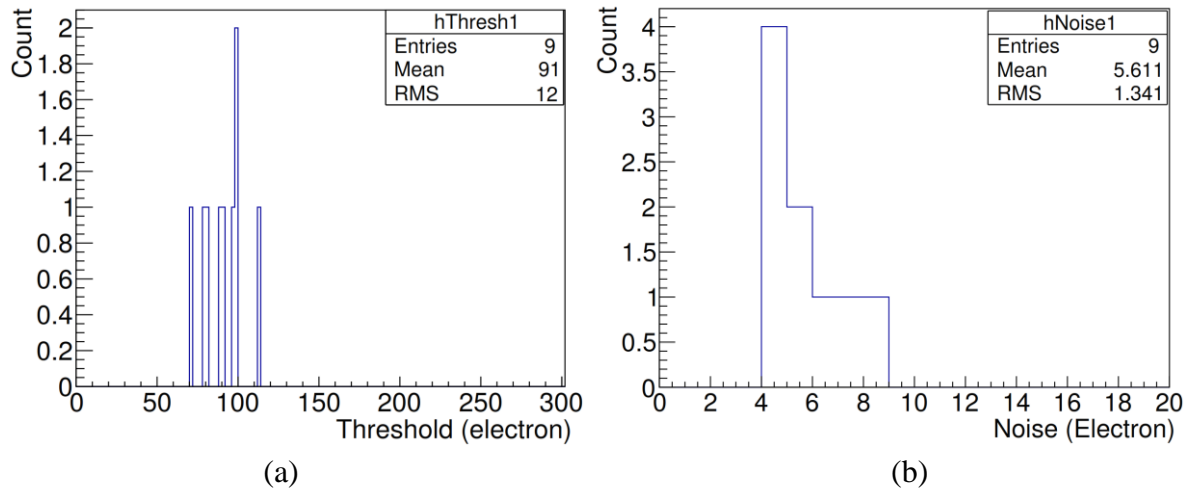


Figure 56: (a) Threshold and (b) Noise value for affected pixels.

### 5.3.6.2 Mean Threshold and Noise versus Total Accumulated Dose (Gy)

When micro beam of Helium-4 ion hits the chip, it deposits high energy to that specific area. The four irradiated areas on chip-2 (cf. figure-50) received different doses and most likely the pixels showing high noise level had the maximum dose. The dose deposition in four areas are calculated as follows [99],

We know, Depth of ALPIDE epitaxial layer  $25\mu\text{m}$

Silicon density  $2.329\text{ g/cm}^3$

Inside the epitaxial layer the assumed average energy of Helium-4 ion is 9 MeV and the energy loss is  $95.5\text{ keV}/\mu\text{m}$ .

Spot pitch<sup>12</sup> of the beam was  $1\mu\text{m}$

#### Area-1

$$\begin{aligned} \text{The irradiated mass in Area-1} &= 128 \times 128 \times 25 \mu\text{m}^3 \times (10^{-4} \text{ cm}/\mu\text{m})^3 \times 2.329 \text{ g/cm}^3 \\ &= 9.54 \times 10^{-10} \text{ Kg} \end{aligned}$$

$$\begin{aligned} \text{Energy loss per Helium Ion} &= 95.5 \text{ KeV}/\mu\text{m} \times 25 \mu\text{m} \times 1.6 \times 10^{-16} \text{ J/KeV} \\ &= 3.82 \times 10^{-13} \text{ J} \end{aligned}$$

$$\begin{aligned} \text{Dose per small mass} &= 3.82 \times 10^{-13} \text{ J} / 9.54 \times 10^{-10} \text{ Kg} \\ &= 4 \times 10^{-4} \text{ Gy} \end{aligned}$$

<sup>12</sup> Spot pitch- Distance between two beam spot.

Area-1 was irradiated 4 times. Dose calculation for each time is following,

- 1) When, Ion rate 2 KHz (Assuming constant)  
Dwell Time 100 ms

$$\text{Calculated Dose} = 128 \times 128 \times 2000 \text{ Hz} \times 0.1 \text{ s} \times 4 \times 10^{-4} \text{ Gy} = 1,310.72 \text{ Gy}$$

- 2) For same Ion rate and dwell time,  
Calculated Dose = 1,310.72 Gy

- 3) When, Ion rate 10 KHz (Assuming constant)  
Dwell Time 100 ms

$$\text{Calculated Dose} = 6,553.6 \text{ Gy}$$

- 4) For same Ion rate and dwell time,  
Calculated Dose = 6,553.6 Gy

$$\begin{aligned} \text{Total Dose in Area-1} &= 1,310.72 \text{ Gy} + 1,310.72 \text{ Gy} + 6,553.6 \text{ Gy} + 6,553.6 \text{ Gy} \\ &= 15,728.64 \text{ Gy} \end{aligned}$$

### **Area-2**

Area-2 was irradiated 3 times. Dose calculation for each time is following,

- 1) When, Ion rate 10 KHz (Assuming constant)  
Dwell Time 200 ms

$$\text{Calculated Dose} = 13,107.2 \text{ Gy}$$

- 2) For same Ion rate and dwell time,  
Calculated Dose = 13,107.2 Gy

- 3) When, Ion rate 10 KHz (Assuming constant)  
Dwell Time 100 ms

$$\text{Calculated Dose} = 6,553.6 \text{ Gy}$$

$$\begin{aligned} \text{Total Dose in Area-2} &= 13,107.2 \text{ Gy} + 13,107.2 \text{ Gy} + 6,553.6 \text{ Gy} \\ &= 32,768.0 \text{ Gy} \end{aligned}$$

### **Area-3**

The irradiated mass in Area-3 =  $2048 \times 25 \mu\text{m}^3 \times (10^{-4} \text{ cm} / \mu\text{m})^3 \times 2.329 \text{ g/cm}^3$

$$= 1.19 \times 10^{-10} \text{ Kg}$$

$$\text{Energy loss per Helium Ion} = 95.5 \text{ KeV}/\mu\text{m} \times 25 \mu\text{m} \times 1.6 \times 10^{-16} \text{ J/KeV}$$

$$= 3.82 \times 10^{-13} \text{ J}$$

$$\text{Dose per small mass} = 3.82 \times 10^{-13} \text{ J} / 1.19 \times 10^{-10} \text{ Kg}$$

$$= 3.2 \times 10^{-3} \text{ Gy}$$

Area-3 was irradiated once. Dose calculation is following,

When, Ion rate 10 KHz (Assuming constant)

Dwell Time 200 ms

$$\text{Calculated Dose} = 2048 \times 10^4 \text{ Hz} \times 0.2 \text{ s} \times 3.2 \times 10^{-3} \text{ Gy} = 13,107.2 \text{ Gy}$$

$$\text{Total Dose in Area-3} = 13,107.2 \text{ Gy}$$

#### Area-4

Area-4 was irradiated once. Dose calculation is following,

When, Ion rate 10 KHz (Assuming constant)

Dwell Time 200 ms

$$\text{Calculated Dose} = 13,107.2 \text{ Gy}$$

$$\text{Total Dose in Area-4} = 13,107.2 \text{ Gy}$$

The change in mean threshold and noise value over dose is illustrated in figure-57.

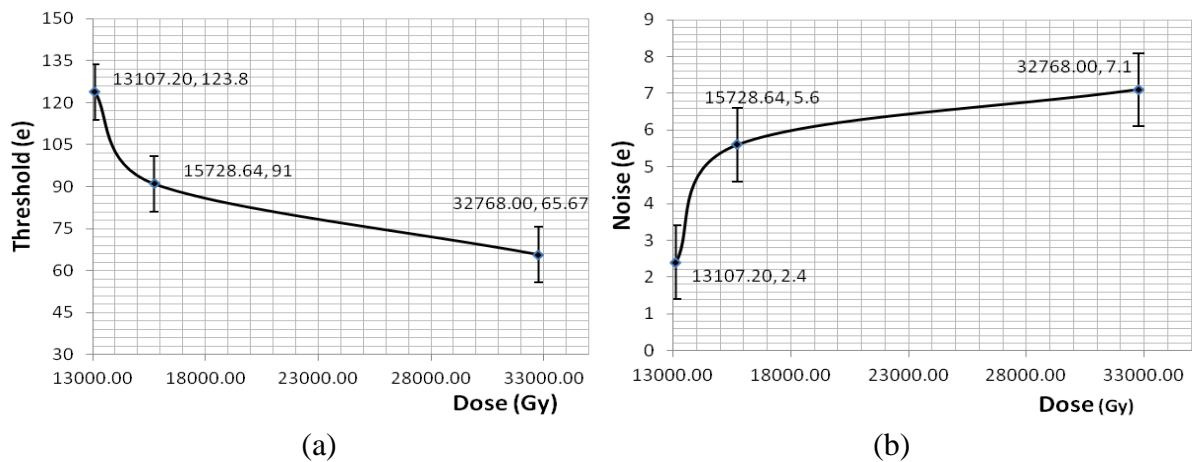


**Figure 57: Mean (a) Threshold and (b) Noise over Dose.**

In section-3.5, the possible radiation damage effects are discussed and it gives a clear understanding that radiation-induced effects, such as increase of leakage current leads to the increased shot noise of the device and degrades device performance, also surface defect due to ionizing radiation causes a shift in threshold and noise. From our analysis of the highly irradiated pixels on chip-2, reduced threshold and increased noise level is determined as an indication of radiation effect but it is hard to interpret what types of defect took place, but the assumption says that the structural damage of silicon chip can happen due to the high energy Helium ion knocking out the silicon atom or dopant atoms from their normal position without any charge generation. This leads to electronic effect through structural damage. The surface defect slowly shifts device parameter until the device doesn't work anymore and mainly occurs because of chronic exposure to radiation. So far, the pixels that were analyzed in this study did not receive radiation over a long period of time but it certainly deposits a high amount of dose that might also cause the damage.

### **5.3.6.3 Compensating for Radiation Damage**

It is almost impossible to fix the pixels which are affected, but in order to use the chip for next experiment these pixels can be masked to avoid any reading from them. Also, since the threshold and noise level is known for pixels, the result of any performed test can be adjusted in accordance.

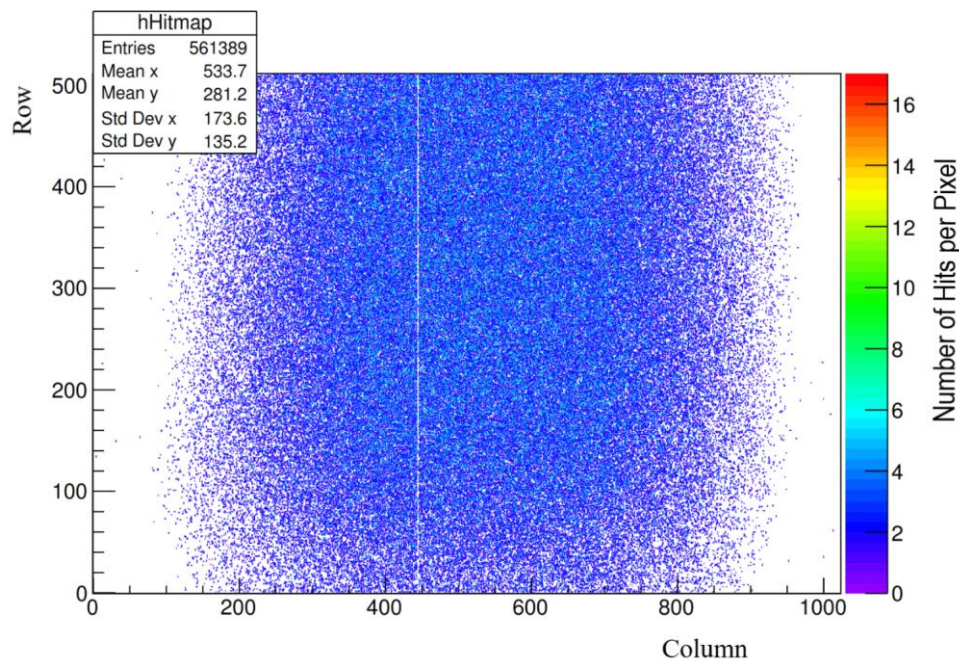
## 5.4 Cluster Analysis

### 5.4.1 Alpha Beta and Gamma Source

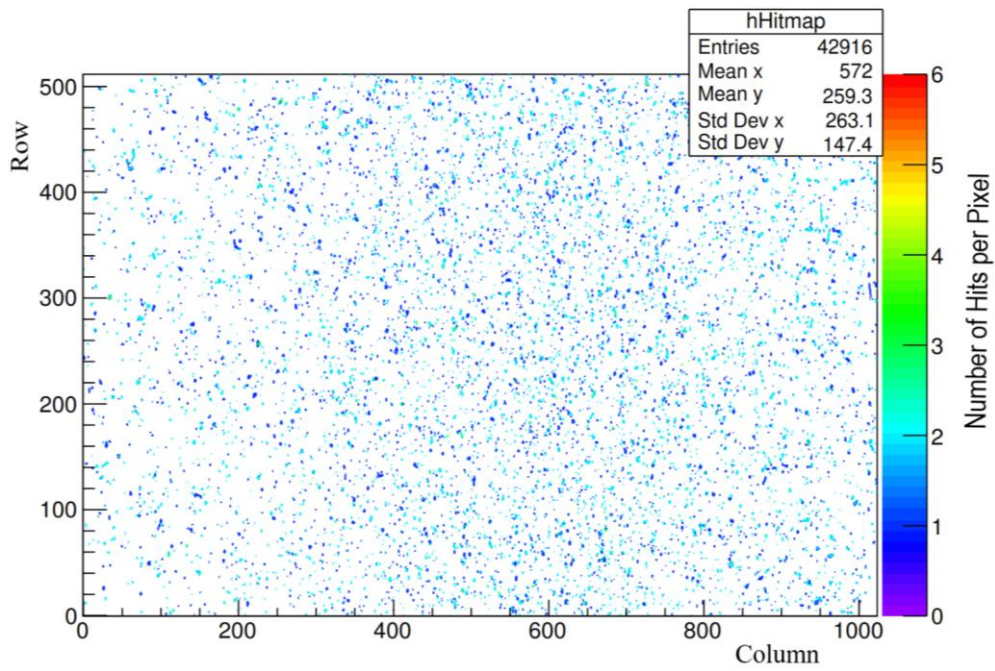
Three forms of ionizing radiation caused by unstable atoms are alpha, beta, and gamma. The ALPIDE cluster size analysis begins with checking the response of the chip to particles and that was carried out using some radioactive sources. For this study radioactive sources,  $^{55}\text{Fe}$  emitting photons,  $^{90}\text{Sr}$  emitting electrons and  $^{241}\text{Am}$  emitting alpha are used (cf. section- 4.5). The particle, emitted by  $^{55}\text{Fe}$ , gives energy almost equal to the most probable energy loss of Minimum Ionizing Particles (MIPs).

Only chip-1 was scanned with different sources with an external event/strobe number of 10000 and  $V_{\text{BB}}=0\text{V}$ . Figure-58 shows hitmap for each source. The hitmap for gamma shows a broken column which is not visible in other hitmaps and this might be because of a large number of pixels hit by photons from  $^{55}\text{Fe}$ , shown in figure-58(a), than beta and alpha, shown in figure- 58(b) and 58(c) respectively. The reason why more pixels are hit by gamma is the longer penetration depth in matter.

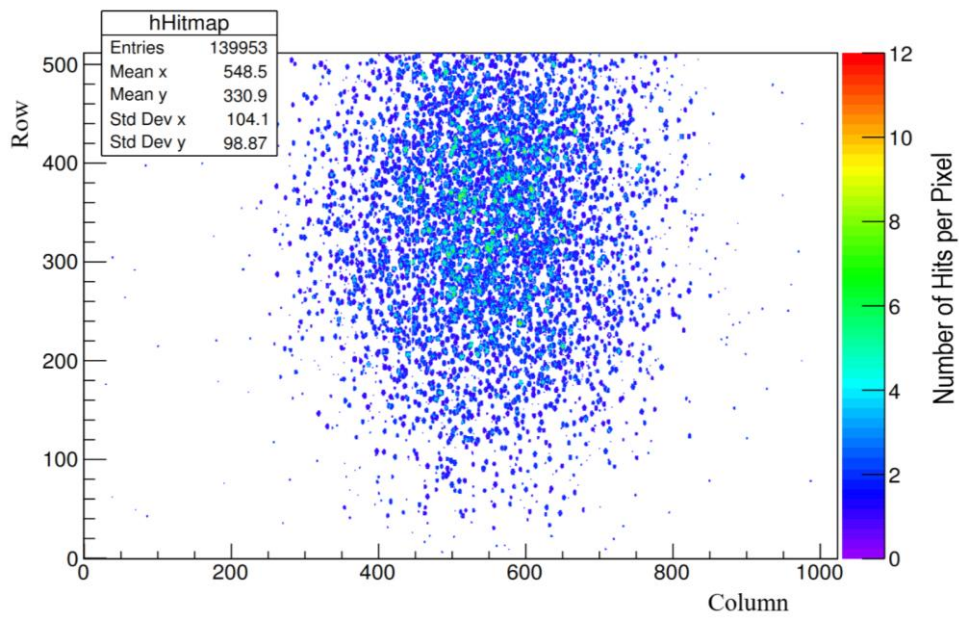
#### 5.4.1.1 Hitmaps



(a) Hitmap for Gamma [ $^{55}\text{Fe}$ ].



(b) Hitmap for Beta [ $^{90}\text{Sr}$ ].

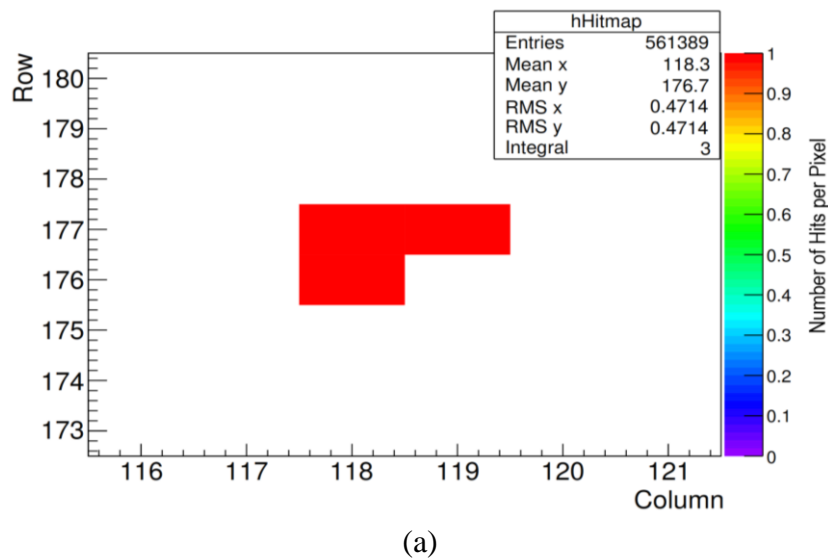


(c) Hitmap for Alpha [ $^{241}\text{Am}$ ].

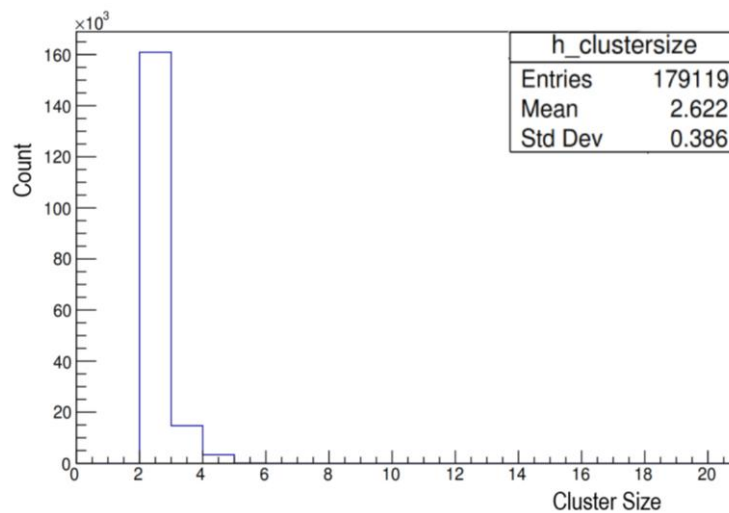
Figure 58: Hitmap for (a) Gamma (b) Beta (c) Alpha.

### 5.4.1.2 Cluster Size

Figure-59 shows cluster size distribution for each particle. Figure-59(a) shows a typical cluster by X-ray. The spectrum of cluster size for gamma, originating from  $^{55}\text{Fe}$  source, shows one significant peak illustrated in figure-59(b). This happens when the particle hits the reflective boundaries of the epitaxial layer and all generated charge carrier are collected by the group of pixels. This single peak also manifests localized charge deposition of gamma. The lower signals values appear as a tail in the histogram can be caused by the absorption of a photon in the substrate and thus all generated charge is not able to reach the epitaxial layer and leads to less collection of charge by the charge collecting diode.



(a)



(b)

**Figure 59: (a) A single event cluster of Gamma (b) Cluster Size histogram for Gamma.**

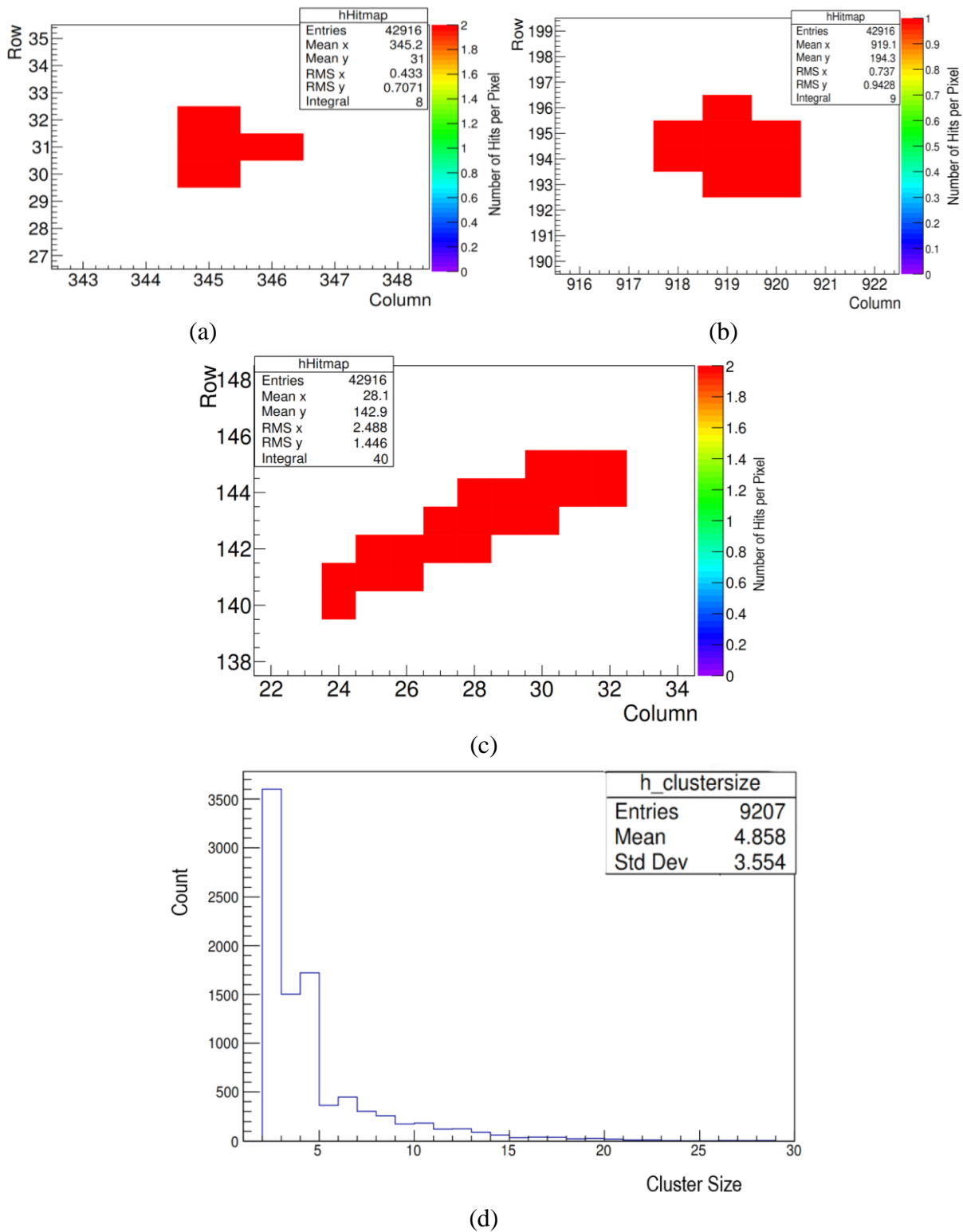
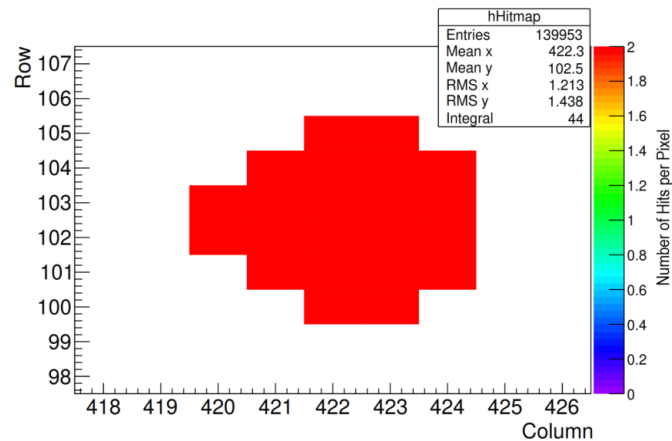


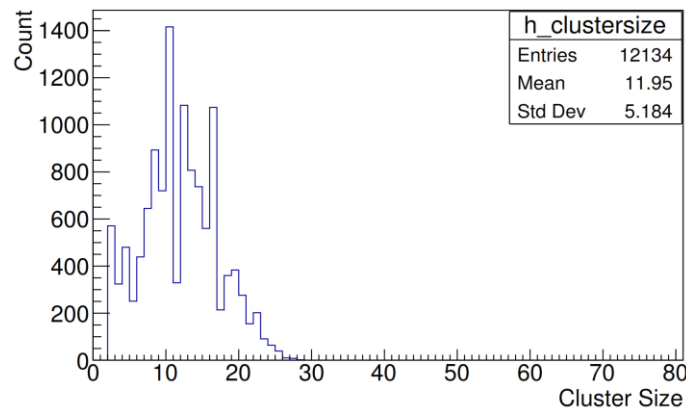
Figure 60: (a) Single event cluster for MIPS particle (b) Single event cluster for low energetic electron (c) A beta track (d) Cluster size histogram for Beta.

The smaller clusters in the histogram, shown in figure-60(d) are produced from the high energetic beta particle that usually goes through the sensor. This high energy beta particles of 2.27 MeV, referred as MIPS particle loses energy along their path that gives a particle track, illustrated in figure-60(c). Figure-60(a) shows a typical single event cluster for MIPS.

Low energetic electron loses more energy in the epitaxial layer therefore produces fat cluster, illustrated in figure-60(b).

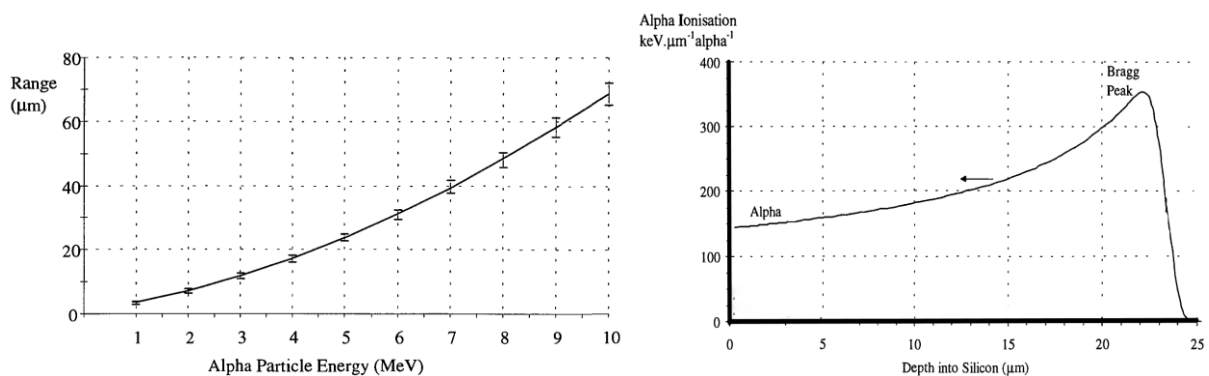


(a)



(b)

**Figure 61: (a) A rare big single event cluster for Alpha (b) Cluster size histogram for Alpha.**



(a)

(b)

**Figure 62: (a) Range of alpha particles in silicon (b) Ionisation energy loss along a particle track due to nearly 5 MeV alpha particle [100].**

For alpha particle, a big cluster is shown in figure-61(a). Now as a heavy charged particle alpha loses energy while traversing a material. From figure-62(a) range of alpha particle with energy 5486 KeV can be estimated and that is around 25  $\mu\text{m}$ . Figure-62(b) shows the maximum ionization energy loss for the same energy alpha particle at depth nearly 25  $\mu\text{m}$ . This illustration leads to an understanding that alpha particle of 5486 KeV losses all its energy at the epitaxial layer of ALPIDE as the epitaxial layer is itself 25  $\mu\text{m}$  deep. This high energy deposition and ionization rate helps to create fat cluster size that is shown in figure-61(b).

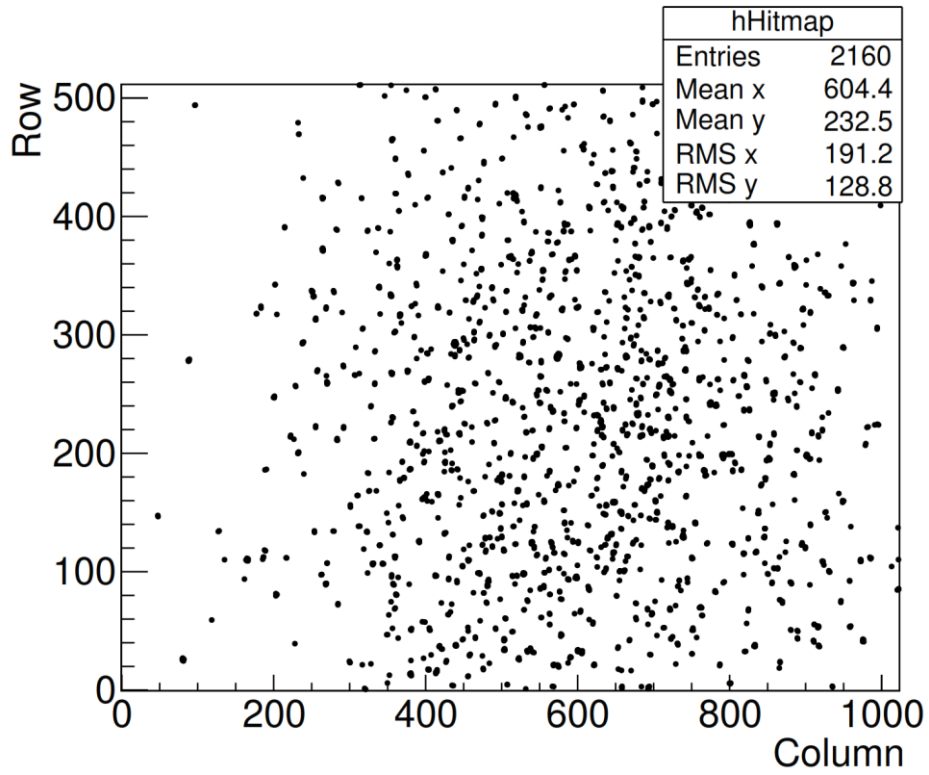
Cluster size is dependent on the threshold. It is known that at lower threshold value the frequency of larger clusters is slightly overestimated whereas the occurrence of single pixel clusters is overestimated at the higher threshold (more details is available here [71]). To eliminate this problem threshold value 131.4, was fixed for scanning all the sources by keeping  $V_{\text{BB}}=0\text{V}$ ,  $\text{ITHR}=50$  and  $\text{VCASN}=50$ . This set up also ensure that change in cluster sizes is not influenced by any other parameter except the type and energy of the particle.

#### 5.4.2 X-ray Source Test

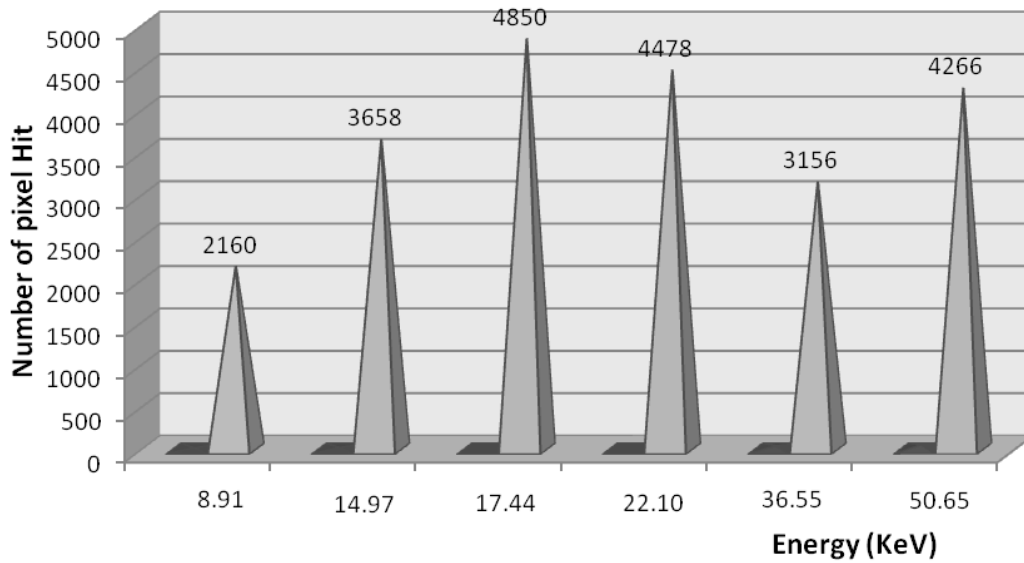
ALPIDE detector was irradiated by X-rays of six different energies (cf. Table-6). This energy change is based on isotope type and the orbital from where X-rays are generated. This experiment was done only on chip-1. Source scanning was performed for 5000 trigger at  $V_{\text{BB}}=0\text{V}$ .

Figure-63(a) shows how the activated pixels are presented in the hitmap and numbers are shown in the statistics box as “Entries”. Figure-63(b) illustrates energy vs. number of entries or activated pixel. The changing pattern of entries with energy shows efficiency of sensor as the photon sources had same geometrical acceptance or same luminosity. Also, the time ( $\approx 15$  mins) for all individual source scan was same.

Soft X-rays ( $<100$  keV) interact predominantly via the photoelectric effect with silicon. The energy is transferred from photon to generated photoelectron. Energy transfer to photoelectron increases with increasing energy of incident photon. A lower energetic photoelectron doesn't interact much with the matter but when the energy of photoelectron is high it can act like beta particle by interacting with matter and create more charge in medium and eventually increases the number of entries. From figure-63(b), we find a pattern of entries starting with a rise and then followed by a fall and rise again. This change in number of entries over energy might cause from the fluctuation of source activity as from the user manual we know that all X-ray sources were with activity of between 1 and 10  $\mu\text{Ci}$  [98].



(a)



(b)

Figure 63: (a) Hitmaps showing number of entries for X-ray with energy 8.04 and 8.91 KeV from Cu (b) Energy vs. Number of pixel hit.

The different interaction probability according to energy is given in Table-9 along with the percentage of energy attenuated, absorbed and transmitted. Here probability is calculated by X-Ray attenuation & absorption calculator [101]. For this calculation Silicon thickness was used 25  $\mu\text{m}$ , which is the epitaxial layer thickness of ALPIDE.

**Table 9: Interaction probability with changing X-ray energy for Silicon**

<b>X-ray Energy (KeV)</b>	<b>Interaction probability</b>	<b>Total Energy Distribution</b>
8.91	Photoabsorption: 23.6939 Compton Scattering: 0.0516 Rayleigh Scattering <sup>13</sup> : 0.3621	Attenuation [%]: 24.1075 Transmission [%]: 75.8925 Energy Absorption [%]: 23.5510
14.97	Photoabsorption: 5.5813 Compton Scattering: 0.0726 Rayleigh Scattering: 0.2028	Attenuation [%]: 5.8566 Transmission [%]: 94.1434 Energy Absorption [%]: 5.5569
19.63	Photoabsorption: 2.4875 Compton Scattering: 0.0800 Rayleigh Scattering: 0.1382	Attenuation [%]: 2.7057 Transmission [%]: 97.2943 Energy Absorption [%]: 2.4802
24.99	Photoabsorption: 1.2034 Compton Scattering: 0.0855 Rayleigh Scattering: 0.0975	Attenuation [%]: 1.3864 Transmission [%]: 98.6136 Energy Absorption [%]: 1.1961
36.55	Photoabsorption: 0.3671 Compton Scattering: 0.0896 Rayleigh Scattering: 0.0537	Attenuation [%]: 0.5104 Transmission [%]: 99.4896 Energy Absorption [%]: 0.3710
50.65	Photoabsorption: 0.1290 Compton Scattering: 0.0896 Rayleigh Scattering: 0.0307	Attenuation [%]: 0.2493 Transmission [%]: 99.7507 Energy Absorption [%]: 0.1365

<sup>13</sup> Rayleigh Scattering: This is the scattering of the Electromagnetic radiation by a particle with radius close to 1/10 the of the radiation wavelength.

### 5.4.2.1 Cluster Size

Cluster sizes at different X-ray energy are shown in figure-64. It can be seen that the mean value of cluster size increases with increasing energy, shown in figure-64(a) to 64(e). Figure-64(f) shows a bit reduced mean cluster size because part of the energy is transmitted through the sensor. Figure-65 shows energy vs. mean cluster size.

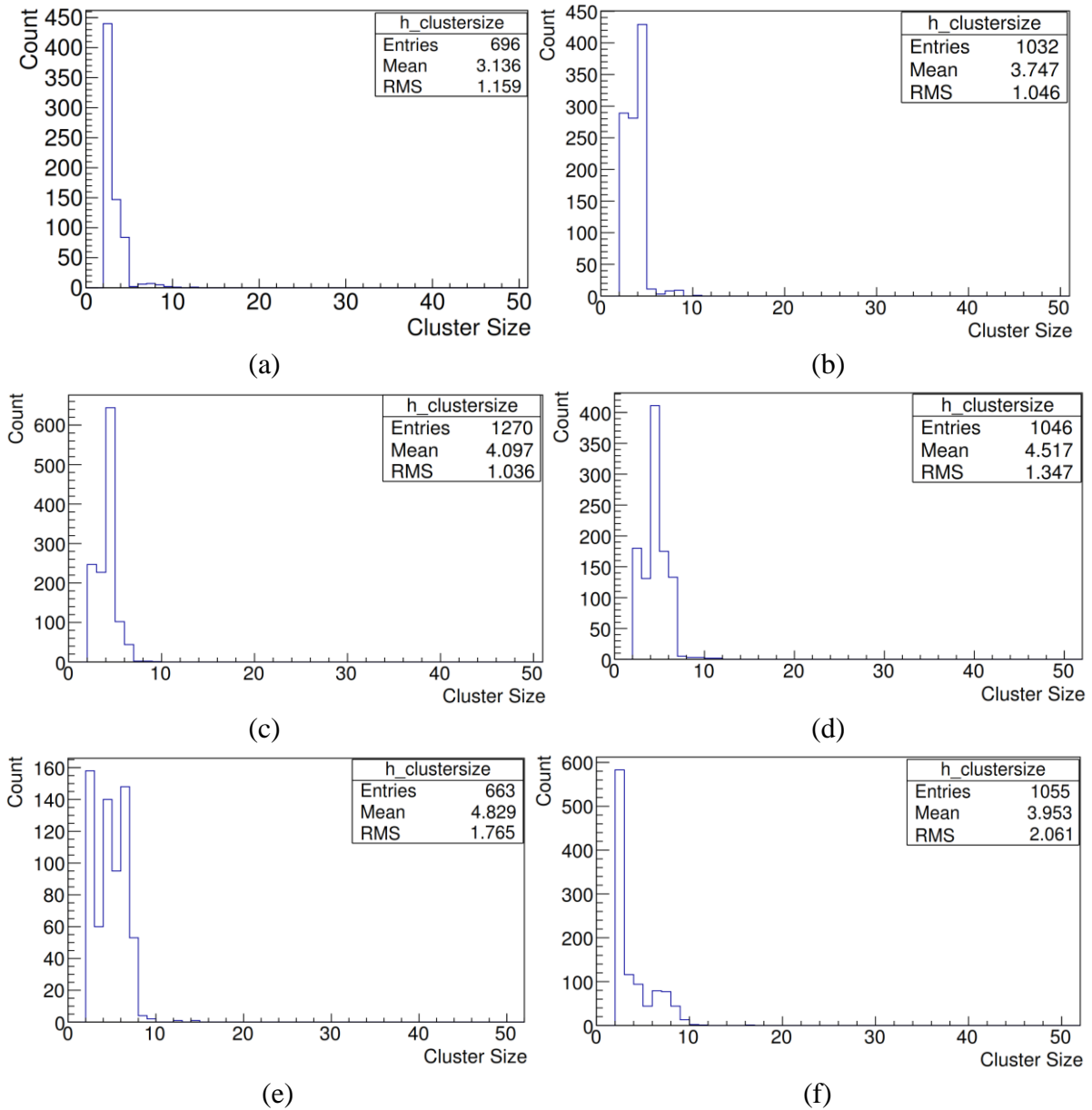


**Figure 64: Cluster size histogram for X-ray with energy (a) 8.04 and 8.91 KeV from Cu (b) 13.37 and 14.97 KeV from Rb (c) 17.44 and 19.63 KeV from Mo (d) 22.10 and 24.99 KeV from Ag (e) 32.06 and 36.55 KeV from Ba (f) 44.23 and 50.65 KeV from Tb.**

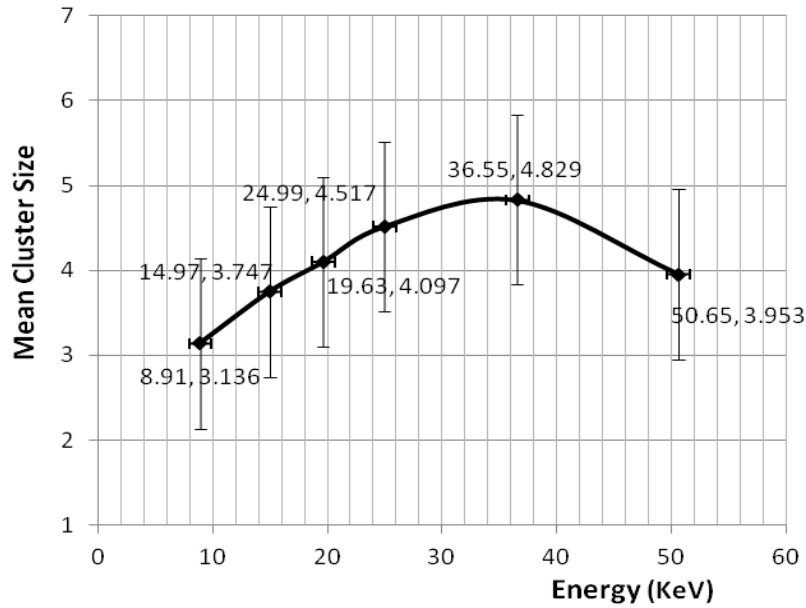


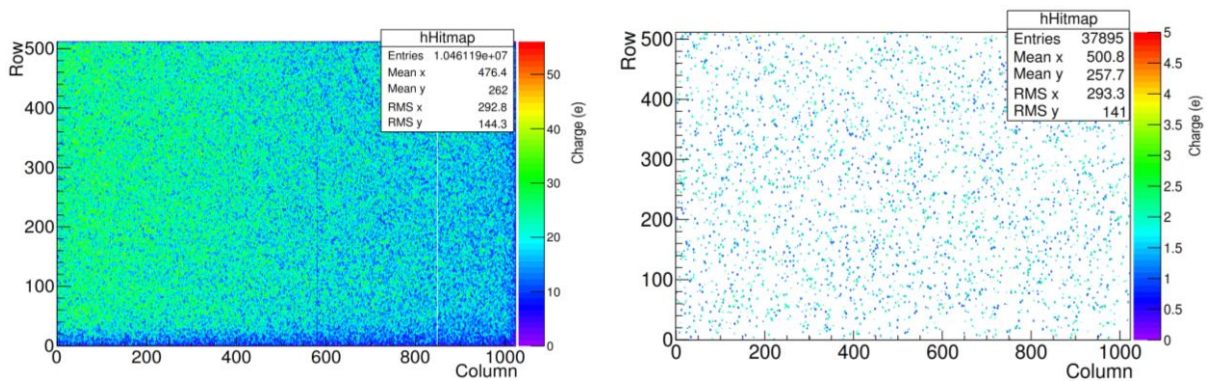
Figure 65: Energy vs. Mean cluster size.

### 5.4.3 Proton Beam Test

The ALPIDE chip-W07R15 was used for proton beam test. Required setup and configuration for this test is discussed in section-4.6. In this section we will show the hitmaps for proton and how typical proton clusters look.

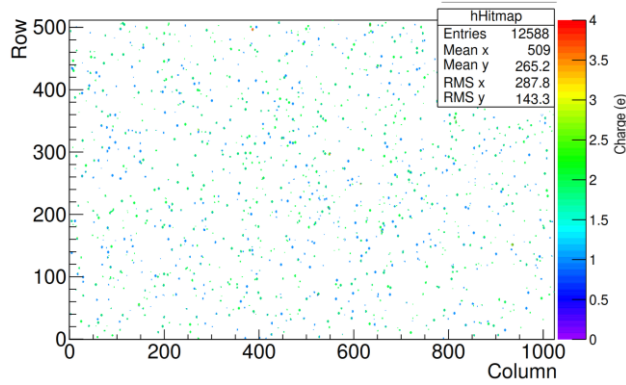
#### 5.4.3.1 Entries over Angle

Particle intensity drops over increasing angle between beam trail and ALPIDE chip and thus the number of hit pixel also goes down. Figure-66 shows how the hitmaps look at different angle where the distance was fixed at a certain range from approximately 1.6 m to 1.7 m. Data was collected for  $V_{BB}=-6V$ .



(a) Angle 12.2, Distance 1.704.

(b) Angle 45.2, Distance 1.666.

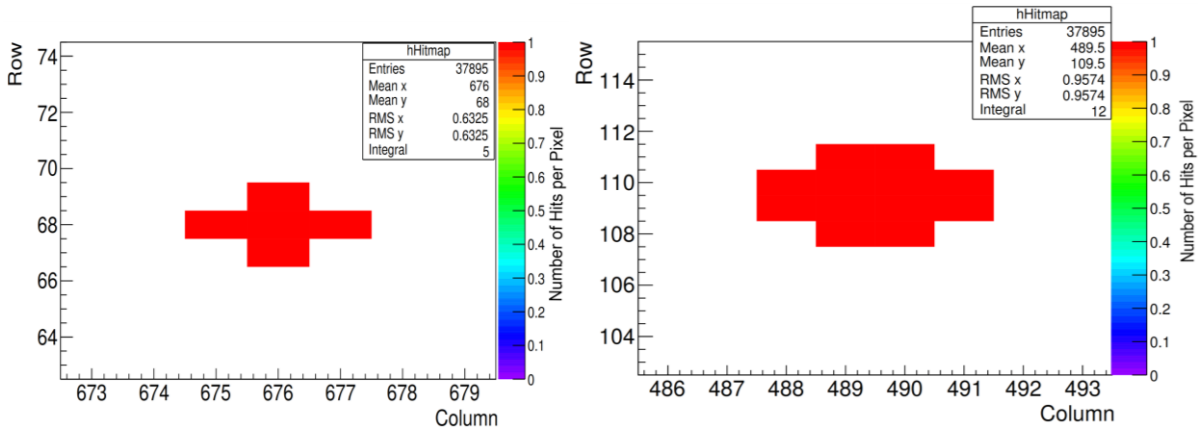


(c) Angle 58.1, Distance 1.65.

Figure 66: Hitmaps for proton beam at  $V_{BB}=-6V$ .

### 5.4.3.2 Proton Cluster size

Figure-67 shows cluster sizes for proton at  $V_{BB}=-6V$  and at 1.6 m distance. High reverse bias voltage gives relatively smaller cluster size because detector charge collection efficiency increases and charge does get enough time to diffuse. Therefore, at  $V_{BB}=-6V$  the bigger cluster generally consist of 10-14 pixels, shown in figure-67(b) and smaller one consists of 5-7 pixels, shown in figure-67(a). Here the mean cluster size is  $\approx 7$ . Figure-68 shows the cluster size histogram at  $V_{BB}=0V$  and at the same distance (1.6 m). Here the mean cluster size is  $\approx 18$ . At  $V_{BB}=0V$  the cluster size is always bigger because of less charge collection efficiency of sensing diode and more diffusion of charge.



(a) Smaller cluster.

(b) Bigger cluster.

Figure 67: Clusters for proton at  $V_{BB}=-6V$ .

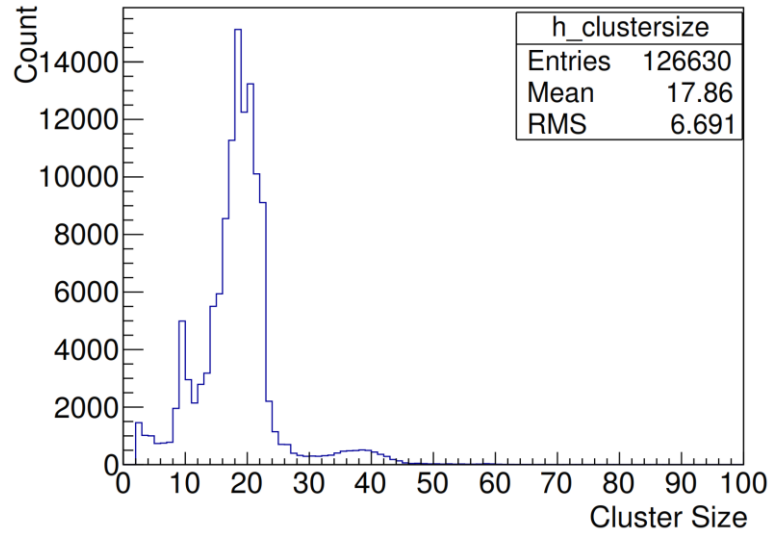


**Figure 68: Cluster Size histogram for proton at  $V_{BB}=0V$  and 1.6 m distant.**

#### 5.4.4 Energy Deposition/LET versus Cluster Size

Figure-69 shows the relationship between energy depositions and cluster size. The energy deposition in the 25  $\mu\text{m}$  epitaxial layer of the sensor can be expressed as LET. The cluster sizes are taken at  $V_{BB}=0V$  and with same strobe duration.

A 5 MeV  $\alpha$  particle loses all its energy in the epitaxial layer as it needs approximately 25  $\mu\text{m}$  silicon thicknesses to be fully stopped (cf. figure-62). So, assumed LET for  $\alpha$  particle is 5 MeV. The mean cluster size for 5 MeV  $\alpha$  is roughly 12.

The low energy beta particles (546 KeV) produce fat cluster with mean size  $\approx 9$ . A 546 KeV electron can travel  $\approx 500 \mu\text{m}$  in silicon [102] and in 25  $\mu\text{m}$  epitaxial layer, deposited energy will be,

$$546 \text{ KeV electron stopping power in silicon} = 1.625 \text{ MeVcm}^2/\text{g} \text{ (Taken from PSTAR)}$$

$$\text{Density of Silicon} = 2.329 \text{ g/cm}^3$$

$$\text{Deposited energy in } 25 \mu\text{m epitaxial layer} = 1.625 \text{ MeVcm}^2/\text{g} \times 2.329 \text{ g/cm}^3 \times 0.0025$$

$$\approx 0.00946 \text{ MeV}$$

$$\approx 9.46 \text{ KeV}$$

The high energy beta or MIPS (2.27 MeV) particles mostly go through the sensor and thus produce smaller cluster with mean value  $\approx 3$ . The energy deposited by the MIPS particle can be calculated from the e-h pair. To create a single e-h pair, 3.62 eV is needed and roughly 72 e-h pairs are produced by a MIP particle in 1  $\mu\text{m}$  silicon. So, in 25  $\mu\text{m}$  silicon, the energy loss will be [103],

$$dE/dx \times 25 \mu\text{m} = 72 \times 3.62 \text{ eV} \times 25 \mu\text{m} = 6516 \text{ eV} = 6.5 \text{ KeV}$$

The deposited energy in the epitaxial layer by six different X-ray sources depends on the energy of the photoelectron they produce. The photoelectron with energy from 6 KeV to 36

KeV, ranges few micrometer and mostly absorbed in the epitaxial layer of the sensor therefore the energy deposition represent the energy of the photoelectron. But when the energy goes 50 KeV, X-ray can penetrate more and probability of making photoelectron at far deep of epitaxial layer increases. The range of photoelectron is also  $\approx 20\text{-}25\ \mu\text{m}$  in silicon [104], so it can be scattered out of the sensor area with some energy and make less deposition of energy in the epitaxial layer. In this study, we have also seen that the cluster size for 50 KeV X-ray drops (cf. figure-64f) as an indication of less energy deposition.

The cluster size from the proton at  $V_{BB}=0\text{V}$  is higher and the mean is approximately 18 (cf. figure-68). The energy deposition by proton is done theoretically and value is taken from PSTAR [51]. 16 MeV proton beam losses  $\approx 5\ \text{MeV}$  while passing through 1.6 m of air. The 11 MeV proton losses 187 KeV in  $25\ \mu\text{m}$  epitaxial layer. The calculation is following,

### Step 1

$$16\ \text{MeV Proton stopping power in Air} = 24.47\ \text{MeVcm}^2/\text{g}$$

$$\text{Density of Air} = 1.225 \times 10^{-3}\ \text{g/cm}^3$$

$$\begin{aligned} \text{Deposited energy in 1.6 m Air} &= 24.47\ \text{MeVcm}^2/\text{g} \times 1.225 \times 10^{-3}\ \text{g/cm}^3 \times 160\ \text{cm} \\ &\approx 5\ \text{MeV} \end{aligned}$$

### Step 2

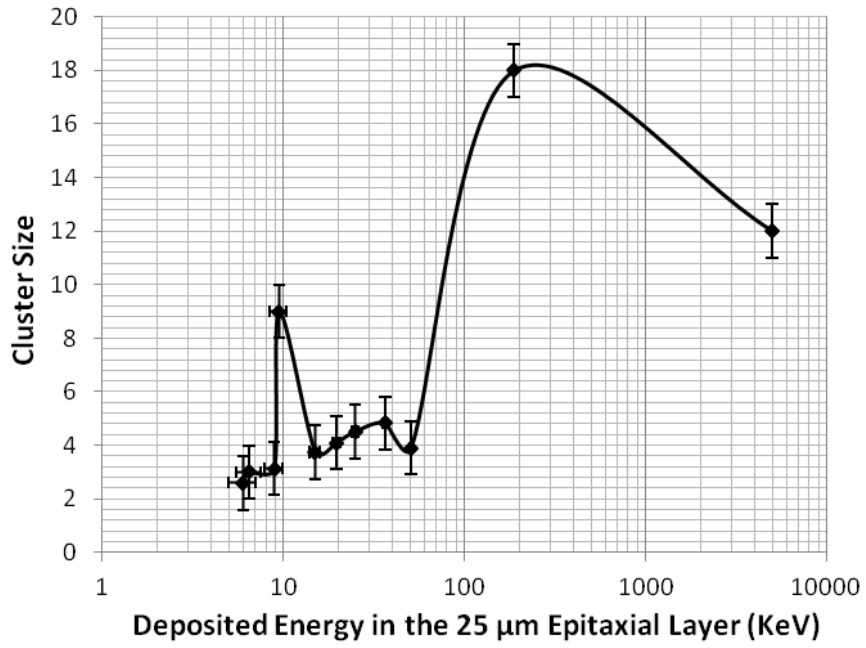
$$11\ \text{MeV Proton stopping power in Silicon} = 32.15\ \text{MeVcm}^2/\text{g}$$

$$\text{Density of Silicon} = 2.329\ \text{g/cm}^3$$

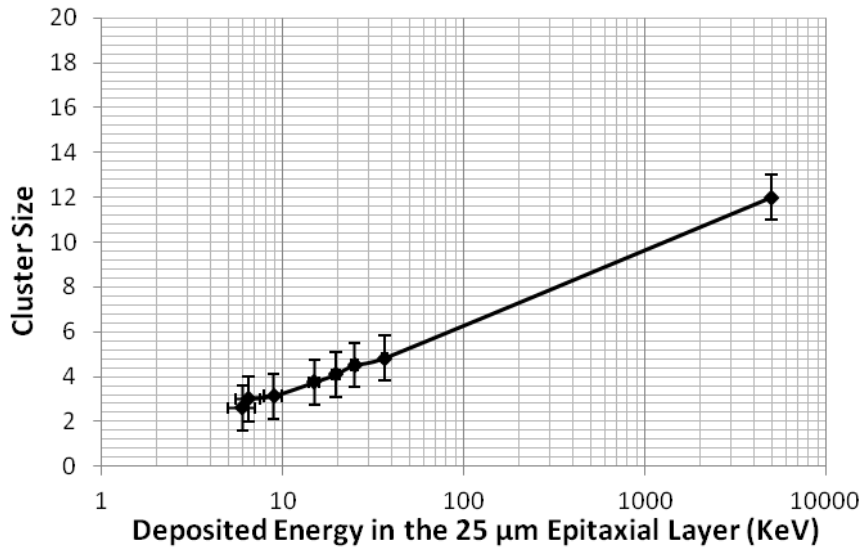
$$\begin{aligned} \text{Deposited energy in } 25\ \mu\text{m Silicon} &= 32.15\ \text{MeVcm}^2/\text{g} \times 2.329\ \text{g/cm}^3 \times 0.0025\ \text{cm} \\ &\approx 0.187\ \text{MeV} \\ &\approx 187\ \text{KeV} \end{aligned}$$

In the figure-69(a), the first bump at 9.46 KeV is from low energetic electron as low energetic electron makes bigger cluster. The second bump at 50 KeV is due to uncertainty in energy deposition by a 50 KeV photoelectron. A photoelectron with this energy does not deposit all its energy in the epitaxial layer so the deposited energy might be less than 50 KeV. The last bump is at 187 KeV and that is for proton. We had high energetic proton beam and the detector was placed before the bragg peak so small amount of energy was deposited in epitaxial layer but with bigger cluster size ( $\approx 18$ ). Also, the measured LET for proton is not very accurate rather an approximation because the stopping power of proton was considered constant. In real case, LET might increase as the proton beam is travelling and losing energy. Accurate LET could be obtained from simulation but due to time constrain simulation was skipped.

In figure-69(b) all the uncertainty with LET and cluster sizes are avoided and only known and accurate values are plotted. From this plot a linear relationship between cluster size and deposited energy is observed.



(a) With LET and cluster size uncertainty.



(b) Without uncertainty.

**Figure 69: Cluster Size vs. Deposited Energy/LET.**

## CHAPTER-6 CONCLUSIONS

The ongoing pCT project aims to build a clinical pCT prototype by 2022 in Bergen, Norway. MAPS-ALPIDE is the proposed sensor for this project. The TowerJazz 180 nm CMOS process will be used for ALPIDE pixel chip fabrication on wafers with a high resistive epitaxial layer on top of the substrate that amounting the total thickness of the chip to only 50  $\mu\text{m}$ . The partially depleted epitaxial layer acts as the sensitive layer. The size of the ALPIDE chip is  $15 \times 30 \text{ mm}^2$  with  $1024 \times 512$  array of  $30 \times 30 \mu\text{m}^2$ .

It is mentioned before that the ALPIDE chip was developed for ALICE experiments to know the physics of strongly interacting matter by improving particle measurement precision and increasing event readout rate. In pCT, high energetic proton beam traverses the target with intensity  $\sim 10^9$  protons/sec that requires a detector with high position resolution (tens of  $\mu\text{m}$ ), simultaneous tracking of large particle multiplicities, fast readout and radiation hardness. It also requires a detector with low mass and thin sensors (50  $\mu\text{m}$ ). These requirements put forward the necessity of designing a high granularity DTC with next-generation pixel sensor-ALPIDE.

### 6.1 Discussion on Performed Test and Findings

Several studies have been done in optimizing the ALPIDE chip over last few years. Chip characterization has been performed previously with earlier prototypes and this thesis was an effort to partially characterize the final ALPIDE chip and compare the performance between three chips as well as with earlier prototype.

The threshold and noise have an important effect on most of the performance parameters of the sensor. So the shift of the threshold and noise value with varying different parameters such as  $V_{\text{BB}}$ , ITHR, and VCASN was determined and measured for three available chips. Results and discussion are given in section-5.3.2 and 5.3.3.

The fake hit rate strongly affects the tracking performance and output data rate of a tracking device, therefore, it is important to know how to optimize the value of fake hit rate by adjusting all related parameter. Therefore the fake hit rate was measured with varying  $V_{\text{BB}}$ , ITHR, and VCASN for three chips. Results and discussion are given in section-5.3.4 and 5.3.5.

The nominal threshold and noise level were further used for detecting radiation effect in pixels. Few pixels in a particular chip, exposed by high energy alpha particle and having excessively high dose deposition, were investigated for radiation damage and a significant decrease in threshold and increase in noise value presented as an indication of radiation effect. Results and discussion are given in section-5.3.6

Before high energy proton beam test, it is important to know how the sensor responds to different low energy particles available at the laboratory. The sensor response is measured as cluster size and to investigate the cluster size the chip was exposed with X-ray (of different energy in KeV),  $\gamma$  (from a  $^{55}\text{Fe}$ -source),  $\beta$  (from a  $^{90}\text{Sr}$ -source) and  $\alpha$  (from a  $^{241}\text{Am}$ - source). It has been observed that for each of the particle the cluster size is distinguishable and

clusters size changes with changing energy. Cluster size analysis was done with C++ and root programming. The developed code is attached in the appendix.

With proton beam, the detector response at different flux was observed and cluster sizes were analyzed for two different reverse bias voltages along with justifying their change in size.

## **6.2 Implications of This Research**

This study is an initial effort to understand the chip performance and behavior also, to analyze test output for further interpretation of useful information.

Radiation damage is one of the top concerns for pCT. Detectors should be sufficiently radiation hard to stay in the beam line permanently to avoid costly and difficult installation and removal of the system very often. Detector's required performance is expected to sustain up to 5 years from the first installation time. Therefore the study of radiation damage and measure to mitigate the damaging effect is important.

This study will help to recognize damaged pixels and avoid exceeding maximum radiation limit to discourage the pCT image compromising for radiation damage. The investigation of radiation effect reveals the approximate dose level responsible for pixel threshold and noise shift. This study includes how the radiation effect can be observed and damaged pixels are separated. Also, the way of measuring the threshold and noise value only for damaged pixels is discussed. So for next such incident, this technique can be adopted.

The Cluster analysis for different particle helps to understand the particle types after detection because the sensor's response to different radiation is only recorded as pixel hits in other way cluster size. The sensor, designed for pCT is sensitive to all types of radiation but only proton information should be scrutinized for tracking the traversing path as well as energy loss in the object to be imaged.

This study also gives the proof of energy dependency of cluster size that indicates the possibility to assume the energy of the traversing particle from the cluster size.

## **6.3 Direction of Further Research**

This study gives a basic understanding about a very complicated ALPIDE chip which is under the consideration stage of being used as a sensor for clinical pCT prototypes. It was not possible to discuss everything about the chip in this short period of time and limited research frame. For pCT purpose, this study is only a primary effort in characterizing the ALPIDE chip as well as interpreting the sensor response to radiation.

The future research in this field can be directed in following recommended ways,

- For optimizing pixel's threshold and noise value, influences of bias parameters other than  $V_{BB}$ . ITHR and VCASN can be explored.

- In fake hit rate test, the result from chip-2 is not fully satisfying as its showing a comparative higher fake hit rate than other chip. But further experiment can be carried out with chip-2 to investigate if the fake hit rate decreases by masking the hot pixels.
- This study doesn't quantify the radiation effect level as well as the threshold of dose level for an ALPIDE chip. Further research can be conducted in that direction. Also, the normal temperature annealing capacity of the chip can be investigated by giving dose over a long period of time and measuring threshold and noise. Also, radiation hardness in terms of proton fluence can be studied.
- Cluster analysis with different energy and different particle can be done in future research to have better understanding of cluster size in parameter.

## APPENDIX

### A.1 Analog Front-End Optimization for Final ALPIDE

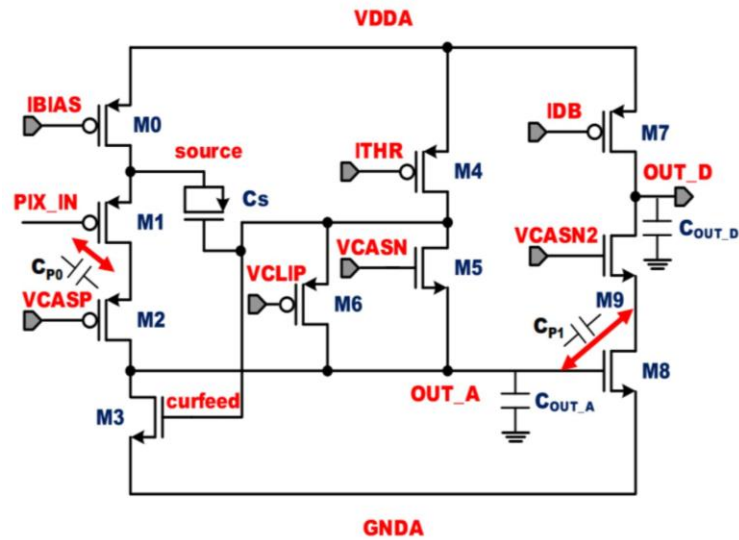
The chip matrix of ALPIDE-3 to final ALPIDE has 8 sectors of  $512 \times 128$  pixels [84]. On the chip, the sectors are numbered from left to right. Table-10 shows different front-end implementation for each sector.

Table 10: ALPIDE sectors [84].

Sector	M3, M5, M6, M8	VCASN2 (M9)	M1 bulk	Reset	Spacing
0	optimized size	Yes	AVDD	Diode	2 $\mu\text{m}$
1	optimized size	No	AVDD	Diode	2 $\mu\text{m}$
2	as in pALPIDE-1/2	No	AVDD	Diode	2 $\mu\text{m}$
3	optimized size	Yes	AVDD	Diode	2 $\mu\text{m}$
4	optimized size	Yes	Source	Diode	2 $\mu\text{m}$
5	optimized size	Yes	Source	Diode	3 $\mu\text{m}$
6	as in pALPIDE-1/2	No	AVDD	PMOS	2 $\mu\text{m}$
7	optimized size	Yes	AVDD	PMOS	2 $\mu\text{m}$

The final optimized ALPIDE analog front-end circuit schematic is shown in Figure-70. This prototype is designed to optimize the charge threshold spread by scaling transistor size with the constraint to fit the front-end in  $220 \mu\text{m}^2$  [83].

In the optimized front-end circuit, Sectors 2 and 6 execute the same architecture as in previous full-scale prototype and consist of larger current bias transistors (M0, M4, M7) but sector 2 uses diode reset scheme and sector 6 uses the PMOS reset scheme. Further reduction of the pixel-to-pixel mismatch was aimed by optimizing M3, M5, M6, M8 transistors size in Sector 1. Transistor M9 (VCASN2) is added in Sector 0.



**Figure 70: Optimized front end schematic with parasitic capacitance (cause gain reduction) of pALPIDE-3 [83].**

Sector 3 executes diode reset and sector 7 executed PMOS reset. This ALPIDE-3 configuration ensures an expected increase in the front-end gain by 18% [84]. The collection n-well has octagonal shape with 2  $\mu\text{m}$  diameter in all the sectors. All sectors have collection n-well to p-well spacing of 2  $\mu\text{m}$  except sector 5 and sector 5 shows the same circuitry like sector 4.

## A.2 List of Helium Beam Test on Chip-2

**Table 11: Details of chip-2 scan for Helium-4 ion beam**

<b>File Date &amp; Time</b>	<b>Bias Voltage (V)</b>	<b>Number of Steps</b>	<b>Step Size (um)</b>	<b>Dwell Time (ms)</b>	<b>Approximate Rate (kHz)</b>
180124_192025	0	128 x 128	1	100	2 +/- 1
180124_200918	-3	128 x 128	1	100	2 +/- 1
180124_205001	-3	128 x 128	1	100	10 +/- 2
180124_212250	0	128 x 128	1	100	10 +/- 2
180125_102831	0	128 x 128	1	200	10 +/- 2
180125_113158	-3	128 x 128	1	200	10 +/- 2
180125_132028	-6	128 x 128	1	100	10 +/- 2
180125_141939	0	L-shape, 1024 + 1024	1	200	10 +/- 2
180125_144208	-3	L-shape, 1024 + 1024	1	200	10 +/- 2

### A.3 C++ Code for ALPIDE Cluster Analysis

```
#include <cstdlib>
#include <iostream>
#include <fstream>
#include <string>

//#include <arrangement.o>
//#include "arrangement.cpp"
//string arrangement(string lineX)
using namespace std;
/*
 *
 */
int main(int argc, char** argv) {
cout << "Hello World\nProcessing Data...." << endl;
ifstream bigdata;
ofstream WriteFile;
ofstream WriteFileResultOnly;
ofstream finalWriteup;
//bigdata.open("E:\\PW\\last.dat");
bigdata.open("E:\\MY\\singEvt_180315_141551_Alpha.dat");
WriteFile.open("E:\\MY\\Result\\output7_2_Alpha.txt");
WriteFileResultOnly.open("E:\\MY\\Result\\output7singEvt_180315_141551_Alpha.txt");
finalWriteup.open("E:\\MY\\Result\\finalResult_singEvt_180315_141551_Alpha.txt");

if(bigdata.fail()){
cerr << "Error Opening file" << endl;
exit(1);}
string item;
string line;
string Cluster = "";
string grpClusterinaEvent = "";
string clusterSize = "";
string eventNclusterLine = "";
int i = 1, k=0, M =0;
int eventID = 0;
float totalEvent = 0;
float totalCluster = 0;
float avgCluster = 0;
int greaterthan10Cluster = 0;
int clusterCount = 0;
int clusterArray[1][5] ;
int total=0;
int A1 =0, B1 =0, C1=0, D1=0, E1=0;
int A_value = 0, B_value = 0, C_value =0;
//read the file until you have reached the end
while(!bigdata.eof()){
```

```

string V = "",W = "",X = "",Y = "",Z = "";
int A =0, B =0, C=0, D=0, E=0;
int SpaceAfterNumCount = 0;
int SpaceDetect =0;
int NumberDetect = 0;
int numStatus = 0;

//bigdata >> item;
getline (bigdata,line);
//cout << i <<endl;

// splitting the string line to five segment
for(int j=0;j<line.length();j++){
if((line[j]) == ' '){ SpaceDetect = 1; NumberDetect =0; }
if((line[j]) != ' '){ NumberDetect = 1; SpaceDetect =0;}

if(NumberDetect == 1){
numStatus = 1;
if(SpaceAfterNumCount == 0){
V += line[j];}
if(SpaceAfterNumCount == 1){
W += line[j];
}
if(SpaceAfterNumCount == 2){
X += line[j];
}
if(SpaceAfterNumCount == 3){
Y += line[j];
}
if(SpaceAfterNumCount == 4){
Z += line[j];
}
}
if(SpaceDetect == 1) {
if(numStatus ==1){
SpaceAfterNumCount += 1;
numStatus = 0;
}
}
}

// cout << " --->> " + V + " | "+ W + " | "+ X + " | "+ Y + " | "+ Z<< endl;
//WriteFile << "\n --->> " + V + " | "+ W + " | "+ X + " | "+ Y + " | "+ Z;

//String to integer conversion
A = atoi(V.c_str());
B = atoi(W.c_str());
C = atoi(X.c_str());
D = atoi(Y.c_str());
E = atoi(Z.c_str());

```

```

A_value = abs(A-A1);
B_value = abs(B-B1);
C_value = abs(C-C1);

//
//if((abs(A-A1) <=4) && (abs(B-B1) <=4) ) {
if(C_value == 0) {
//WriteFile << " <<<<";
k++;
if(( A_value <= 4) && (abs(B-B1) <=4)){
clusterCount++;
WriteFile <<" | \t ->" + to_string(clusterCount);
}else {
if(clusterCount >=1){
//    greaterthan10Cluster++;
M++;
WriteFile <<" | \t ---->> " + to_string(clusterCount+1);
Cluster += to_string(clusterCount+1);
Cluster += "|";

clusterSize += to_string(clusterCount+1)+",";
total = total + clusterCount+1;
}
clusterCount = 0;
}
}
//if(!((abs(A-A1) <=4) && (abs(B-B1) <=4))){
//if(!((abs(A-A1) <=4) && (abs(B-B1) <=4) && ((C-C1)==0))){
else{
totalEvent++;
eventID = C1;
if(clusterCount >=1){
//    greaterthan10Cluster++;
M++;
WriteFile << " | \t ---->> " + to_string(clusterCount+1);
Cluster += to_string(clusterCount+1);
Cluster += "|";

clusterSize += to_string(clusterCount+1);

total = total + clusterCount+1;
}
if(clusterCount ==0){
//    greaterthan10Cluster++;
//M++;
WriteFile << " | \t ---->> 0 ";
}
WriteFile << " >>>--- No. of Cluster in a event =>> " + to_string(M);

```

```

grpClusterinaEvent += to_string(M) + "|";
eventNclusterLine += "\n"+to_string(eventID)+"\t\t"+to_string(M)+"\t\t"+ clusterSize;

totalCluster = totalCluster + M;
clusterCount = 0;
M=0;
clusterSize = "";
}
//M=0;
WriteFile << "\n --->> " + V + " | " + W + " | " + X + " | " + Y + " | " + Z;
A1 = A; B1 = B; C1 = C; D1 = D; E1 = E;
i++;
}
cout << to_string(k) + "->" + to_string(clusterCount) + "->" + Cluster << endl;
WriteFile << "\n" + to_string(k) + "->" + to_string(clusterCount) + "-> \nTotal number of
Greater-than-10 Cluster =" + to_string(greaterthan10Cluster);
WriteFile << "\nTotal Value:" + to_string(total) + "\n->" + "Avg:" + to_string(((total)/1)) + "\n" +
Cluster << endl;

//arrangement("|1|2|3|4|");

//individual Cluster Size
string clusterline;
clusterline = Cluster;
int BarDetected = 0;
int NumberDetected = 0;
int lastGreaterNumb = 0;
int collectedNumb = 0;
string numbTemp = "";
string Arrangement = "";
WriteFile << to_string(clusterline.length())<<endl;
for(int j=0;j<clusterline.length();j++){
if(clusterline[j] == '|'){ BarDetected =1; NumberDetected = 0;}
if(clusterline[j] != '|'){ BarDetected =0; NumberDetected = 1;}

if(NumberDetected == 1){
numbTemp += clusterline[j];
}
if(BarDetected == 1){
collectedNumb = atoi(numbTemp.c_str());
//cout <<to_string(lastGreaterNumb) + "-->";
//      cout <<collectedNumb<<endl;
if(collectedNumb >lastGreaterNumb){
lastGreaterNumb = collectedNumb;
//      cout <<"->" + to_string(lastGreaterNumb);
}
numbTemp = "";
//collectedNumb = 0;
}
}
}

```

```

for( int k=0; k<=lastGreaterNumb; k++){
BarDetected = 0;
NumberDetected = 0;
collectedNumb = 0;
numbTemp = "";
int L=0;
for(int j=0;j<clusterline.length();j++){
if(clusterline[j] == '|'){ BarDetected =1; NumberDetected = 0;}
if(clusterline[j] != '|'){ BarDetected =0; NumberDetected = 1;}

if(NumberDetected == 1){
numbTemp += clusterline[j];
}
if(BarDetected == 1){
collectedNumb = atoi(numbTemp.c_str());
//cout <<to_string(lastGreaterNumb) + "-->";
//cout <<collectedNumb<<endl;
if(collectedNumb == k){
L++;
}
numbTemp ="";
//collectedNumb = 0;
}
}
Arrangement += to_string(k)+"-->" +to_string(L)+"|\n";
}
cout <<"Greater Numb: " + to_string(lastGreaterNumb)<<endl;
cout << Arrangement;
//individual cluster size finding end

WriteFile << "\n";
WriteFile << "\n";
WriteFile << "\n";
WriteFile << "Number of Event: " + to_string(totalEvent)<<endl;
WriteFile <<grpClusterinaEvent;
WriteFile << "\nGreater Numb: " + to_string(lastGreaterNumb)<<endl;

WriteFile <<eventNclusterLine;
finalWriteup <<"EventID No-of-Cluster \t Cluster-Size";
finalWriteup <<eventNclusterLine;
avgCluster = totalCluster/totalEvent;
finalWriteup << "\nAvrg no of cluster per event:" +to_string(totalCluster)+ "/" +
to_string(totalEvent)+ "=" +to_string(avgCluster);

finalWriteup << "\n\nMost Frequent Cluster size\n" +Arrangement;

WriteFile << "\n";
WriteFile <<Arrangement;
WriteFileResultOnly <<Arrangement;

```

```
WriteFile.close();  
bigdata.close();  
finalWriteup.close();
```

```
return 0;  
}
```

## BIBLIOGRAPHY

- [1] R. W. Schulte and S. N. Penfold, “Proton CT for Improved Stopping Power Determination in Proton Therapy, invited,” *Trans. Am. Nucl. Soc.*, vol. 106, pp. 55–58, 2012.
- [2] M. Jermann, “Particle Therapy Statistics in 2014,” *Int. J. Part. Ther.*, vol. 2, no. 1, pp. 50–54, 2015.
- [3] H. E. S. Pettersen *et al.*, “Proton tracking in a high-granularity Digital Tracking Calorimeter for proton CT purposes,” *Nucl. Instruments Methods Phys. Res. Sect. A Accel. Spectrometers, Detect. Assoc. Equip.*, vol. 860, no. January, pp. 51–61, 2017.
- [4] “PTCOG,” “Particle Therapy Cooperative Group,” *March 2018*. [Online]. Available: [ptcog.ch/index.php/clinical-protocols](http://ptcog.ch/index.php/clinical-protocols). [Accessed: 18-Mar-2018].
- [5] “Medical Imaging.” [Online]. Available: <http://www.who.int>. [Accessed: 19-Mar-2018].
- [6] W. R. Hendee, E. R. Ritenour, and K. R. Hoffmann, *Medical Imaging Physics*, Fourth., vol. 30, no. 4. 2003.
- [7] W. G. Bradley, “History of Medical Imaging,” *Proc. Am. Philos. Soc.*, vol. 152, no. 3, pp. 349–361, 2008.
- [8] R. A. Sofferman, *Ultrasound of the Thyroid and Parathyroid Glands*. Springer Science & Business Media, 2011.
- [9] J. T. Bushberg *et al.*, *The Essential Physics of Medical Imaging*, Third. 2012.
- [10] J. Hsieh, *Computed Tomography: Principles, Design, Artifacts, and Recent Advances*, Second. Bellingham, WA: SPIE, 2009.
- [11] W. R. Hendee, “Physics and Applications of Medical Imaging,” *Rev. Mod. Phys.*, vol. 71, no. 2, p. S444, 1999.
- [12] L. E. Romans, “Computed Tomography for Technologists: A comprehensive Text,” 2011. pp. 30–31, 2011.
- [13] P. Shreve and D. W. Townsend, *Clinical PET-CT in Radiology: Integrated Imaging in Oncology*. Springer Science & Business Media, 2010.
- [14] F. A. Mettler *et al.*, “Radiologic and Nuclear Medicine Studies in the United States and Worldwide: Frequency, Radiation Dose, and Comparison with Other Radiation Sources—1950–2007,” *Radiology*, vol. 253, no. 2, pp. 520–531, 2009.
- [15] E. J. Hall and D. J. Brenner, “Cancer Risks from Diagnostic Radiology,” *Br. J. Radiol.*, vol. 81, no. 965, pp. 362–378, 2008.
- [16] E. B. Podgorsak, *Radiation Oncology Physics: A Handbook for Teachers and Students*. Vienna: International Atomic Energy Agency, 2005.
- [17] D. N. M. Ershaidat, “Charged Particle Interactions.” .
- [18] R. W. Schulte *et al.*, “Density resolution of proton computed tomography,” *Med. Phys.*, vol. 32, no. 4, pp. 1035–1046, 2005.
- [19] A. Getachew, “Stopping Power and Range of Protons of Various Energies in Different Materials,” Addis Ababa University, 2007.
- [20] C. Candela Juan, M. Crispin-Ortuzar, and M. Aslaninejad, “Depth-Dose Distribution

- of Proton Beams Using Inelastic-Collision Cross Sections of Liquid Water,” *Nucl. Instruments Methods Phys. Res. Sect. B Beam Interact. with Mater. Atoms*, vol. 269, no. 2, pp. 189–196, 2011.
- [21] F. Bloch, “Zur bremsung rasch bewegter teilchen beim durchgang durch materie,” *Ann. Phys.*, vol. 408, no. 3, pp. 285–320, 1933.
- [22] H. Bethe, “Zur theorie des durchgangs schneller korpuskularstrahlen durch materie,” *Ann. Phys.*, vol. 397, no. 3, pp. 325–400, 1930.
- [23] U. Schneider and E. Pedroni, “Multiple Coulomb scattering and spatial resolution in proton radiography,” *Med. Phys.*, vol. 21, no. 11, pp. 1657–1663, 1994.
- [24] D. C. Williams, “The most likely path of an energetic charged particle through a uniform medium,” *Phys. Med. Biol.*, vol. 49, no. 13, pp. 2899–2911, 2004.
- [25] H. A. Bethe, “Molière’s theory of multiple scattering,” *Physical Review*, vol. 89, no. 6, pp. 1256–1266, 1953.
- [26] U. Weber and G. Kraft, “Comparison of Carbon Ions Versus Protons,” *Cancer J.*, vol. 15, no. 4, pp. 325–332, 2009.
- [27] E. B. Podgorsak, *Radiation Physics for Medical Physicists*, Second. Springer Science & Business Media, 2010.
- [28] M. T. Studenski and Y. Xiao, “Proton Therapy Dosimetry Using Positron Emission Tomography,” *World J. Radiol.*, vol. 2, no. 4, p. 135, 2010.
- [29] Faiz M. Khan and J. P. Gibbons, *Khan’s The Physics of Radiation Therapy*, Fifth. 2014.
- [30] R. R. Wilson, “Radiological Use of Fast Protons,” *Radiology*, vol. 47, no. 5, pp. 487–491, 1946.
- [31] S. Pieplensbosch, “Potential benefits of proton therapy in clinic,” 2015.
- [32] D. Schulz-Ertner, O. Jäkel, and W. Schlegel, “Radiation Therapy With Charged Particles,” *Semin. Radiat. Oncol.*, vol. 16, no. 4, pp. 249–259, 2006.
- [33] T. Ohno, “Particle radiotherapy with carbon ion beams,” *EPMA J.*, vol. 4, no. 1, p. 9, 2013.
- [34] A. M. Cormack, “Early two-dimensional reconstruction and recent topics stemming from it,” *Med. Phys.*, vol. 7, no. 4, pp. 277–282, 1980.
- [35] C. BOPP, “The proton as a dosimetric and diagnostic probe,” Universite De Strasbourg, 2014.
- [36] M. Goitein, “Three-dimensional density reconstruction from a series of two-dimensional projections,” *Nucl. Instruments Methods*, vol. 101, no. 3, pp. 509–518, 1972.
- [37] K. M. Crowe, T. F. Budinger, J. L. Cahoon, V. P. Elischer, R. H. Huesman, and L. L. Kanstein, “Axial scanning with 900 MeV alpha particles,” *IEEE Trans. Nucl. Sci.*, vol. 22, no. 3, pp. 1752–1754, 1975.
- [38] G. Poludniowski, N. M. Allinson, and P. M. Evans, “Proton radiography and tomography with application to proton therapy,” *Br. J. Radiol.*, vol. 88, no. 1053, pp. 1–14, 2015.

- [39] K. M. Hanson *et al.*, “Computed tomography using proton energy loss,” *Phys. Med. Biol.*, vol. 26, no. 6, pp. 965–983, 1981.
- [40] K. Hanson, “Proton Computed Tomography,” *IEEE Trans. Nucl. Sci.*, vol. 26, no. 1, pp. 1635–1640, 1979.
- [41] K. M. Hanson *et al.*, “The Application of Protons to Computed Tomography,” *J. Comput. Assist. Tomogr.*, vol. 2, no. 5, pp. 671–674, 1978.
- [42] K. M. Hanson *et al.*, “Proton computed tomography of human specimens,” *Phys. Med. Biol.*, vol. 27, no. 1, pp. 25–36, 1982.
- [43] D. West and A. C. Sherwood, “Proton-scattering radiography,” *Non-Destructive Test.*, vol. 6, no. 5, pp. 249–257, 1973.
- [44] A. M. Koehler, “Proton radiography,” *Science (80- )*, vol. 160, no. 3825, pp. 303–304, 1968.
- [45] V. W. Steward, “Proton (Heavy Ion) Radiography in Medical Diagnosis,” *IEEE Trans. Nucl. Sci.*, vol. 26, no. 2, pp. 2257–2261, 1979.
- [46] J. Saudinos, G. Charpak, F. Sauli, D. Townsend, and J. Vinciarelli, “Nuclear scattering applied to radiography,” *Phys. Med. Biol.*, vol. 20, no. 6, p. 890, 1975.
- [47] D. West and A. C. Sherwood, “Radiography with 160 MeV Protons,” *Nature*, vol. 239, p. 157, Sep. 1972.
- [48] R. Schulte *et al.*, “Design of a proton computed tomography system for applications in proton radiation therapy,” *Nucl. Sci. Symp. Conf. Rec. 2003 IEEE*, vol. 3, pp. 1579–1583, 2003.
- [49] R. F. Hurley, R. W. Schulte, V. Bashkirov, G. Coutrakon, H. F.-W. Sadrozinski, and B. Patyal, “The Phase I Proton CT Scanner and Test Beam Results at LLUMC,” *Trans Am Nucl Soc.*, no. 106, pp. 63–66, 2012.
- [50] R. Schulte *et al.*, “Conceptual design of a Proton Computed Tomography System for Applications in Proton Radiation Therapy,” *IEEE Trans. Nucl. Sci.*, vol. 51, no. 3, p. 866, 2004.
- [51] “PSTAR database, National Institute for Standards and Technology.” [Online]. Available: <https://physics.nist.gov/PhysRefData/Star/Text/PSTAR.html>. [Accessed: 25-Mar-2018].
- [52] M. H. Phillips, K. J. Stelzer, T. W. Griffin, M. R. Mayberg, and H. R. Winn, “Stereotactic radiosurgery: a review and comparison of methods,” *J. Clin. Oncol.*, vol. 12, no. 5, pp. 1085–1099, 1994.
- [53] P. Pemler *et al.*, “A detector system for proton radiography on the gantry of the Paul-Scherrer-Institute,” *Nucl. Instruments Methods Phys. Res. Sect. A Accel. Spectrometers, Detect. Assoc. Equip.*, vol. 432, no. 2–3, pp. 483–495, 1999.
- [54] T. Li *et al.*, “Reconstruction for proton computed tomography: a Monte Carlo study,” *Nucl. Sci. Symp. Conf. Rec. 2003 IEEE*, vol. 4, pp. 2767–2770, 2003.
- [55] T. Li, Z. Liang, J. V. Singanallur, T. J. Satogata, D. C. Williams, and R. W. Schulte, “Reconstruction for proton computed tomography by tracing proton trajectories: A Monte Carlo study,” *Med. Phys.*, vol. 33, no. 3, pp. 699–706, 2006.
- [56] Y. Saraya, T. Izumikawa, J. Goto, T. Kawasaki, and T. Kimura, “Study of spatial

- resolution of proton computed tomography using a silicon strip detector,” *Nucl. Instruments Methods Phys. Res. Sect. A Accel. Spectrometers, Detect. Assoc. Equip.*, vol. 735, pp. 485–489, 2014.
- [57] E. Song, H. Ryu, J. Lee, and J. Kim, “Image resolution of proton radiography by using a range modulation technique,” *J. Korean Phys. Soc.*, vol. 52, p. 904, 2008.
- [58] U. Amaldi *et al.*, “Construction, test and operation of a proton range radiography system,” *Nucl. Instruments Methods Phys. Res. Sect. A Accel. Spectrometers, Detect. Assoc. Equip.*, vol. 629, no. 1, pp. 337–344, 2011.
- [59] V. V Denyak *et al.*, “Dose energy dependence in proton imaging,” *Nucl. Instruments Methods Phys. Res. Sect. A Accel. Spectrometers, Detect. Assoc. Equip.*, vol. 652, no. 1, pp. 747–750, 2011.
- [60] T. Satogata, H. F.-W. Sadrozinski, A. Ruggiero, and A. Dilmanian, “Dose / Sensitivity in Proton Computed Tomography,” *2003 IEEE Nucl. Sci. Symp. Med. Imaging Conf.*, vol. 5, pp. 3667–3671, 2003.
- [61] E. Rocco, “Highly granular digital electromagnetic Calorimeter with MAPS,” *Nucl. Part. Phys. Proc.*, vol. 273–275, pp. 1090–1095, 2016.
- [62] K. Austreim, “Proton Beam Test Of A High Granularity Calorimeter For Proton Computed Tomography,” University of Bergen, 2015.
- [63] E. R. Fossum, “CMOS image sensors: electronic camera on a chip,” *Proc. Int. Electron Devices Meet.*, no. 3, pp. 17–25, 1995.
- [64] R. Turchetta *et al.*, “A monolithic active pixel sensor for charged particle tracking and imaging using standard VLSI CMOS technology,” *Nucl. instruments methods Phys. Res. A*, vol. 458, pp. 677–689, 2001.
- [65] R. Turchetta, “CMOS Monolithic Active Pixel Sensors ( MAPS ) for scientific applications,” 2003.
- [66] S. Kleinfelder, S. Lim, X. Liu, and A. El Gamal, “CMOS Digital Pixel Sensor with Pixel-Level Memory,” *Solid-State Circuits Conf. 2001. Dig. Tech. Pap. ISSCC. 2001 IEEE Int.*, pp. 88–89, 435, 2001.
- [67] D. X. D. Yang, A. El Gamal, B. Fowler, and H. Tian, “640×512 CMOS image sensor with ultrawide dynamic range floating-point pixel-level ADC,” *IEEE J. Solid-State Circuits*, vol. 34, no. 12, pp. 1821–1834, 1999.
- [68] D. X. D. Yang, B. Fowler, and A. El Gamal, “A Nyquist-Rate Pixel-Level ADC for CMOS Image Sensors,” *IEEE J. Solid-State Circuits*, vol. 34, no. 3, pp. 348–355, 1999.
- [69] R. Turchetta *et al.*, “CMOS Active Pixel Sensors: Design For Scientific Applications,” *RUTHERFORD Applet. LABS Chilt. (UNITED KINGDOM)*, 2005.
- [70] Miljenko and Suljic, “Characterisation of Monolithic Active Pixel Sensors for the upgrade of the ALICE Inner Tracking System detector,” Universit` a degli Studi di Trieste, 2013.
- [71] Miljenko Suljic, “Study of Monolithic Active Pixel Sensors for the Upgrade of the ALICE Inner Tracking System,” Universit` a Degli Studi di Trieste, 2017.
- [72] S. Meroli, D. Passeri, and L. Servoli, “Energy loss measurement for charged particles in very thin silicon layers,” *J. Instrum.*, vol. 6, no. 6, 2011.

- [73] I. Aimo, “Studies on Monolithic Active Pixel Sensors for the Inner Tracking System Upgrade of ALICE Experiment,” Politecnico di Torino, 2015.
- [74] L. Landau, “On the energy loss of fast particles by ionization,” *J. Phys.(USSR)*, vol. 8, pp. 201–205, 1944.
- [75] P. V Vavilov, “Ionization losses of high-energy heavy particles,” *Zh. Eksp. Teor. Fiz.*, vol. 32, pp. 749–751, 1957.
- [76] J. Willem van Hoorne, “Study and Development of a novel Silicon Pixel Detector for the Upgrade of the ALICE Inner Tracking System,” Technische Universitat Wien, 2015.
- [77] G. R. Lynch and O. I. Dahl, “Approximations to Multiple Coulomb Scattering,” *Nucl. Inst. Methods Phys. Res. B*, vol. 58, no. 1, pp. 6–10, 1991.
- [78] L. Rossi, P. Fischer, T. Rohe, and N. Wermes, *Pixel Detectors: From Fundamentals to Applications*. 2005.
- [79] A. Collu, “Development and characterisation of Monolithic Active Pixel Sensor prototypes for the upgrade of the ALICE Inner Tracking System,” Università degli Studi di Cagliari, 2015.
- [80] F. Reidt, “Studies for the ALICE Inner Tracking System Upgrade,” University of Heidelberg, 2016.
- [81] T. Lazareva, “Analysis of test beam data of ALPIDE, the Monolithic Active Pixel Sensor (MAPS) for the ALICE ITS upgrade,” 2017.
- [82] I. Ravasenga, “Development of Monolithic Pixel Sensors for ALICE Experiment,” Università di Torino, 2015.
- [83] D. Kim *et al.*, “Front end optimization for the monolithic active pixel sensor of the ALICE Inner Tracking System upgrade,” *J. Instrum.*, vol. 11, no. 2, 2016.
- [84] A. I. A. development Team, “ALPIDE-3 Operations Manual - DRAFT.” 2016.
- [85] P. Yang *et al.*, “Low-power priority Address-Encoder and Reset-Decoder data-driven readout for Monolithic Active Pixel Sensors for tracker system,” *Nucl. Instruments Methods Phys. Res. Sect. A Accel. Spectrometers, Detect. Assoc. Equip.*, vol. 785, no. 2015, pp. 61–69, 2015.
- [86] D. Christian, “Quantifying Flux for (Bulk) Radiation Damage Studies,” pp. 8–9, 2001.
- [87] E. Borchini and M. Bruzzi, *Radiation damage in silicon detectors*, vol. 17, no. 11. La Rivista del Nuovo Cimento (1978-1999), 1994.
- [88] E. Fretwurst *et al.*, “Radiation Damage in Silicon Detectors Caused by Hadronic and Electromagnetic Irradiation,” *IEEE Trans. Nucl. Sci.*, no. December, p. 35, 2002.
- [89] M. Keil, “ALPIDE Software - User manual.” pp. 1–6, 2017.
- [90] G. Deptuch, “New Generation of Monolithic Active Pixel Sensors for Charged Particle Detection,” Université Louis Pasteur - Strasbourg I, 2002, 2005.
- [91] H. Tian, B. Fowler, and A. El Gamal, “Analysis of temporal noise in CMOS photodiode active pixel sensor,” *IEEE J. Solid-State Circuits*, vol. 36, no. 1, pp. 92–101, 2001.
- [92] G. T. Seaborg, *Modern alchemy: selected papers of Glenn T. Seaborg*, vol. 20. World

- Scientific, 1994.
- [93] U. R. Integrity, “Americium-241.”
  - [94] R. J. Budnitz, “Strontium-90 and Strontium-89: A review of Measurement Techniques in Environmental Media,” pp. 1–14, 1974.
  - [95] M. M. Bé *et al.*, “Table of Radionuclides (vol. 3–A= 3 to 244),” *Monogr. BIPM*, vol. 5, 2006.
  - [96] B. L. Henke, E. M. Gullikson, and J. C. Davis, “X-Ray Interactions: Photoabsorption, Scattering, Transmission and Reflection  $E = 50\text{--}30,000$  eV,  $Z = 1\text{--}92$ ,” 2010.
  - [97] E. M. A. Hussein, “Hand Book on Radiation Probing and Imaging, vol. 1.” Springer, 2003.
  - [98] G. Genov, M. E. Rostad, and A. O. Solberg, “CZT and BGO spectroscopic performance testing. University of Bergen,” 2017.
  - [99] A. T. Samnøy, “ALPIDE IBIC Report,” University of Bergen.
  - [100] R. T. Pace and B. S. H. G. Dip, “Alpha Radiation Effects in Integrated Circuits : Investigating Options for Sensors,” University of South Australia, 1999.
  - [101] “X-Ray attenuation & absorption calculator.” [Online]. Available: [http://web-docs.gsi.de/~stoe\\_exp/web\\_programs/x\\_ray\\_absorption/index.php](http://web-docs.gsi.de/~stoe_exp/web_programs/x_ray_absorption/index.php). [Accessed: 10-May-2018].
  - [102] A. N. Larsen and A. Mesli, “Electron and Proton Irradiation of Silicon,” in *Semiconductors and Semimetals*, vol. 91, Elsevier, 2015, pp. 47–91.
  - [103] M. Krammer, “Silicon Detectors,” *Inst. High Energy Physics, Vienna, Austria*, 2011.
  - [104] Z. Wang, “On the Single-Photon-Counting (SPC) modes of imaging using an XFEL source,” *J. Instrum.*, vol. 10, no. 12, 2015.
  - [105] W. Poonsawat, C. Kobdaj, M. Sitta, and Y. Yan, “Material Budget Calculation of the new Inner Tracking,” vol. XX, no. X, pp. 1–8, 2017.